**The Thesis Committee for Georgios Moutsanidis**
**Certifies that this is the approved version of the following thesis:**

# Progressive Collapse Resistance of Steel-Framed Structures with Composite Floor Systems

**APPROVED BY**
**SUPERVISING COMMITTEE:**

**Supervisor:**

Eric Williamson

Michael Engelhardt

# Progressive Collapse Resistance of Steel-Framed Structures with Composite Floor Systems

**by**

**Georgios Moutsanidis, M.Eng.**

**Thesis**

Presented to the Faculty of the Graduate School of

The University of Texas at Austin

in Partial Fulfillment

of the Requirements

for the Degree of

**Master of Science in Engineering**

**The University of Texas at Austin**

**August 2014**

## Dedication

To my parents who have contributed the most to everything I have accomplished in my life

"When you set sail for Ithaka, wish for the road to be long…"

*Constantine P. Cavafy*

# Acknowledgements

This material is based upon work supported by the Science and Technology Directorate, U.S. Department of Homeland Security under Award Number: 2010-ST-108-000014. The views and conclusions contained in this document are those of the author and should not be interpreted as representing official policies, either expressed or implied, of the U.S. Department of Homeland Security.

Special thanks go to Dr. Eric Williamson for all his support over the past two years. Thank you for giving me the opportunity to work on this research project and for all your support and interest in my progress within and beyond this research. Your guidance has been invaluable to the progress of my academic life. I would also like to express my gratitude to Dr. Michael Engelhardt for his helpful guidance within the research project and for his interest and support in my academic progress.

I would also like to deeply thank my classmate and research partner, Michalis Hadjioannou. His personality, knowledge, and patience helped me to adjust myself in the lab and overcome difficulties I encountered during my research progress.

Finally, I would like to thank the rest of the research team: Lindsay Hull and Umit Can Oksuz. Thanks for all of your hard work, devotion, and friendliness during your work at this research project.

July 16, 2014

# Abstract

## Progressive Collapse Resistance of Steel-Framed Structures with Composite Floor Systems

Georgios Moutsanidis, MSE

The University of Texas at Austin, 2014

Supervisor: Eric B. Williamson

Progressive collapse research intends to evaluate and quantify the resistance of structural systems against local failures independent of how such failures may initiate. The present research program pertains to the simulation and analysis of a structural gravity frame with composite floor system under column loss scenarios. The ultimate goal of this research is to evaluate and possibly identify any potential deficiencies in the current progressive collapse guidelines.

This thesis presents the construction, testing, and results of a test performed on a steel-concrete composite structure with shear connections under a perimeter column removal. The structure was designed based on typical design guidelines. After the column removal, the specimen was subjected to increasing uniform load and was found to resist the full progressive collapse design load without major failures.

In addition, computational work pertaining to the composite floor system behavior and the interaction among the beams, the slab, and the shear connectors was conducted. The purpose of this work was to identify possible deficiencies in the current

simulation techniques for composite structure modeling under progressive collapse scenarios. After the analyses were conducted, it was found that the majority of current simulation techniques are adequate for modeling composite floor systems, with the use of nonlinear springs being the most accurate and computationally efficient.

# Table of Contents

# List of Tables

# List of Figures

# CHAPTER 1

# Introduction and Research Motivation

## 1.1 PROGRESSIVE COLLAPSE DEFINITION

Progressive collapse is a structural process in which failure of a structural element triggers the failure of adjoining structural elements and eventually the failure of a disproportionately large part of a structure relative to the initial cause. In the research literature, the terms *disproportionate* collapse and *progressive* collapse are used to describe this general process. While some researchers have offered slightly different definitions for these terms, they will be used interchangeably in this thesis.

Another term that is often used when describing progressive collapse issues is the robustness of a structure. Robustness is a structure's ability to resist damage without failure and it is an inherent structural property. It is not achieved by oversizing the structural elements but by designing the structural system in a way that, in the event an element fails, load redistribution takes place. Parameters that are related to robustness and have an influence on progressive collapse resistance are ductility, energy absorption, redundancy, and continuity.

Progressive collapse might be initiated by a variety of scenarios. One common scenario is a column loss. However, other element failures, such as crushing of slabs or fracture of connections, might also trigger progressive collapse. As far as the cause is concerned, a common assumption is that blast loads may initiate a progressive collapse, where the blast may be caused either by an accident or a terrorist attack. Other triggering mechanisms include earthquakes, impacts, foundations settlements, and human mistakes during construction. Therefore, code provisions and guidelines dealing with disproportionate collapse are threat independent, meaning that no matter what the cause

of an element's failure, the structure should be designed in a way to resist this particular loss (GSA 2003; U.S. DoD, 2009).

Finally, although progressive collapse usually takes place in a vertical manner due to gravity forces, often referred to as "pancaking", horizontal progressive collapse is also possible in which there is successive lateral failure of adjacent structural bays.

## 1.2 SIGNIFICANCE OF PROGRESSIVE COLLAPSE AND REMARKABLE EVENTS

The progressive collapse resistance of a structure is of great importance because it is connected not only to structural integrity but also to protection of human lives. Loss of structural integrity could have devastating consequences. To address these concerns, the U.S. Department of Defense (U.S. DoD, 2009) and the General Services Administration (GSA, 2003) have both developed guideline documents to provide engineers with information regarding how to mitigate the possibility of progressive collapse. The concern over progressive collapse is not limited to the U.S.; other countries have also developed design guidelines (e.g., CPNI, 2011). To demonstrate the significance and devastating effects of progressive collapse, a few notable incidents are described below.

### *1.2.1 Ronan Point Apartment Tower (UK, 1968)*

The first well known and one of the most infamous cases of progressive collapse caused by a non-terrorist explosion is the Ronan Point Apartment Tower event. This particular building was constructed in 1968 using the Larsen-Nielsen system, which was developed in Denmark (Pearson, 2003). In such a system, all elements were precast concrete load-bearing components. Therefore the gravity loads were transferred to the ground through the load bearing walls without the presence of additional columns. The wall and the floor panels were fit together using slots. These joints were then bolted

together and filled with dry pack mortar. This particular method of construction was simpler and faster than conventional construction techniques in use at that time. It was widely adopted in the UK after the Second World War due to the urgent need for building housing facilities and because of the lack of skilled construction workers (Pearson, 2003). The Ronan Point Apartment Tower was 22-stories tall, and there were 110 apartments in the building.

On the morning of May 16, 1968, an occupant of apartment 90 on the 18$^{th}$ floor lit a match for her stove, which initiated a gas explosion due to a leak. In total, four people died and seventeen were injured (Pearson, 2005). The explosion destroyed the load bearing walls in the opposite corner of the apartment. These walls served as supports to the upper floors. Therefore, after this loss, a chain reaction was triggered. Initially, floors nineteen through twenty-two collapsed one after another because they were left unsupported. The four collapsing floors fell onto floor eighteen, which could not resist the impacting kinetic energy, initiating a sequence of failures that propagated downward until it reached the ground floor. As a result, the entire southeast corner of the structure collapsed (see Fig.1-1).

Figure 1-1: Ronan Point Apartment Tower Partial Collapse after Gas Explosion (Pearson, 2005)

Following the collapse, the British government formed a panel to investigate the possible causes. The main factor that led to the explosion was a substandard brass nut that had been used to connect the hose to the stove (Griffiths, 1968). However, it was concluded that the explosion was small, and the resulting internal pressure load was estimated to be less than 10 psi. Later, the Building Research Station and Imperial College London conducted research to determine the structural resistance and deficiencies of the building (Levy, 1992). The results indicated that the bearing walls could be displaced by a pressure of only 2.8 psi. The investigation revealed serious design deficiencies. The building was designed for wind velocities of 63 mph based on code provisions dating back in 1952 that did not take into account high-rise buildings. Much stronger winds were known to occur quite frequently, however, and the codes

were out of date. In addition, it was found that fire could also lead to progressive collapse of Ronan Point, and it was also highlighted that the Larsen-Nielsen system was designed for low-rise buildings only. No alternative load path was provided, and the collapse was due to a lack of structural redundancy. The building was reconstructed and occupants moved in again.

Many years later, architect Sam Webb conducted a survey to assess the condition of the building (Pearson, 2003). His findings revealed many cracks in the central stairway and elevator shaft, and he concluded that in high winds the structure was beginning to fail.

The above mentioned findings led to the demolition of the entire building in May 1986. Instead of a traditional demolition, Ronan Point was dismantled floor by floor so possible construction deficiencies could be revealed. In fact, the investigators found really poor workmanship including unattached fixing straps, panels placed on bolts instead of mortar, and inadequate mortar in most floor-wall joints. These findings led to the demolition of all the Larsen-Nielsen structural systems in the UK.

The importance of the Ronan Point collapse can be seen in the strong impact this event had on building codes. The British conducted extensive research on progressive collapse, which was followed by research conducted in the US that eventually led to the development of new design criteria (Fuller, 1975). The Portland Cement Association and the Prestressed Concrete Institute issued their own guidelines (Ross, 1984), the need for structural robustness and redundancy was realized (Shepherd, 1995), and quality control was recognized to be a crucial aspect for successful construction (Feld, 1997).

### *1.2.2 Alfred P. Murrah Federal Building (OK, 1995)*

A representative case of progressive collapse that is widely cited by many researchers is the failure of the Murrah Building in Oklahoma City, OK. This building suffered disproportionate collapse in 1995 following a terrorist attack.

The construction of the Murrah Federal Building started in 1974, and it was completed within 20 months. The building consisted of a nine-story office building with one-story ancillary east and west wings along with an adjacent multilevel parking structure (FEMA 277, 1996). The structural system of the building consisted of ordinary moment frames supporting gravity loads and reinforced concrete shear walls resisting lateral loads. On the first and second floors of the building's north face, the columns were spaced at a center-to-center distance of 40 ft (Line G in Figure 1-2). These columns supported a transfer girder at the height of the third floor, as can be seen in Figures 1-3 and 1-4. Above the third floor, columns were spaced at a center-to-center distance of 20 feet. The building was designed in accordance with the provisions of ACI 318-71 (ACI, 1971) and complied with all applicable building code requirements.

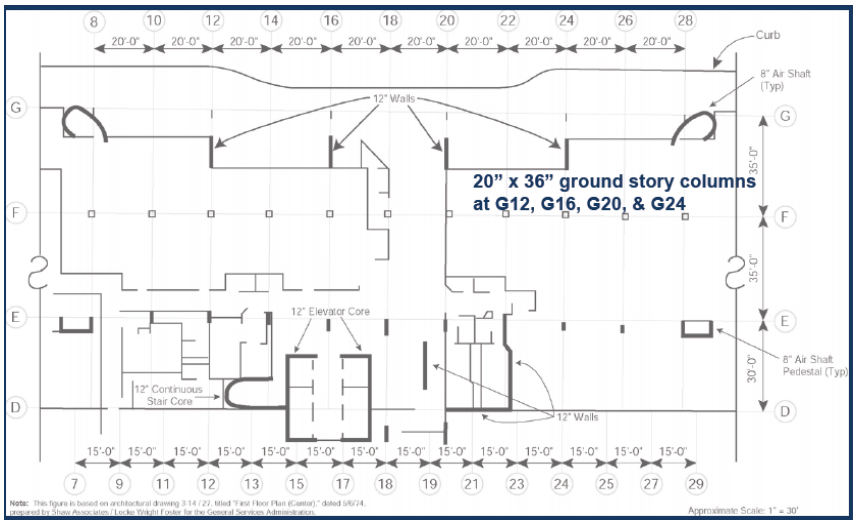


Figure 1-2: First Floor Plan (FEMA 277, 1996)

On April 19, 1995, terrorists attacked the Murrah Federal Building using a truck filled with a mixture of ammonium nitrate and fuel oil (ANFO). According to extensive research that followed the attack, the charge weight was estimated to be equivalent to approximately 4000 lb of TNT (FEMA 439A, 2005). The explosion took place approximately 14 ft away from the north face of the building. The explosion killed 168 people and injured 680. In addition, nearly 50000 people were forced to evacuate the Oklahoma City downtown area, 86 cars were burned, and 324 buildings were damaged as a result of the attack (Oklahoma City Police Department, 1995).

From the 324 structures that were damaged, the Alfred P. Murrah Federal Building was the most severely affected. Almost half of the building collapsed, and the remaining portion was demolished after investigations were completed. According to FEMA 439A (2005), only 4% of the structure collapsed due to the direct blast effect, while approximately 42% collapsed because of the progressive collapse that followed the first element loss. More specifically, out of the 137,800 $ft^2$ that collapsed, 5,850 $ft^2$ were destroyed by blast and 58,100 $ft^2$ failed by progressive collapse (FEMA 439A, 2005).

The truck carrying the explosive was parked in close proximity to column G20 (Figure 1-3). As a result, this column failed by brisance (i.e., shattering) (Corley, 2008). This statement is supported by the fact that no evidence of this column was found among the debris or in the crater of the explosion (FEMA 277. 1996). Loss of this column removed support for the transfer girder on the third floor between columns G16 and G24. Analysis of the structure without column G20 showed that the structure could no longer be supported by the ordinary moment frame (FEMA 277, 1996).

Figure 1-3: The Alfred P. Murrah Federal Building (FEMA 439A, 2005)

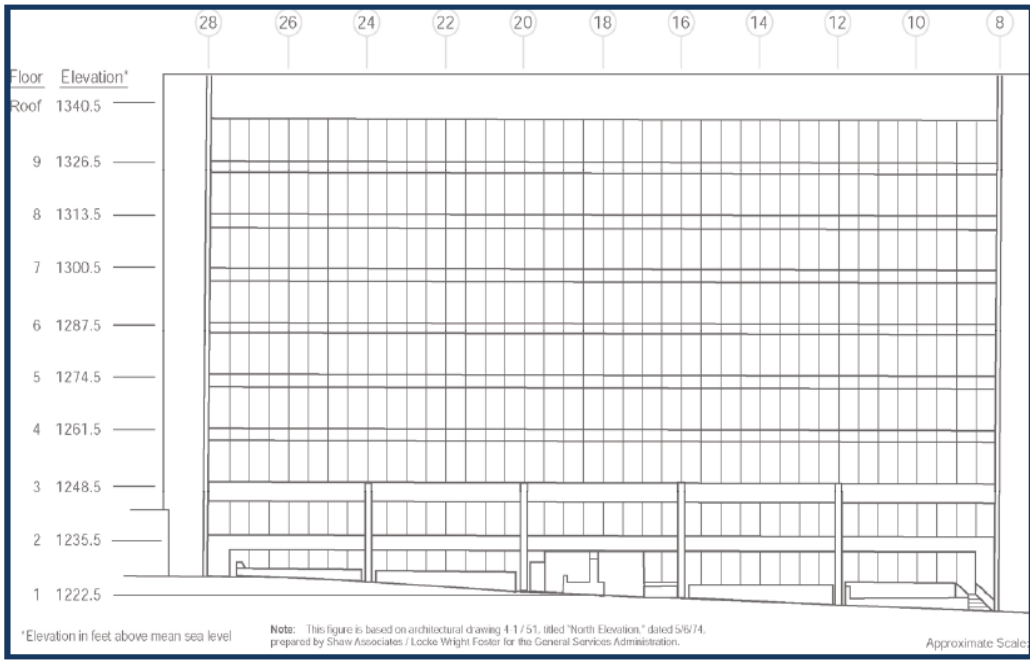


Figure 1-4: North Face Elevation (FEMA 277, 1996)

Columns G24 and G16 were located outside the range of the brisance, but they were quite close to the detonation and therefore were highly loaded. The strength of these columns was limited by the shear resistance at their ends. Due to the blast load, both columns underwent significant deflections and eventually failed in shear (Corley, 2008). Column G12 did withstand the effects of the direct blast (see Table 1-1).

Table 1-1: Blast Response of Intermediate Columns Supporting North Face Transfer Girder (FEMA 277, 1996)

| | Column Numbers | | | |
|---|---|---|---|---|
| | G24 | G20 | G16 | G12 |
| Slant Range (feet) | 37 | 21 | 50 | 89 |
| Peak Pressure (pounds per square inch) | 1,400 | 5,600 | 641 | 115 |
| Duration (milliseconds) | 1.3 | (1) | 1.7 | 1.4 |
| Deflection (inches) | 2.2 | (1) | 1.2 | 0.2 |
| Shear at Supports / Limiting Capacity | 1.8 | (1) | 1.0 | 0.1 |

(1) Column destroyed by brisance

As described previously, the structural components that were destroyed due to direct blast effects account for only a small amount of total collapse. The vast majority of failed floor space was attributed to progressive collapse. Eventually, all floors and roof panels bounded by column lines 12, 28, F and G collapsed.

Among the various papers and reports published about this terrorist attack, two noteworthy documents that deal with the structural response of the building will be briefly mentioned here. Both of these reports were developed by the Federal Emergency Management Agency.

The first document, FEMA 277 *The Oklahoma City Bombing: Improving Building Performance through Multi-Hazard Mitigation*, cited analyses performed by FEMA for the failure mechanisms of the Murrah Federal Building. Virtual work analyses showed that if any one of columns G12, G16, G20, G24 were removed, the third-floor transfer girder would collapse. In addition, this report concluded that many of the techniques used to upgrade the seismic resistance of buildings could also improve the ability to resist extreme blast loads and reduce the possibility of progressive collapse. These techniques mainly pertain to reinforcing details for special moment frames and mechanical splices for continuous load paths. It was suggested that had these techniques been implemented, the damage would have been reduced by 80%.

The second report, FEMA 439A *Blast-Resistant Benefits of Seismic Design*, evaluates the resistance of the Murrah Federal Building had it been designed for locations of high seismicity. Thus, it considers earthquake-resistant design techniques that can improve resistance to blast and progressive collapse. After assuming the San Francisco, CA downtown response spectrum and carrying out earthquake analyses, the report points out that the building was inadequately designed for a high seismicity zone. At this point, it should be emphasized that Oklahoma City, OK is not a seismically active region, and the building was well designed in accordance with 1970 era codes and provisions. In addition, rebar and concrete testing of the materials found among the debris following the attack showed the minimum strength values were well above the specified values (FEMA 439A, 2005). After the discussion on seismic-resistant design

procedures, FEMA 439A includes three potential longitudinal strengthening schemes: 1). A pier-spandrel system on the north face; 2). a special moment frame on the north face; and 3). interior shear walls. All three schemes were designed in accordance with ACI 318-02. As for the transverse direction, 12-inch reinforced concrete shear walls were placed between ventilation shafts at the east and west ends of the building. Blast response analyses were conducted using specialized software (ConWep, Span32 and WAC) (Army TM 5-855-1, 1998; Slawson, 1995; Biggs, 1964). A progressive collapse analysis was carried out as a nonlinear static analysis simply by imposing gravity loads and removing the elements that were found to fail during the blast analyses. Even though researchers argue whether seismic design practices can improve structural response against progressive collapse, Table 1-2 with the results of the progressive collapse analyses suggests that two out of the three longitudinal strengthening schemes could improve the behavior.

Table 1-2: Estimated Damage Based on Floor Area (FEMA 439A, 2005)

| Floor Level | Floor Area (SF) | Blast Damage (SF) | Progressive Collapse Damage | | | | |
|---|---|---|---|---|---|---|---|
| | | | Original Building (SF) | Pier-Spandrel Scheme (SF) | SMF Scheme (SF) | Shear Wall Scheme – Line F.5 (SF) | Shear Wall Scheme – Line F (SF) |
| Roof | 15,200 | 0 | 6,300 | 0 | 0 | 4,650 | 5,250 |
| 9th | 15,200 | 0 | 6,300 | 0 | 0 | 4,650 | 5,250 |
| 8th | 15,200 | 0 | 6,300 | 0 | 0 | 4,650 | 5,250 |
| 7th | 15,200 | 0 | 6,300 | 0 | 0 | 4,650 | 5,250 |
| 6th | 15,200 | 0 | 6,300 | 0 | 0 | 4,650 | 5,250 |
| 5th | 15,200 | 300 | 6,300 | 300 | 300 | 4,650 | 5,250 |
| 4th | 15,200 | 1,050 | 6,300 | 1,050 | 1,050 | 4,650 | 5,250 |
| 3rd | 15,200 | 2,100 | 7,000 | 2,100 | 2,100 | 4,650 | 5,250 |
| 2nd | 15,200 | 2,400 | 7,000 | 2,400 | 2,400 | 6,150 | 5,250 |
| Total | 137,800 | 5,850 | 58,100 | 5,850 | 5,850 | 43,350 | 47,250 |
| % of Total Floor Area Damaged | | 4% | 42% | 4% | 4% | 31% | 34% |
| % of Damaged Area Due to Blast | | - | 10% | 100% | 100% | 12% | 12% |
| % of Damaged Area Due to Progressive Collapse | | - | 90% | 0% | 0% | 88% | 88% |

### *1.2.3 World Trade Center (NY, 2001)*

The last progressive collapse incident that will be described in this thesis concerns the events of September 11, 2001. As a consequence of the intentional plane crashes that occurred in New York that day, 2,830 people were killed (FEMA, 2002).

Construction of the World Trade Center (WTC) began in August 1966 and was completed in 1972. The WTC towers, also known as the "twin towers" or WTC1 and WTC2, were the primary components of the WTC building complex. WTC1 and WTC2 were 417-m and 415-m high, respectively, with a typical story height of 3.7 m. The buildings were 63.1-m × 63.1-m in plan, with a rectangular core measuring 26.5-m × 41.8-m (Figure 1-5). The towers consisted of closely spaced 1-m exterior columns that

were connected to each other with deep spandrel plates (Figure 1-6). There were a total of 240 exterior columns.

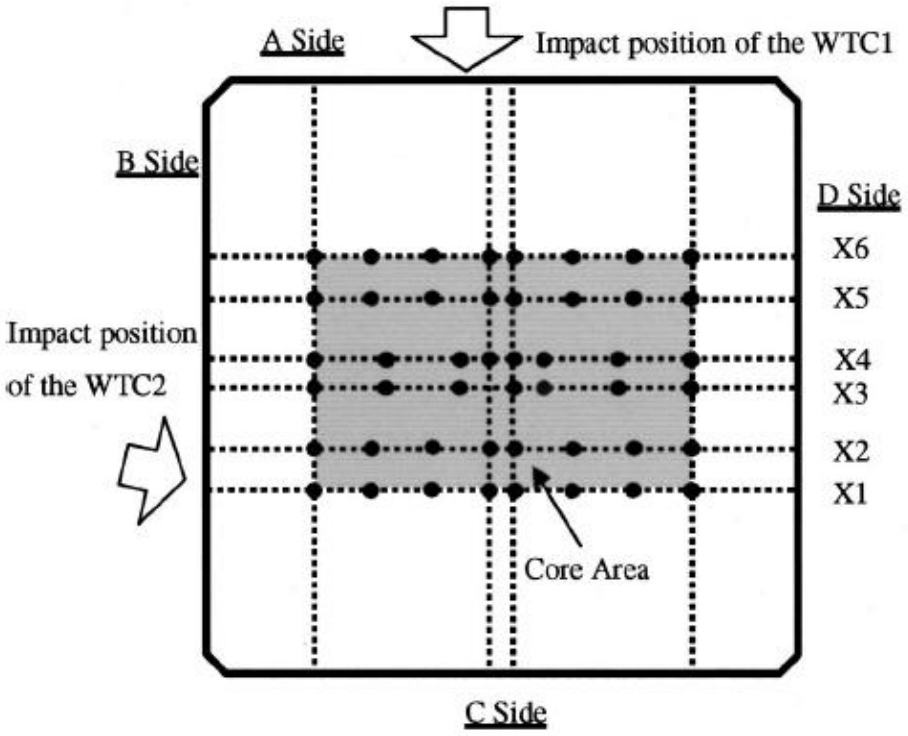


Figure 1-5: Plan View of the Structural System (Omika, 2005)

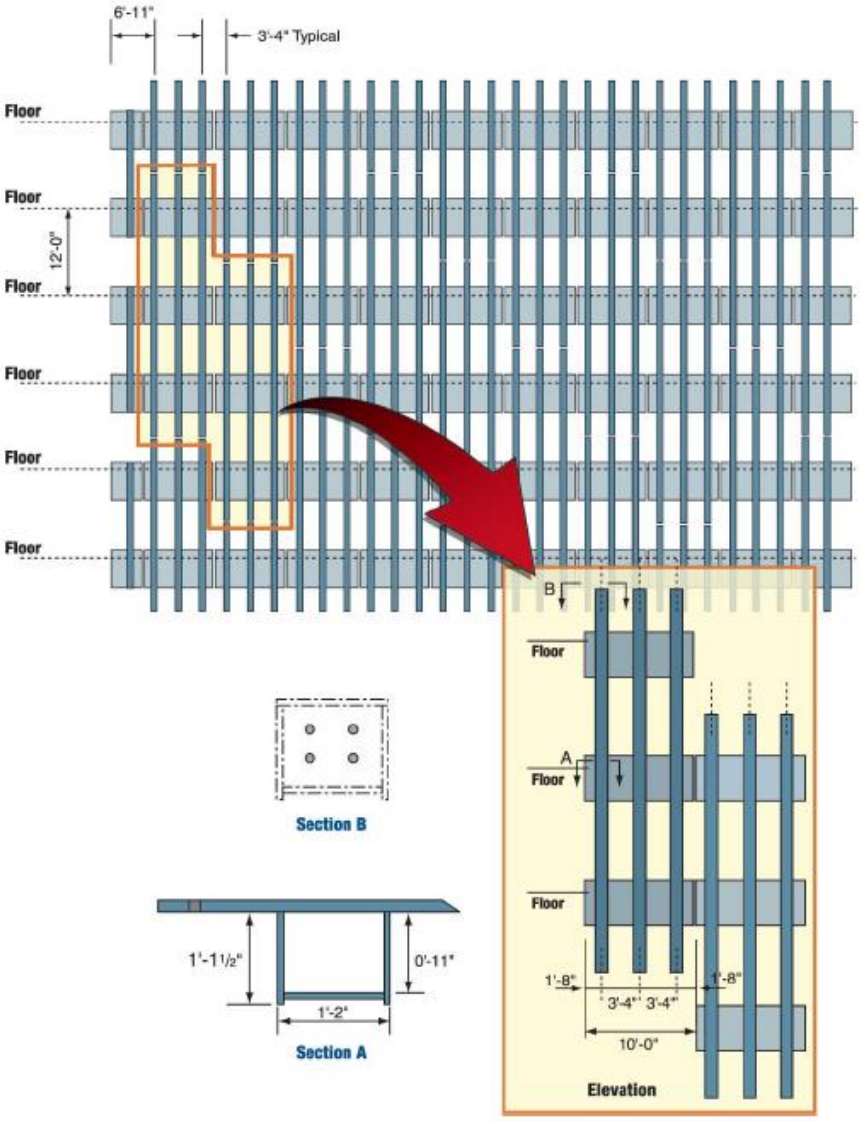


Figure 1-6: Partial Elevation of Exterior Bearing Wall Frame Showing Exterior Wall Module Construction (FEMA, 2002)

The core consisted of 47 columns that were connected to each other by small W-shape steel beams. The core supported 60% of the gravity load, while the exterior columns supported the remaining 40%. The exterior frames (columns and spandrel beams) also carried the design wind load. The composite floor slabs consisted of lightweight concrete and steel decks that were supported by steel-framed open web joists

connected to the perimeter columns of the core, as can be seen in Figure 1-7 (Corley, 2004; Omika, 2005).

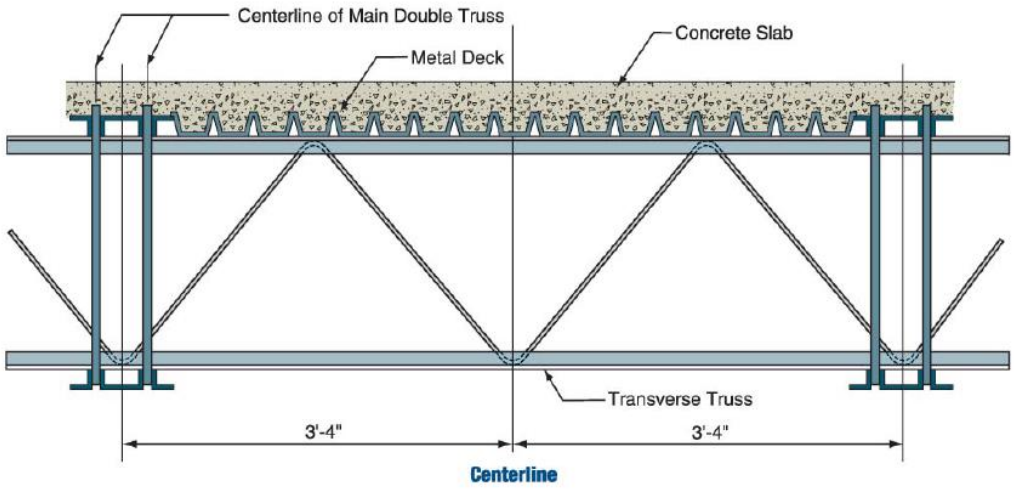


Figure 1-7: Floor System (FEMA, 2002)

On September 11, 2001, Boeing 767 planes crashed into WTC1 and WTC2. Specifically, a Boeing 767-200 crashed into WTC1 between the 94$^{th}$ and 99$^{th}$ floors flying at an estimated speed of 760 km/h. About 20 minutes later, a second Boeing 767-200 crashed into WTC2 between the 78$^{th}$ and 84$^{th}$ floors flying at an estimated speed of 950 km/h (FEMA, 2002). At the central zone of impact in WTC1, at least five prefabricated wall sections tore loose, and others we pushed inside. Additional damage was caused by the jet's wings. As a result, the tower experienced partial floor collapse (Corley, 2004). The impact's results were nearly the same in WTC2. A crucial point in the response is the fire that developed right after impact in both towers. It was estimated that temperatures reached as high as 1,100 $^{o}$C in some areas. There are different opinions among researchers concerning the sequence of the collapse events and the cause of the

collapse, but according to FEMA (FEMA, 2002) and Corley (Corley, 2004) the most dominant one is as described hereafter:

- The impact forces damaged certain columns that then lost their ability to carry loads. These loads were transferred to the undamaged columns, resulting in elevated stresses in those columns.
- Falling debris imposed heavy loads on the floor framing that were not accounted for in the original design.
- The high temperatures resulted in the expansion of floor framing and slabs. Therefore, additional stresses were developed in some elements.
- The high temperatures resulted in the loss of rigidity in certain elements. Therefore, some horizontal elements and floor slabs became tensile members, causing end connections to fail.
- The high temperatures also resulted in lowering the columns' yield strength. As a result, columns that were in close proximity to the fired buckled before reaching their specified buckling load under typical conditions.
- Once the floor collapse began, the stored potential energy in the floors was converted to kinetic energy impacting on the lower floors. The lower floors could not absorb the high impacting kinetic energy and therefore a progressive series of floor failures took place, resulting in the entire collapse of both WTC1 and WTC2.

It should be noted that the World Trade Center building complex was designed to resist the impact of a Boeing-707, which was the biggest commercial plane in existence when the buildings were built. Extensive investigations following the collapse (FEMA, 2002), along with high fidelity finite element simulations (Omika, 2005), made

it clear that plane impact was not the primary cause of the collapse. Lack of redundancy to mitigate the results of the initial impact was what led to the eventual disaster.

This event once again verified the need for robustness, alternative load paths, fireproofing, and ductile connection performance. Although the scale of this disaster was enormous and impacted the entire world, it is still debatable whether a plane impact is realistic design scenario.

## 1.3 RESEARCH MOTIVATION AND THESIS OBJECTIVES

The above mentioned examples are among the most well known progressive collapse incidents. They are highly related to the present research, and the purpose of citing them is to emphasize the importance and hazardous effects of progressive collapse. These examples, along with various other cases of progressive collapse inside and outside of the US that are not mentioned in detail here because they have been extensively presented by other researchers (e.g., L'Ambiance Plaza (Scribner 1988), Skyline Towers (Schellhammer 2013), etc.), have made professional structural engineers question the adequacy and the effectiveness of current code provisions. Some believe the current guidelines are not conservative and that further evaluation of structural robustness and resistance to progressive collapse should be studied. Conversely, other engineers think the current disproportionate collapse guidelines are too conservative and lead to unnecessarily costly designs. Current progressive collapse design guidelines measure resistance to an assumed column loss scenario, and quantitative response characteristics can be computed for this particular case. However, resiliency cannot be easily defined for general cases. Therefore, there is still much that is not known about progressive collapse. A better understanding of the collapse mechanisms and of the

components that enhance a structure's redundancy will give structural engineers the opportunity to reevaluate current code provisions and make them more effective and less costly. The vast majority of the studies conducted to date have been based upon a sudden column loss scenario (e.g., PCA, 2005; Astaneh, 2003; Yi, 2011). Among the few tests that have been conducted, the majority have focused on individual columns and beams without considering concrete slabs or steel decks. Most of the previous work on composite floor systems has been based on finite element modeling and numerical analysis rather than on lab tests (Sadek, 2008; Alashker, 2010). Significantly, only one other prior study actually utilized a composite floor system, meaning a steel beam that acts compositely with a corrugated metal deck and a concrete slab through means of shear connectors.

To develop general tools for determining the robustness and disproportionate collapse resistance of composite floor systems in typical buildings, the Department of Homeland Security (DHS) has funded the research project described in the current thesis. The research team's primary objectives are to determine the key elements that contribute to structural redundancy and to highlight the failure modes associated with the progressive collapse of a composite floor system under a sudden column loss. Loss of a single column is the initiating failure mechanism prescribed in the UFC guidelines (U.S. DoD, 2009) and several other specifications (CPNI, 2011; GSA, 2003). To meet the research objectives, a series of tests were conducted at the Ferguson Structural Engineering Laboratory at The University of Texas at Austin. The first test deals with an interior column removal scenario, while the second test pertains to a sudden perimeter column loss scenario of a typical steel-framed building. This thesis primarily focuses on the second test. Details of the first test can be found in Hull (2013).

Aside from the physical tests, high fidelity finite element models were created to evaluate and quantify the composite action of the floor system with the beams and the metal deck. This thesis includes an investigation of simple and computationally efficient ways to simulate composite action. The ultimate objective of this thesis and research project is to evaluate the current code provisions and to suggest possible modifications and additions to the code.

Following this initial chapter, Chapter 2 includes a detailed literature review. While general background information on progressive collapse is provided, the main focus of the chapter is on research that adopts a column loss scenario as a triggering damage case. Emphasis is given to those projects associated with composite floor systems. In addition, a brief overview of the finite element techniques utilized to simulate composite behavior are cited. In Chapter 3, an extensive and detailed description of the test setup and instrumentation of the second test is given. Chapter 4 primarily focuses on the testing procedure and interpretation of the measured results. In Chapter 5, the finite element modeling research is presented. The chapter includes validation of pull-out tests simulated with LS-DYNA, finite element material testing, proposed simulation techniques for modeling composite action (steel beam-shear stud-concrete slab) with LS-DYNA, and comments on the ability of the above mentioned software to simulate progressive collapse scenarios of composite floors. Finally, Chapter 6 includes further interpretation of the results, general comments, and conclusions.

# CHAPTER 2

# Literature Review

This chapter is divided into three parts. First, a brief overview of current code provisions and standards is provided. Second, a review of significant research conducted on the topic of disproportionate collapse is given, where the focus is on composite floor systems subjected to a sudden column loss. The third part contains a brief review of the modeling techniques that have been used so far by researchers to simulate composite action involving the interaction of steel beams and a concrete deck through shear studs.

## 2.1 CURRENT DESIGN METHODOLOGIES

One of the most widely used manuals for design against progressive collapse is the Unified Facilities Criteria (DoD, 2009). Three different approaches are included in this set of guidelines, and the choice is dependent on the level of risk and computational demand. The first method for mitigating progressive collapse is called the *Tie Force Method*. This method does not explicitly model the load bearing mechanism of a structure under a column loss. Instead, it requires a minimum amount of redundancy and reserve strength so that loads can be transferred to undamaged areas. There are two main force resisting mechanisms associated with the Tie Force method: 1). catenary action of beams, and 2). membrane action of floor slabs. In contrast with the previous version of UFC (DoD, 2005), the new UFC guidelines (DoD, 2009) allow designers to account for tie forces in the floor system rather than concentrated near beams and girders. This modification occurred due to the fact that the floor slab resistance is significant and due to the fact that the deformation demand in beams is too high if the tie steel is concentrated in these regions.

The second method is called the *Alternate Path Method*. This method divides the structure into primary and secondary structural components and requires the existence of an alternate load path in case one or more primary structural elements is lost. The structure may be analyzed for a set of progressive collapse scenarios (e.g., column removal) using linear static, nonlinear static, or nonlinear dynamic analyses. Apart from the distinction between primary and secondary elements, the structural components are also divided into force- or deformation- controlled. A force-controlled element is limited by the material strength, while a deformation-controlled element is limited by the maximum allowable inelastic deformation. All components must survive a progressive collapse analysis without exceeding their acceptance criteria. Secondary elements might be excluded from the model; however, their deformations must be checked. In the case of a static analysis, a dynamic impact factor (DIF) must be considered to account for the highly dynamic nature of progressive collapse. The dynamic increase factor is provided in the above mentioned code manuals. Its value depends upon the properties of the system being analyzed and is not a single constant.

The third design method specified in the UFC guidelines is the *Enhanced Local Resistance Method.* According to this methodology, critical structural members that are expected to sustain extreme loads such as blast loads or vehicle impacts are explicitly designed for those loads. The main characteristic of this method is that columns are designed in a manner that their shear capacity exceeds their flexural capacity. By doing so, it is ensured that brittle failure is avoided. This method, though effective, may lead to over-dimensioning of certain elements and increased costs. Further, because events leading to the failure of a key structural component are difficult to predict, there is significant uncertainty in ensuring that members designed for enhanced local resistance will perform as desired. The first method (tie force method) is often called an indirect

method, while the other two procedures are often referred to as direct methods. This is because indirect methods do not explicitly consider failure of a component or subsequent response (tie force method), while direct methods specifically consider the failure of a specific component (alternate path method and enhanced local resistance method). The above mentioned methods are not used as standalone procedures. Instead they are utilized in combination with each other, depending on the level of a structure's risk to undergo progressive collapse. For more details, the reader should refer to UFC (DoD, 2009).

The General Service Administration (GSA, 2003) has also provided methodologies for progressive collapse analyses. These methodologies employ scenario-based approaches and are similar to the UFC guidelines. The major difference between the DoD and GSA guidelines is the following: The DoD requires consideration of element removal at every floor. In contrast, the GSA requires an element removal only at the first floor (Elingwood, 2009).

## 2.2 PROGRESSIVE COLLAPSE RESEARCH

Several past studies have investigated the behavior of structural systems subjected to progressive collapse scenarios with particular focus on sudden column removals. Most past studies have been computational in nature, though a few significant experimental studies have also been conducted. Issues identified in the research literature include the following: factors that contribute to structural resistance against progressive collapse; beam-to-column connections; development of catenary, Vierendeel and membrane action; energy-based assessments of robustness and progressive collapse resistance; assessment of dynamic increase factors; and methods for mitigating the effects of disproportionate collapse.

Discrepancy exists among researchers and engineers for issues related to the DIF. Therefore, further research should be conducted towards this direction. Kim (2008) developed an integrated system for progressive collapse analysis using the nonlinear analysis software OpenSees. The program automatically evaluates the damage level of the members and creates a modified structural model for the next analysis step. Various structures with different column removal scenarios were analyzed, and the dynamic increase factor was determined. Based on Kim's analyses, this factor can be much larger than the one specified in GSA and DoD, depending on the modeling technique that is utilized. Converesely, Gannon (2009) performed a detailed study where concrete, steel, and wood structures were analyzed with all three UFC design methods. The authors concluded that the UFC specified DIF is conservative. The exact same conclusion was drawn by research conducted by Stevens (2011).

Various energy-based analyses have been resented in the literature to compare with the widely used force-based analyses. For example, Bazant (2007), identified the relationship between the impacting kinetic energy of falling floors and the energy absorption capacity of an impacted floor as the criterion for progressive collapse occurrence. He developed a dynamic, one-dimensional continuum model, which he applied to the 9/11 collapse of the World Trade Center towers. The computed results were consistent with the actual event, and he suggested the use of his model to evaluate various structural systems against their susceptibility to progressive collapse.

Szyniszewski (2009) analyzed a typical three-story building frame to investigate energy flow during progressive collapse. The analysis was carried out using the LS-DYNA finite element software, and an energy-based global stability criterion was established. The structure was subjected to the sudden removal of two columns after the static preloading phase was completed. Three different loading combinations were

investigated: 1.2*DL*+1.0L*L*, 1.2*DL*+1.5*LL*, 1.2*DL*+2.0*LL,* where *DL* is the dead load and *LL* is the live load. The goal was not to determine the maximum failure load but to identify the transition from a safely arrested collapse to a case in which collapse propagates. After evaluating the results, the author indicates that the force-based demand-capacity ratios widely utilized for progressive collapse investigation are much less accurate than the energy-based demand capacity ratios, which are sensitive to changes in structural behavior.

Significant research has also been carried out in the field of progressive collapse of concrete structures. Sasani (2008) investigated load redistribution and change in column axial forces by performing an actual progressive collapse test on the Hotel San Diego in San Diego, CA before its demolition. Bidirectional Vierendeel (frame) action of the longitudinal and transverse frames was identified as being the main factor contributing to the building's resistance. This mechanism resulted in the redistribution of the loads from the damaged to the undamaged columns, while adequate anchoring of the beams' reinforcement was found to be crucial for such a redistribution to take place. Sasani (2011) performed a similar experiment by exploding four neighboring first-floor and two perimeter second-floor columns of the Crowne Plaza Hotel, an 11-story building located in Houston, TX. Again, two-dimensional Virendeel action and flexural-axial response were identified as being the primary gravity load redistribution paths after the columns were removed. Other significant experimental and analytical studies of reinforced concrete structures subjected to column removal scenarios were performed by PCA (2005), Qian (2012), Orton (2013), and Bao (2013). All of these researchers identify catenary and Virendeel actions as the main resisting mechanisms of reinforced concrete structures against progressive collapse and concurrently question the

effectiveness of the value of the dynamic increase factor for progressive collapse analysis.

While the studies cited above provide valuable insight into the progressive collapse behavior of structural systems, the fact remains that limited information is available on the performance of typical steel-framed structures subjected to column removal scenarios. Because the failure mechanisms associated with steel members are different than reinforced concrete members, the results described above cannot be directly applied to typical steel-framed buildings. Nonetheless, some researchers have studied steel building behavior in detail, where this work has included both computational research and experimental studies. Among the various issues that have been identified as crucial in progressive collapse of composite floor systems, the ones of high interest are mainly the parameters that enhance the system's resistance and especially the contribution of the floor deck.

Foley (2007) used computational approach to address the issue of a center column loss of a composite floor system. The study's main goal was to identify and quantify the sources of progressive collapse resistance in structural steel framing systems. Three-story, 10-story and 20-story structures were analyzed, with special attention given to the study of catenary and membrane action. The computational results showed that the main parameters that enhance the resistance are moment connections, catenary action of steel beams, and membrane action of the floor deck. Slab reinforcement was found to be a key variable that significantly affects the deck's ability to develop membrane action. Overall, the composite floor systems studied by Foley were able to carry the dead and service live loads, but they were unable to carry these loads once the full dynamic load effect was considered.

Vlassis (2008) investigated the progressive collapse resistance of a multi-story steel building due to failed floor impact. The main idea of the study was that progressive collapse can be arrested if the imparted kinetic energy from a falling floor to a lower floor does not exceed the energy absorption capacity of the impacted floor. The study adopted the same principles that Bazant (2007) advocated. Vlassis' proposed framework involved three independent stages: 1). establishment of the nonlinear static response of the impacted floor systems, 2). a dynamic assessment approach to estimate the dynamic deformation demands, and 3). a ductility assessment during which the ability of the impacted floor to arrest the collapse was evaluated. The method was highly dependent on the estimation of the energy transfer, with limiting cases taken as fully plastic and fully rigid impact. The method was applied to a steel-framed composite building. Vlassis (2008) showed that a floor system within a steel-framed composite building with a typical configuration has a limited chance of arresting collapse due to impact from an upper floor.

Sadek (2008) investigated the robustness of a typical concrete deck-steel beam composite floor system under a center column loss scenario. The system utilized simple shear connections, and the analysis was carried out using LS-DYNA. Three different computational models were evaluated: 1). a detailed model wtih solid and shell elements, 2). a model with coarse shell elements, and 3). a reduced model where the beams and columns were discretized as beam elements and a series of nonlinear horizontal springs was used to simulate connection behavior. Apart from the maximum load the system could sustain, parameters such as the framing and metal deck contribution were investigated. The analyses showed that the primary resistance mechanism is the catenary action of the beams. Various failure modes were observed including fillet weld failure, bolt failure, block shear, and tear out failure. The floor deck

was found to have a significant contribution to the capacity through diaphragm and membrane action, as shown in Figure 2-1. Overall, this particular floor slab was found to be vulnerable to collapse under a center column removal, and the predicted capacity was much less than the value required by the GSA guidelines (GSA, 2003).

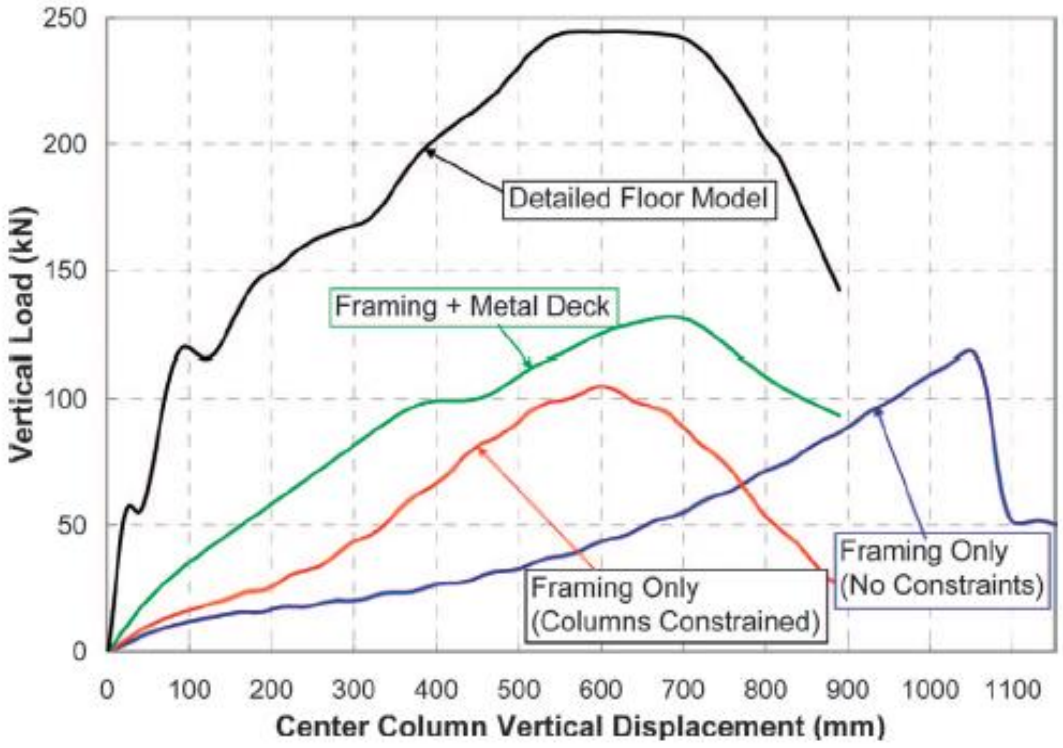


Figure 2-1: Applied Vertical Load Versus Center Column Vertical Displacement (Sadek, 2008)

Alashker (2010) performed a study to investigate the progressive collapse resistance of composite floors in which steel beams were attached to columns through shear tabs. The study built upon previous work done by Sadek (2008). The computational models were validated against extensive experimental data. Two different computational schemes were adopted. In the first approach, the center column stub was

pushed down using displacement control. In the second approach, the load was distributed uniformly over the slab using load control. The author investigated various parameters that affect resistance such as the effect of the steel deck, slab reinforcement, and shear tab connection strength. The results showed that the steel deck is the main source of the floor's capacity through membrane action. The strength of the shear tab connection was found to be unimportant.

Tan (2003) conducted an experimental study to investigate the capacity of a composite floor system to resist progressive collapse through catenary action. The test specimen was a single-story system, 20-feet wide and 60-feet long. The slab was placed 6 feet- 3.5 inches above the floor as shown in Figure 2-2. W18×35 longitudinal beams, W21×44 transverse beams, and W14×61 columns were used. ASTM Grade 36 steel was used for all sections, and the concrete slab had a specified unconfined compressive strength of 4 ksi.

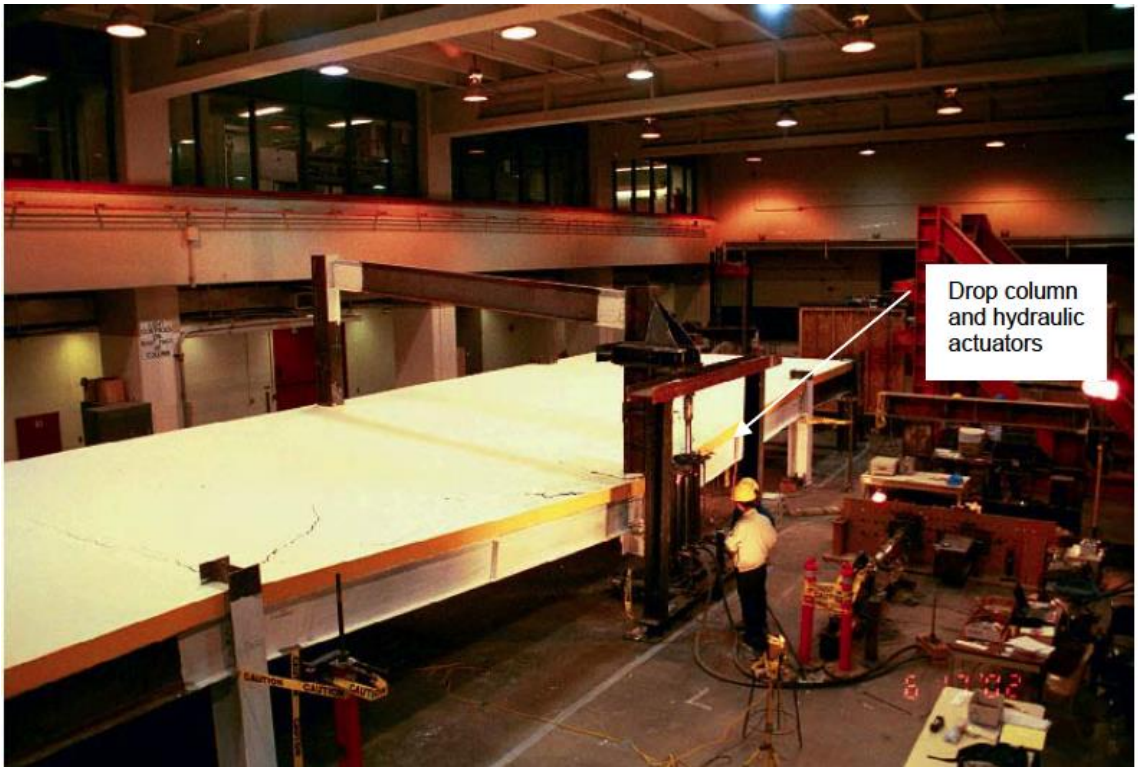


Figure 2-2: Test Specimen (Tan, 2003)

To simulate a columns loss, two hydraulic actuators were used (Figure 2-2). Because the test specimen was placed close to the floor, the center columns could deform no more than 36 inches before contacting the laboratory floor. The test was terminated when the drop column reached its maximum displacement without failure of the structure. The only observed failure was fracture of the weld on the east beam shear tab. The same research team performed two more tests trying to investigate a cable retrofit method against progressive collapse. Indeed, the retrofit helped the structure to sustain much higher load for the same maximum deflection. However, because the structure did not fail during any of the tests, it is difficult to draw detailed conclusions regarding the failure modes, its catenary action, and the cable retrofit.

Song (2009, 2010, 2012) conducted experimental and computational research on the progressive collapse behavior of two actual buildings. The structures were scheduled for demolition and did not carry any live load. Four first-story columns were removed. None of the buildings collapsed. Based on elastic-static and nonlinear dynamic analyses that were conducted, however, it was found that one of the two buildings did not conform with the GSA (2003) guidelines. This finding suggests that there might be extra capacity in structures with composite floor systems and that current analysis guidelines are not able to capture the actual capacity available in these systems. Therefore, more detailed analysis approaches may be needed. In addition, the authors verified that 3-D analyses are much more accurate than 2-D analyses, and they also showed that dynamic analyses are more accurate than static analyses. They also pointed out that the dynamic impact factor specified by DoD (2005) and GSA (2003) is somewhat conservative.

## 2.3 COMPOSITE ACTION SIMULATION

As suggested by several of the research studies cited in the previous section, an important aspect in progressive collapse modeling is the simulation of composite floor system behavior. Specifically, composite behavior is defined as the interaction between the steel beams and the concrete slab. In most cases, this interaction is achieved through the use of steel shear studs that are welded to the top flange of the steel beams and embedded in the concrete slab.

As described in the previous section, many researchers that study progressive collapse from a computational perspective use LS-DYNA. This software is preferred because its explicit dynamic solver makes it effective for analyzing highly dynamic loadings like those associated with sudden column removal. Other commercial software such as ABAQUS and ANSYS, however, have also been adopted by researchers to

simulate composite action and study progressive collapse. Due to high computational demands, most researchers have chosen not to create full three-dimensional models (steel beams-shear studs-concrete slabs and possibly metal decking), but instead utilize reduced representations of the exact models.

Li (2011), in his study on the effects of three-dimensionality in progressive collapse behavior, modeled the shear connectors with rigid links and the concrete slab using fully integrated four-noded isotropic shell elements, as shown in Figure 2-3. The software used was LS-DYNA.

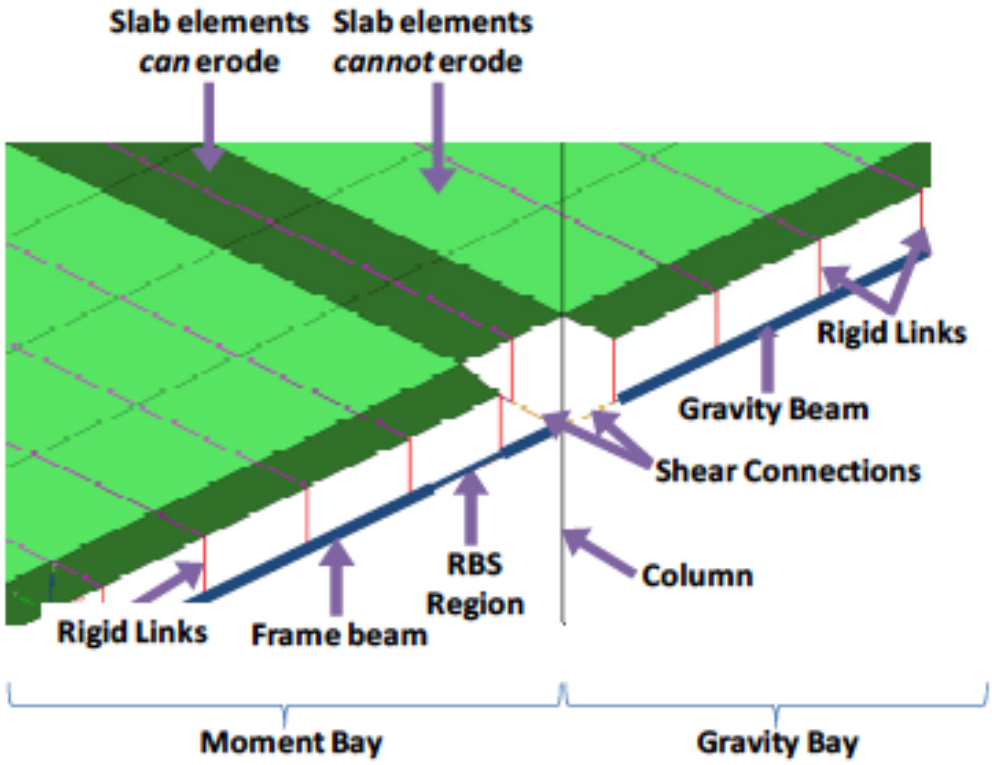


Figure 2-3: Close up of Connection Region (Li, 2011)

Patil (2013) conducted a computational parametric study to investigate the effect of shear stud dimensions and configuration in the response of composite floor systems. ANSYS software was used for this study. The concrete slab was discretized using solid elements, the steel beams were modeled using shell elements, and the shear studs were represented by beam elements. The results were validated against code provisions and experimental data, and good agreement was found to exist. Queiroz (2006), also using ANSYS, investigated composite beam behavior. He used solid elements to discretize the concrete slab, shell elements for the steel beam, and a nonlinear spring element to represent the shear connectors. This particular element is defined with a user-specified force-deflection curve. The configuration can be seen in Figures 2-4 and 2-5.

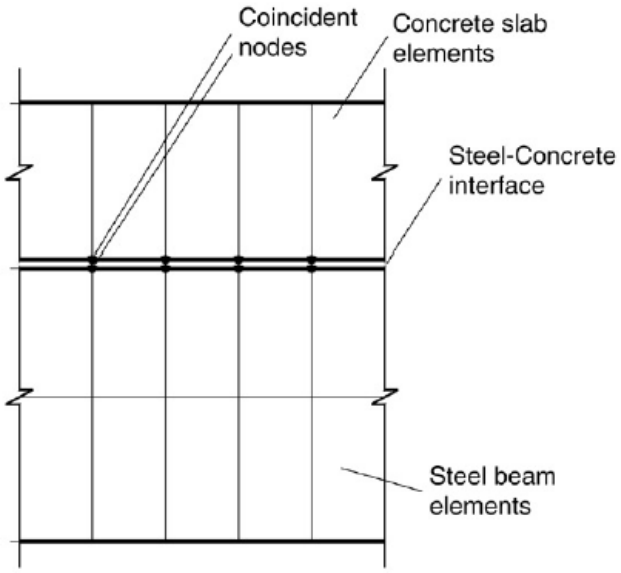


Figure 2-4: Shear Studs in a Typical Composite Beam Finite Element Mesh (Queiroz, 2006)

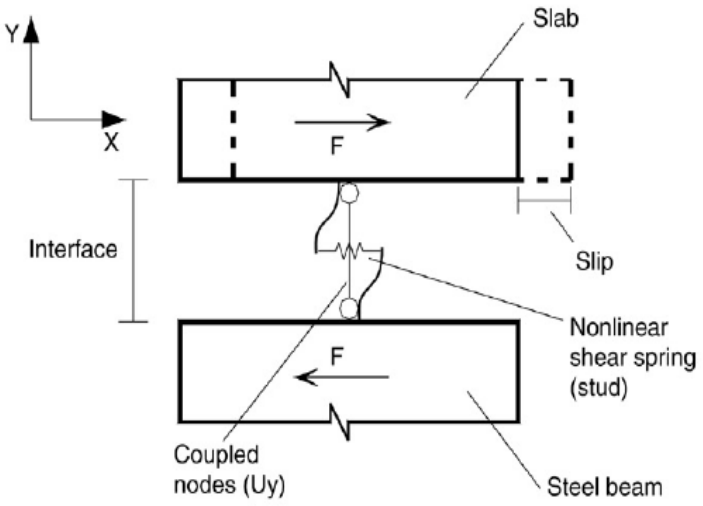


Figure 2-5:Representation of the Shear Stud Model (Queiroz, 2006)

Finally, Lam (2005) and Prakash (2011) investigated the behavior of headed stud shear connectors in composite beams using ABAQUS. Both research teams utilized full three-dimensional models, meaning that solid elements were used for all steel beams, concrete slab, and shear connectors (Figure 2-6). The test results were validated against experimental data, and good correlation was observed. These models were found to be more accurate than the previous ones, the analysis time, however, was more than twice the analysis time of the previous models.

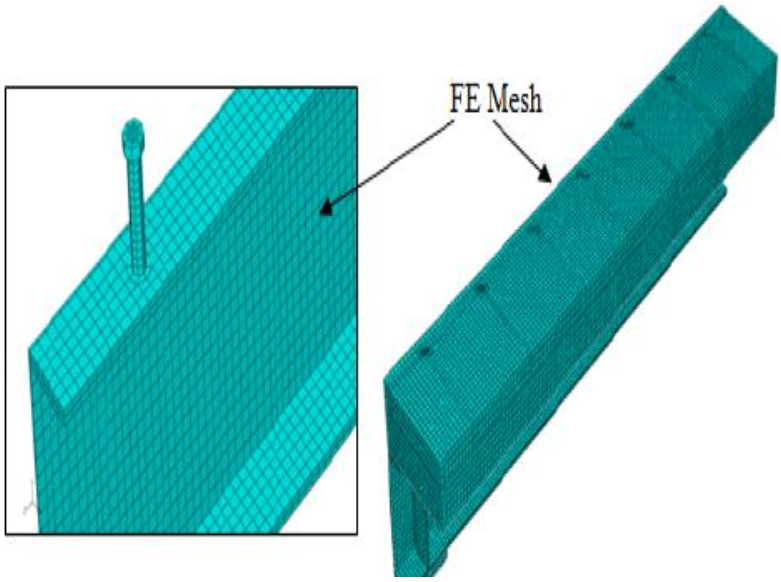


Figure 2-6: a) Steel Beam with Shear Connectors on Top, b) Full Model (Prakash, 2011)

## 2.4 SUMMARY

Although significant computational work has been conducted on the progressive collapse analysis of steel and composite structures, the literature still lacks a sufficient amount of experimental data to support the computational results. The load distribution and the development of membrane action are still untested areas. In addition, discrepancy exists among researchers and practicing engineers regarding whether the current code provisions are conservative or not, and the value of the dynamic increase factor has yet to be verified experimentally. Therefore, full-scale tests of composite floor systems loaded to collapse are needed.

It can also be seen that significant computational work has been conducted to validate various composite behavior simulations using the commercial software packages ANSYS and ABAQUS. However, limited data exist on how well LS-DYNA can capture composite behavior, utilizing either full three-dimensional models or simplified models that adopt shell and beam elements to reduce computational demands.

As mentioned previously, emphasis in this thesis is placed on LS-DYNA because it is widely accepted by engineers for progressive collapse analysis. Therefore, the validation of the composite behavior using this particular software is imperative.

The above mentioned issues will be addressed in the present study. Chapters 3 and 4 focus on the full-scale test performed within the current research project that attempts to shed light on the progressive collapse behavior of composite floor systems. Furthermore, in Chapter 5, a validation of the composite behavior simulation with LS-DYNA is presented so that possible computational deficiencies of this particular software can be identified.

# CHAPTER 3

# Experimental Setup

## 3.1 SPECIMEN DESIGN

This chapter provides a description of the test specimen, experimental setup, loading system, and instrumentation. The structural engineering firm Walter P. Moore provided assistance by designing a prototype building according to their office's standard details. However, due to practical constraints that had mainly to do with the available space at the Ferguson Structural Engineering Laboratory at UT Austin and the available project budget, the prototype building had to be reduced in size. Using a similar design approach as that taken by Walter P. Moore, the research team chose to design and construct a steel gravity frame with approximately 15-ft bays and secondary floor beams at the midspan of each bay. For the floor, the research team chose to use corrugated steel decking with a cast-in-place concrete slab. An external frame was utilized to provide lateral restraint (Figure 3-1).

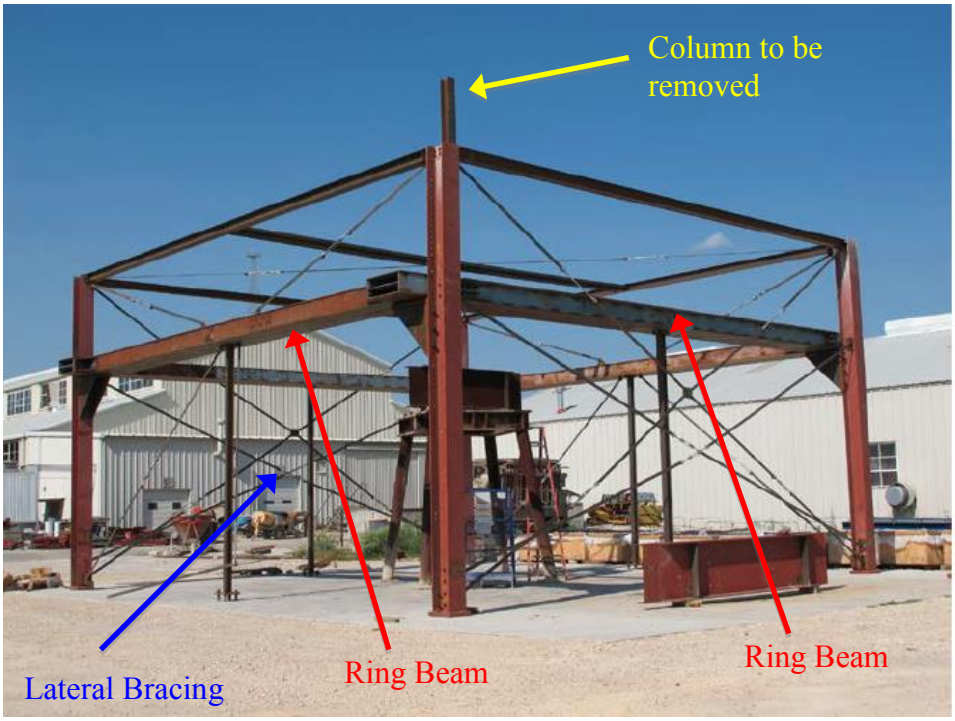


Figure 3-1: External Frame Before Construction of the Specimen

The loads considered for the test included a dead load (*DL*) of 75 psf and a live load (*LL*) of 50 psf. In addition, a uniformly distributed line load acting along the edge of the specimen having a dead load equal to 320 plf was utilized to simulate the effect of a façade. According to the UFC guidelines (DoD, 2009), the load combination for progressive collapse analysis is $1.2DL + 0.5LL$. The test, however, was carried out statically. Therefore, a dynamic increase factor should be taken into account to determine the collapse load based on the UFC provisions (DoD, 2009). Due to the fact that progressive collapse is an extreme event, the structure should not be designed to remain in the elastic region. Consequently, the design approach the research team adopted was a nonlinear static analysis. The DIF was determined based on the procedure described in paragraph 3-2.15.5 of the UFC. The yield rotation ($\theta_y$) was calculated based

on Equation 5-1 of ASCE 41-06 (ASCE, 2006), and the plastic rotation angle ($\theta_{pra}$) was determined according to Table 5.6 of ASCE 41-06 for three different levels of protection: Immediate Occupancy, Life Safety, and Collapse Prevention. The corresponding DIF values were 1.58, 1.22, and 1.18, respectively, resulting in an average value of 1.33. Therefore, the research team estimated the final collapse load based on the UFC guidelines to be 1.33(1.2*DL* + 0.5*LL*). A detailed calculation of the DIF can be found in Appendix A.

### *3.1.1 Structural Steel Framing Members*

All structural framing members were specified to be ASTM A992 steel. The layout of the members is shown in Figure 3-2. The W12×14 girder spanned north to south. The secondary W6×9 beams framed in at the girder midspan. The corrugated steel deck spanned 7.5-feet north to south between the secondary beams. Around the perimeter of the external frame, there was a large and heavy ring beam, as can be seen in Figure 3-1. The specimen's exact dimensions were 29-feet–11-inches by 14-feet–11.5-inches. All beams and the girder were connected directly to the ring beam.

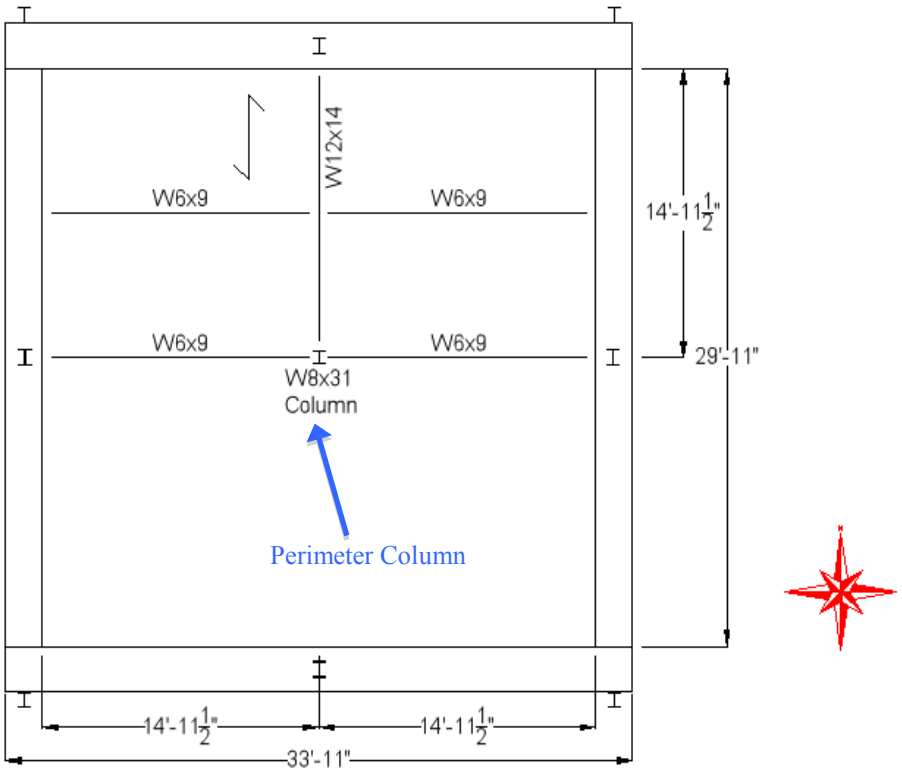


Figure 3-2: Plan View of Test Specimen

A W8×31 section was used for the perimeter column. The column extended 18-feet–6-inches up from the bottom of the floor system. The perimeter column was supported by a hydraulic actuator. Details of the perimeter column and the actuator are shown in Figures 3-3 and 3-4.


Figure 3-3: Perimeter Column, Lateral Bracing, and Actuator


Figure 3-4: Perimeter Column Connection

Shear connections were utilized for all framing members. The girder and the primary beams were attached using double angles at each end, while the secondary beams were connected to the girder and the ring beam with shear tabs. All angles and plates were specified to be ASTM A36 steel. Details are shown in Figures 3-5, 3-6, and 3-7.

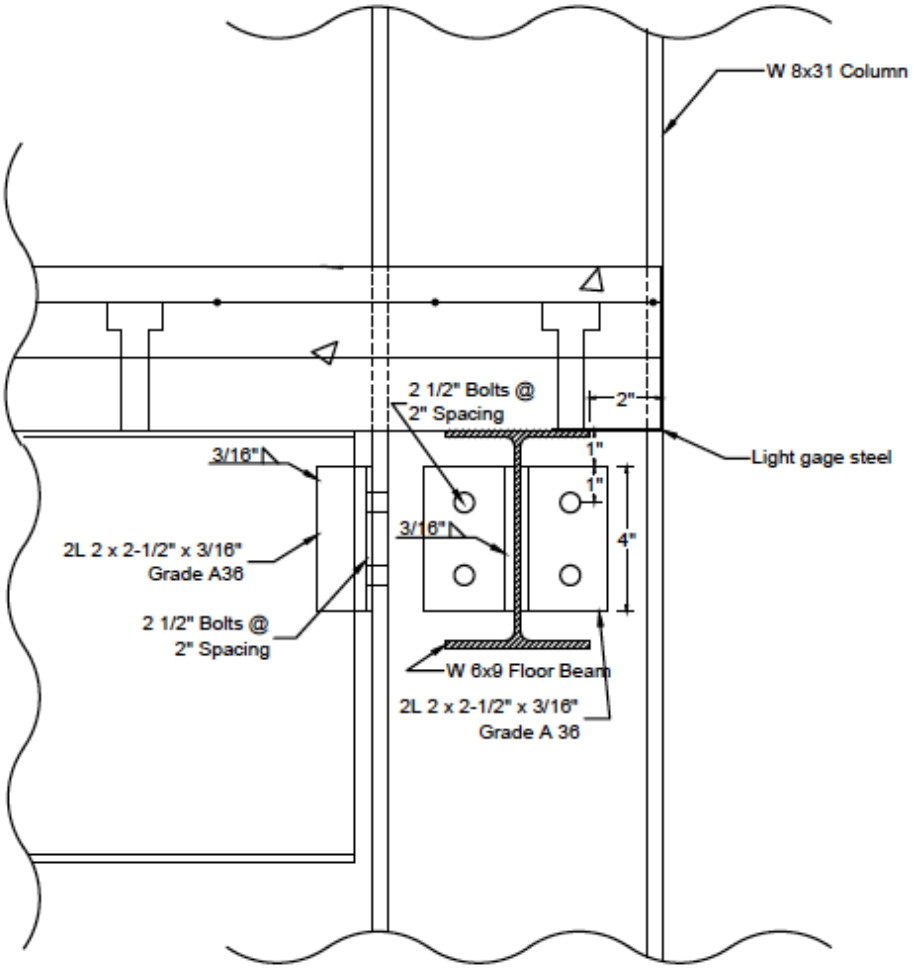


Figure 3-5: Girder-to-Column Connection Detail

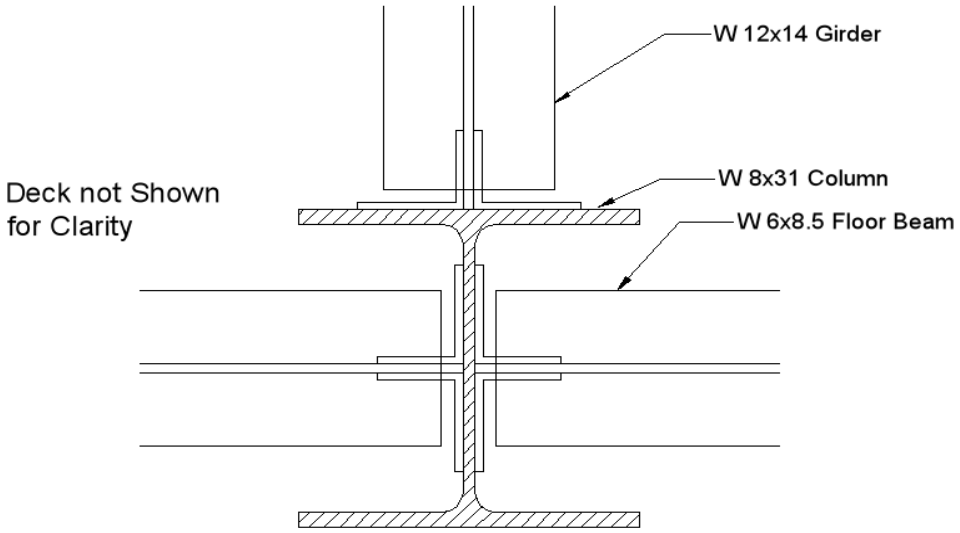


Figure 3-6: Girder and Floor Beam-to-Column Connection Detail (plan view)

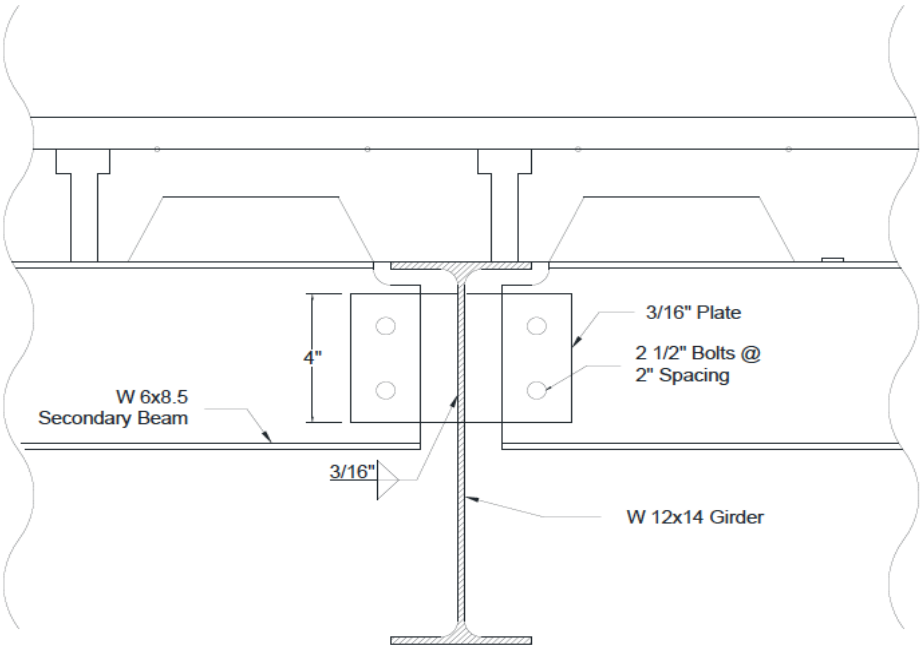


Figure 3-7: Secondary Beam-to-Girder Shear Tab Connection

The angles were welded to the beams and girder using 3/16-inch fillet welds with E70 electrodes and were subsequently bolted to the column. Two ASTM A325 bolts were used for each angle.

### *3.1.2 Composite Floor System*

The composite floor system consisted of 22-gage steel floor decking with 2-inch deep corrugations. The concrete slab was 4.5-inches deep, measuring from the bottom of the ribs, and the specified compressive strength was 3.5 ksi. Concrete was cast on March 26, 2013. During the concrete casting and the entire construction phase, wood shoring was used for safety, as shown in Figure 3-8.


Figure 3-8: Wood Shoring During the Construction Phase

As far as the slab reinforcement is concerned, welded wire mesh was placed to provide resistance to cracking caused by temperature changes and shrinkage. To position the wire mesh at the desired height, chairs were used. Along the entire length of the girder, #3 reinforcing bars were placed at 12 inches, per the recommendation of Walter P. Moore (Figure 3-9). Identical reinforcement was also placed along the perimeter and at the four corners of the floor system, as shown in Figure 3-10.

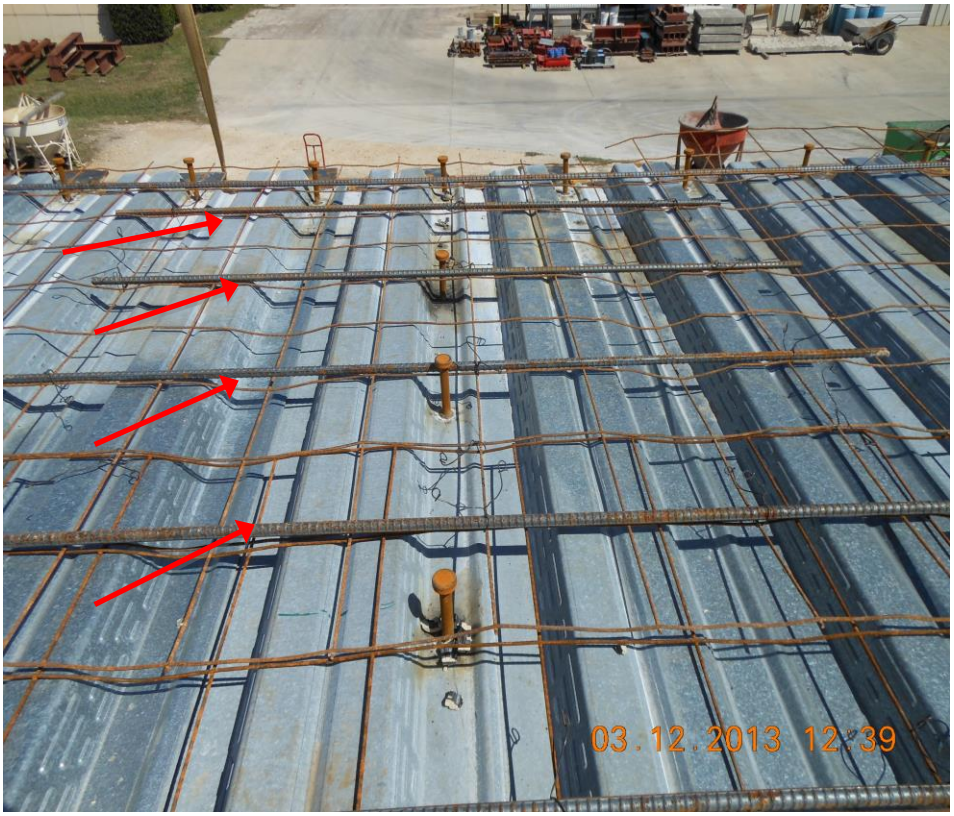


Figure 3-9: #3 Reinforcing Bars along the Girder

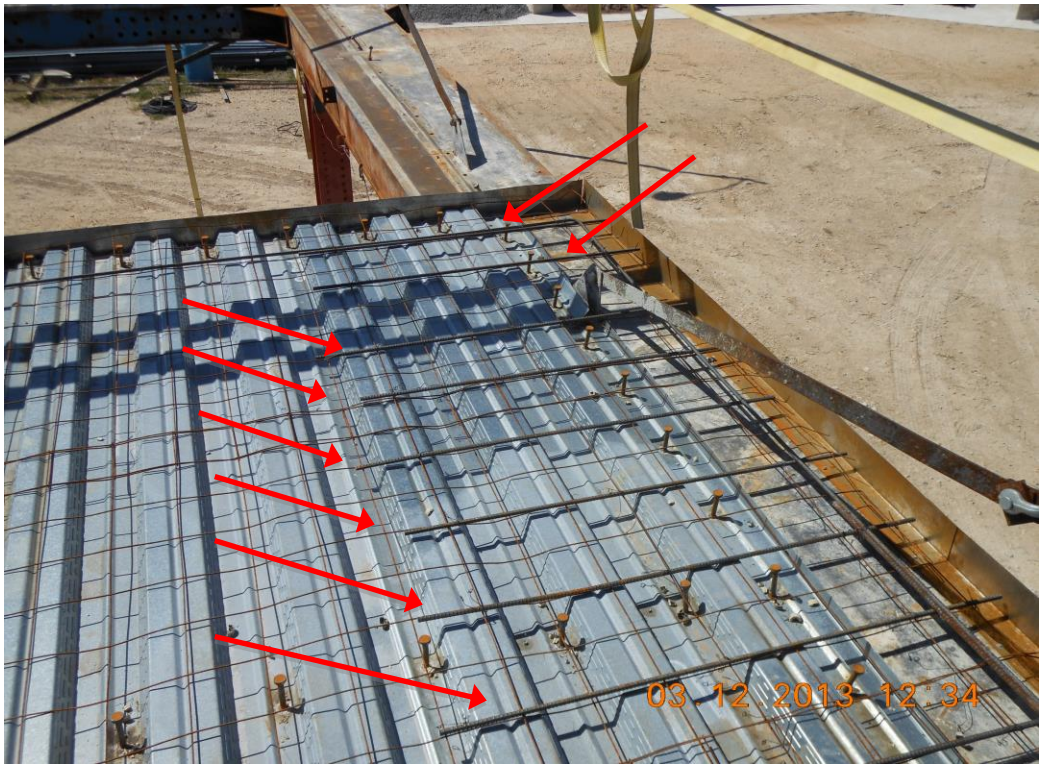


Figure 3-10: #3 Reinforcing Bars along the Perimeter

Additional details of the floor system are shown in Figures 3-11 and 3-12.

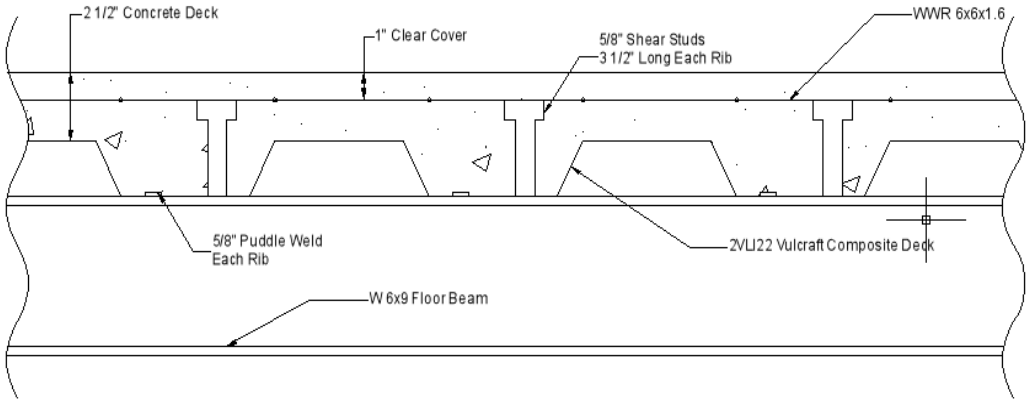


Figure 3-11: Composite Floor Detail over Floor Beam

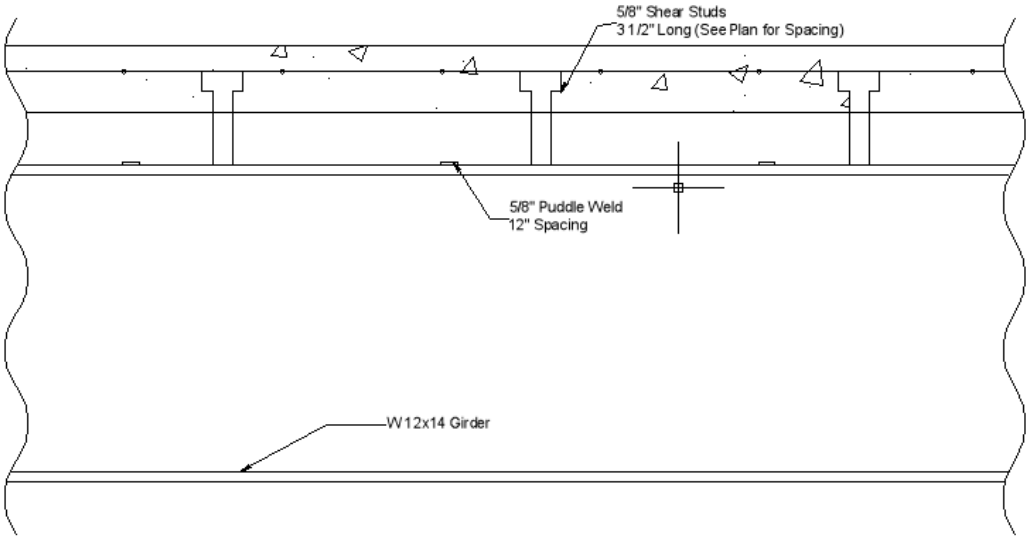


Figure 3-12: Composite Floor Detail over Girder

The longitudinal seams of the corrugated steel deck ran parallel to the girder, north to south. The width of the corrugated steel deck strips was 3 feet. Therefore, 4-inch side laps were required along the east-to-west direction. These side laps were attached to each other with self-drilling TEK screws. Self-drilling TEK screws were also used to attach the decking to the steel framing system prior to the installation of the shear studs. Shear studs were used to establish composite action between the floor slab and the steel framing components. The studs were 0.5-inch in diameter and 3.5-inches long. Along the east-to-west direction, the shear studs were placed at each low flute of the deck, resulting in an approximate spacing of 12 inches. Along the north-to-south direction, the studs were also placed 12 inches apart. At the side laps, the studs were welded directly through both sheets of corrugated decking.

### *3.1.3 External Frame*

As mentioned previously, the test specimen was configured to simulate the sudden loss of a perimeter column. Due to the fact that space limitations prohibited the construction of a full building, the boundary conditions were of primary importance. A heavy steel ring beam was placed along the perimeter of the specimen (Figure 3-1) to simulate the restraint offered by neighboring bays in a manner that was representative of the prototype building. The details of the east-to-west ring beam can be seen in Figure 3-13. The only difference between the east-to-west and north-to-south ring beams is the cross section used. A W27×84 section was used for the east-west ring beam, while a W27×94 section was used for the north-south direction.

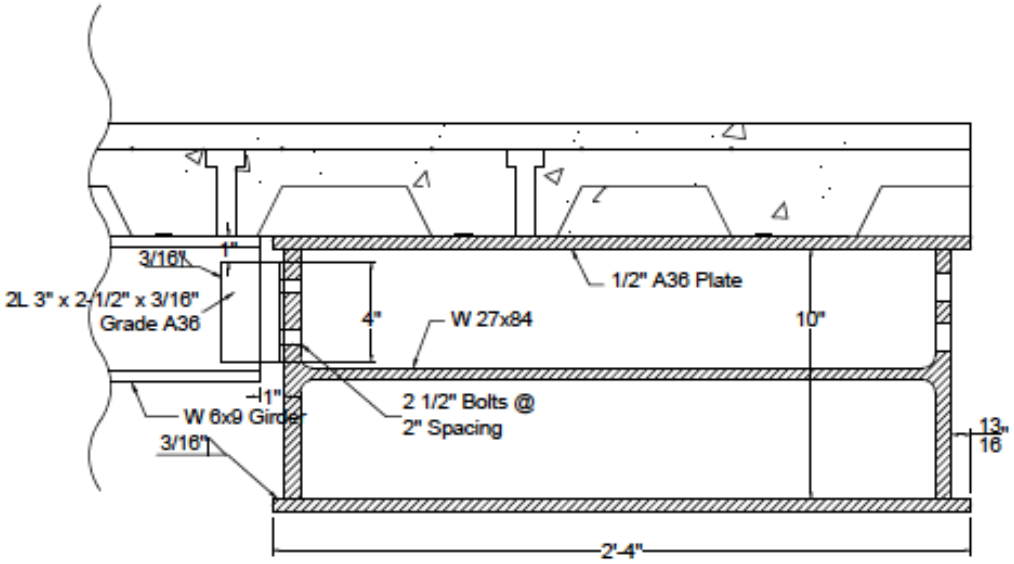


Figure 3-13: East-to-West Ring Beam Cross Section

To resist horizontal flexure, each beam was placed on its weak axis so that the strong axis was parallel to the plane of the slab. Steel plates with a thickness of 0.5 inch were welded to the top and bottom of the ring beam to increase its rigidity. In addition, steel gusset plates were used to provide extra lateral and vertical resistance to the ends of

the ring beams (Figure 3-14). It is noted that the rigidity of the north-to-south ring beams differed from the east-to-west beams due to the differences in their detailing. While the ring beam is used to simulate the continuity between adjacent bays in an actual building, it cannot capture this behavior exactly. This is due to the fact that this configuration cannot account for all the various floor systems and column removal locations. The ring beam, however, is well suited for idealized laboratory conditions and allows for a repeatable test setup. Furthermore, using the collected data to validate computational models, results form this test program can be extended to actual floor systems. Therefore, the stresses and deformations of this beam were monitored during the test so the demand that would be placed on actual floor systems could be estimated.


Figure 3-14: Ring Beam Corner Detail

The main floor girder and beams framed directly into the ring beam. The composite floor slab was connected to the ring beam through one row of shear studs placed 12 inches apart. A high factor of safety was used for the entire external frame to ensure failure would occur only within the specimen and not in the external restraining frame.

## 3.2 LOADING SYSTEM DESIGN

The testing procedure was divided into two separate loading stages. During the first stage, the perimeter column (actuator) was gradually lowered. During the second stage, additional load was applied to the floor slab until it collapsed. For the column lowering stage, the floor slab was allowed to stabilize after each 0.5-inch displacement increment. This procedure was repeated until the actuator was fully disengaged from the floor system. This forced the structure to redistribute forces as the reaction was removed. During this stage of testing, the floor slab was loaded with 115 psf, which is the UFC (DoD, 2009) design load for progressive collapse. Although a dynamic impact factor was previously calculated to be equal to 1.33, this was only an estimate, and its adequacy will be analyzed later based on the test results. Consequently, the team members decided to initially load the structure ignoring the DIF. Further details about the testing procedure are given in the next chapter.

Prior to testing, the research team estimated that the floor system would survive the initial column removal with the unamplified progressive collapse design load. Therefore, the research team sought a loading system that could provide additional load beyond that imposed during the initial stage of loading. In addition, it was imperative that this mechanism could keep this load evenly distributed over the slab and that the

load could be measured with acceptable accuracy so the researchers could determine its ultimate value. The research team estimated the maximum load the structure could accommodate was 150 psf. To achieve this level of loading, two large plastic swimming pools were placed on the slab as shown in Figure 3-15.

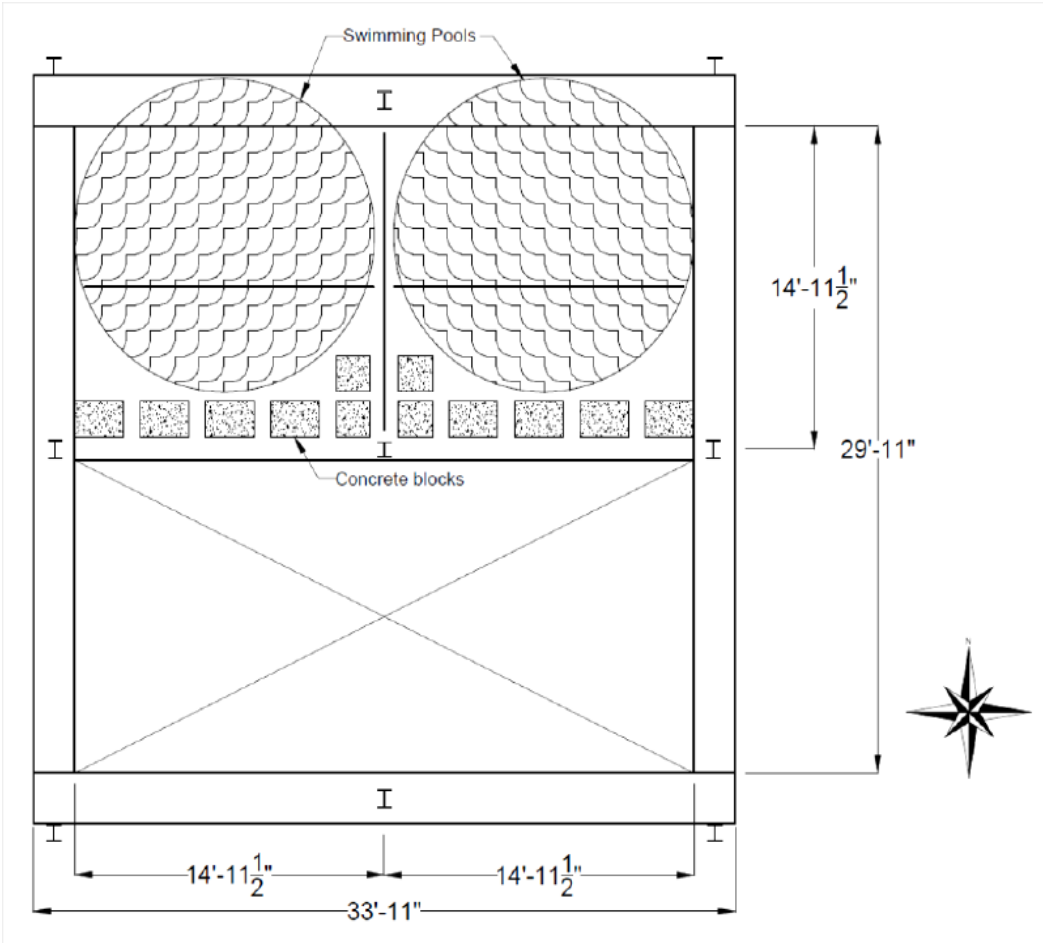


Figure 3-15: Loading System

The swimming pools, when fully loaded with water, could accommodate a total load on the floor of 270 psf, which is much larger than the predicted ultimate design

load. As mentioned before, this test was performed to simulate a perimeter column removal scenario. Therefore, a loading system that simulates an external wall or façade was also sought beyond the uniform load applied by the pools. The solution selected to simulate the façade load was to use 20-incs×20-inch×28-inch concrete blocks along the external edge of the structure (Figure 3-15). Each concrete block weighed approximately 950 lbs, and the load per unit length was approximately 320 plf.

A third pool located near the structure was used to store the water required for the testing. This pool was placed a safe distance from the test specimen, and PVC piping and water pumps were used to create an irrigation system that could distribute water equally to the two loading pools. Additional details about the testing procedure and sequence are provided in the next chapter.

## 3.3 TEST SPECIMEN INSTRUMENTATION

Throughout testing, data was collected at a rate of 1 Hz. The values of primary interest were the loads, vertical displacements, horizontal displacements, and strains.

### *3.3.1 Load Measurements*

To measure the total load supported by the actuator, a 50-kip load cell was used (Figure 3-16). The load cell measurements were recorded from the time the test started until the point the actuator was fully disengaged from the floor slab (after that point no meaningful measurements could be extracted). To measure the additional load after column removal, flow meters were directly connected to water pumps so the total volume of water distributed to the two loading pools could be measured (Figure 3-17).


Figure 3-16: Load Cell

Figure 3-17: Flow Meters

### *3.3.2 Vertical Displacement Measurements*

String potentiometers were used to measure the vertical displacement of the test specimen at eleven key locations (see Figure 3-18). Two potentiometers were placed on the north side of the actuator for redundancy in case the main potentiometer was destroyed. The capacity of the potentiometers placed on the beams and girder was 62 inches, while the capacity of the potentiometers placed around the perimeter column was 125 inches. The potentiometers rested on the concrete slab below the test specimen. The cables were fully extended and connected to the appropriate member using wire that was attached to brackets glued to the bottom of each beam. The instruments were attached at the middle of the beam bottom flanges. As far as the column is concerned, the string potentiometers were connected to steel plates that provided clearance from the actuator (Figure 3-19).

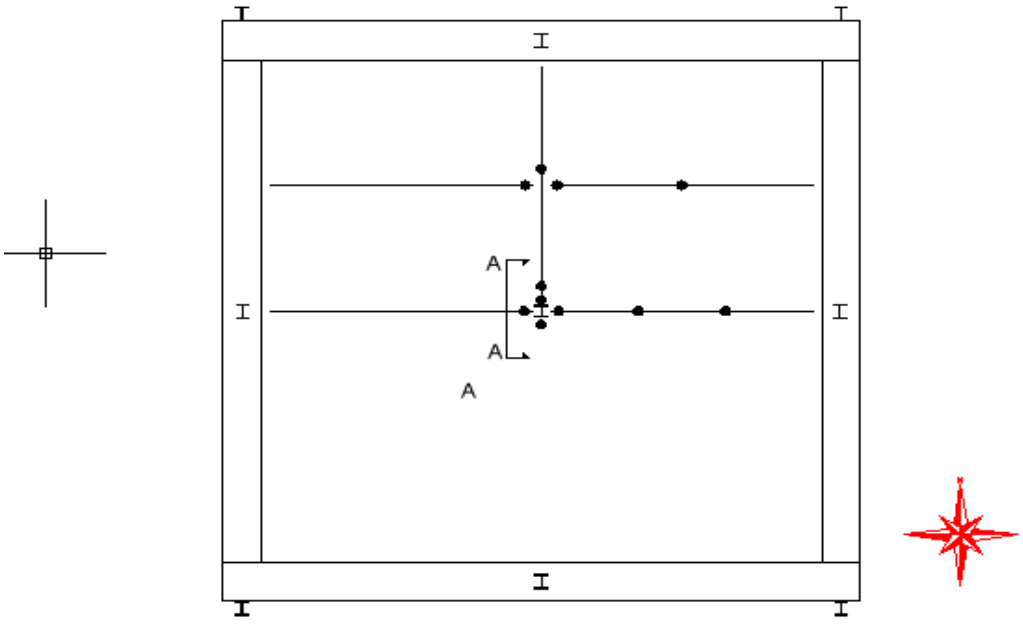


Figure 3-18: Vertical Displacement Transducers


Figure 3-19: Plate Providing Clearance from Actuator and Linear Potentiometers

### *3.3.3 Horizontal Displacement Measurements*

Linear potentiometers with a 7-inch stroke were used to measure the horizontal displacements. The potentiometers were attached to the top and bottom of the beam and girder webs as shown in Figures 3-19 and 3-20.

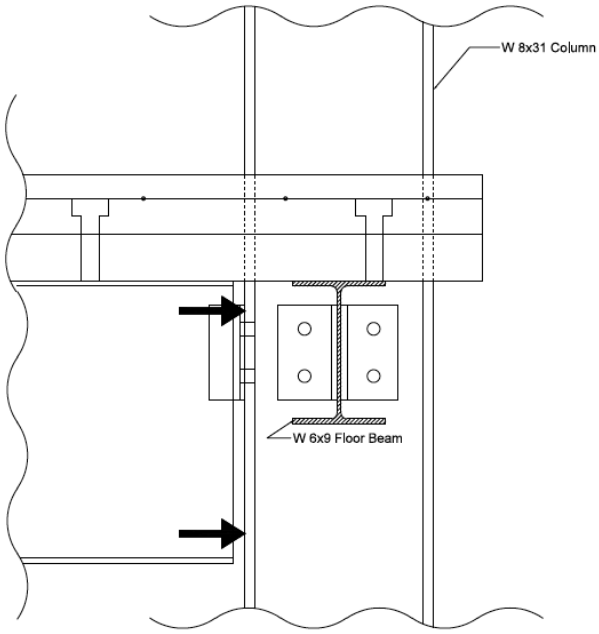


Figure 3-20: Sketch of Horizontal Linear Potentiometers

To enhance the accuracy of the calculated rotations, the vertical spacing of the potentiometers was maximized.

### *3.3.4 Strain Gages*

To measure strains and estimate the induced bending moments, strain gages were placed on the girder, on the ring beam, and on the floor slab. The girder was instrumented with eight strain gages at midspan. The gages were offset eight inches from the beam-to-girder connection to avoid localized stress concentrations that could affect the readings. The offset was towards the north edge of the specimen. Protective coatings were used to account for outdoor exposure and to enhance the bond between the gage and the steel beam. Figure 3-21 shows the gages attached to the girder, and Figure 3-22 shows the exact location of the strain gages on the girder.


Figure 3-21: Strain Gages on Girder

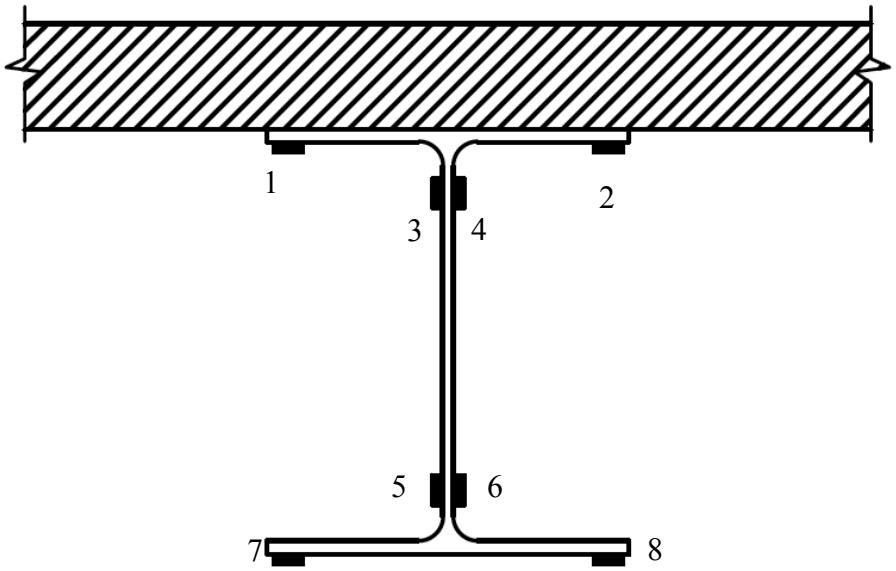


Figure 3-22: Location of Strain Gages on Girder

Four strain gages were placed at each instrumented section of the ring beam to define the strain profile. The specific layout of the ring beam strain gages is shown in Figure 3-23, and the exact location of the strain gages on each ring beam section is shown in Figure 3-24. In total, twenty-eight strain gages were used on the ring beams.

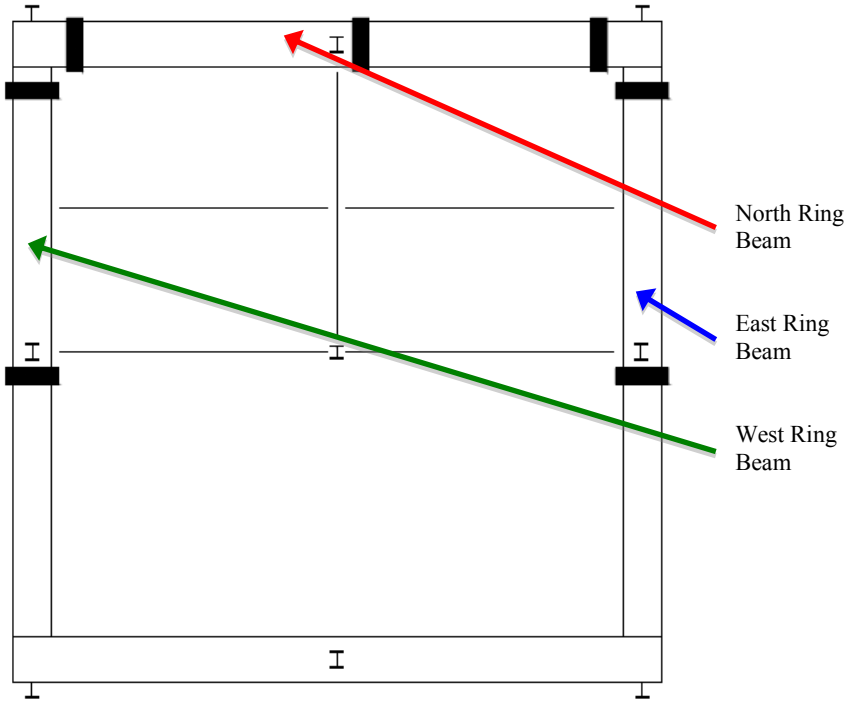


Figure 3-23: Plan View of Ring Beam Strain Gage Locations

Figure 3-24: Section View of Ring Beam Strain Gage Locations

Finally, strain gages were placed on the composite floor system. Gages were placed both on the high and low flutes of the corrugated decking along both the north-to-south and east-to-west directions. These gages were placed on the bottom side of the corrugated metal decking because concrete was cast on top. A detailed layout of the floor deck strain gages is shown in Figure 3-25. In total, twenty-four strain gages were used for the floor decking instrumentation.

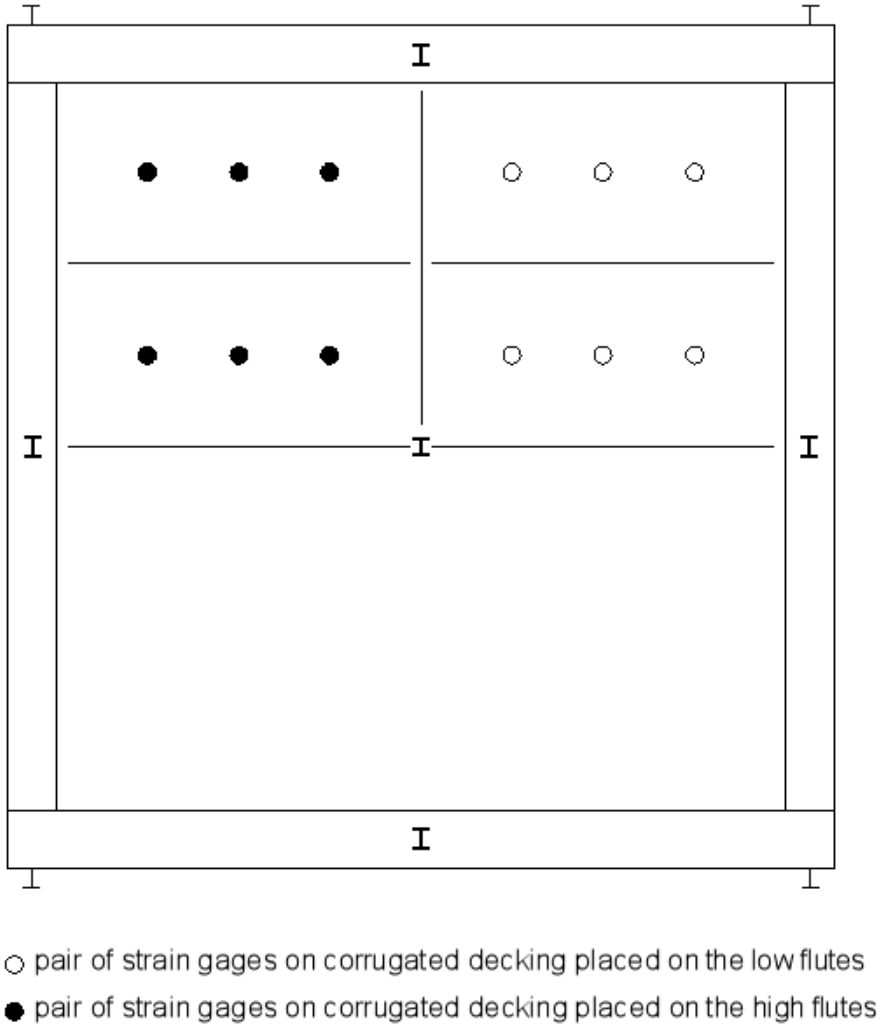


Figure 3-25: Plan View of Floor Decking Locations

This chapter provided a summary of the overall experimental setup and the instrumentation used. The next chapter includes a detailed description of the testing procedure and an analysis of the results based on the data collected.

# CHAPTER 4

# Test Procedure and Results

This chapter provides an overview of the testing procedure used to evaluate the composite floor system described in Chapter 3 under a perimeter column loss scenario. Observations from the test are described, and an in-depth analysis of the results is presented.

## 4.1 TEST PROCEDURE

The perimeter column removal test was performed on May 22, 2013. Before beginning the test, the data acquisition system was activated, and the team members zeroed every single instrument under the specimen dead load. During this procedure, the actuator (perimeter column) was fully engaged. Apart from the specimen's self-weight, each loading pool contained approximately 1550 gallons of water. This volume of water indicates the specimen carried the full UFC load of approximately 115 psf. Before the actuator was engaged, the tare value for the load cell was measured and then input by hand to get the total reaction at the column base.

The lowering of the actuator started at 9:12 am. The actuator was progressively lowered until it was fully disengaged from the test specimen. The actuator was lowered in increments of 0.5 inch. Between the lowering increments, the specimen was left to stabilize and come to equilibrium. The perimeter column was fully disengaged after approximately 41 minutes at 9:54 am (Figure 4-1). The deflection at that point in time was measured to be 5.03 inches. As anticipated, the specimen was able to carry the full progressive collapse design load under static conditions. At that time, the distributed load on the slab was 115 psf, and the line load acting on the edge beam was 320 plf.

Figure 4-2 shows the vertical deflection at the position of the column versus time during the actuator lowering phase. Figure 4-3 shows the column's reaction versus the column's deflection during the same phase.


Figure 4-1: Actuator Fully Disengaged

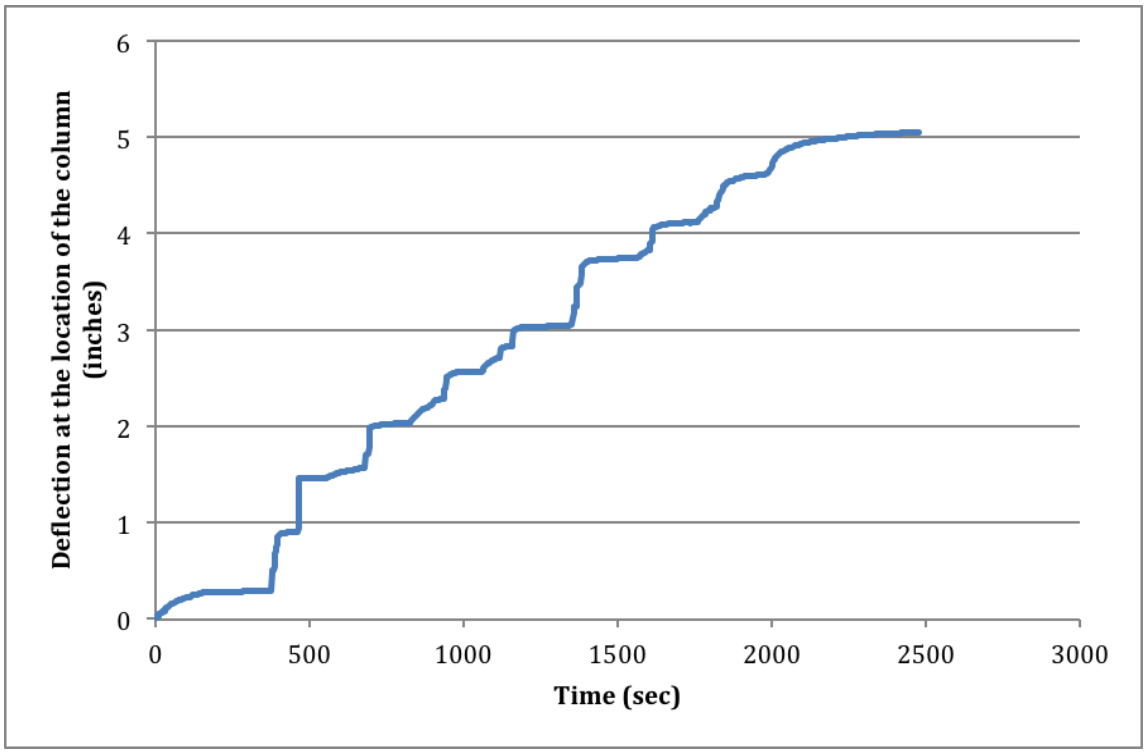


Figure 4-2: Load-Time Curve during Static Column Removal

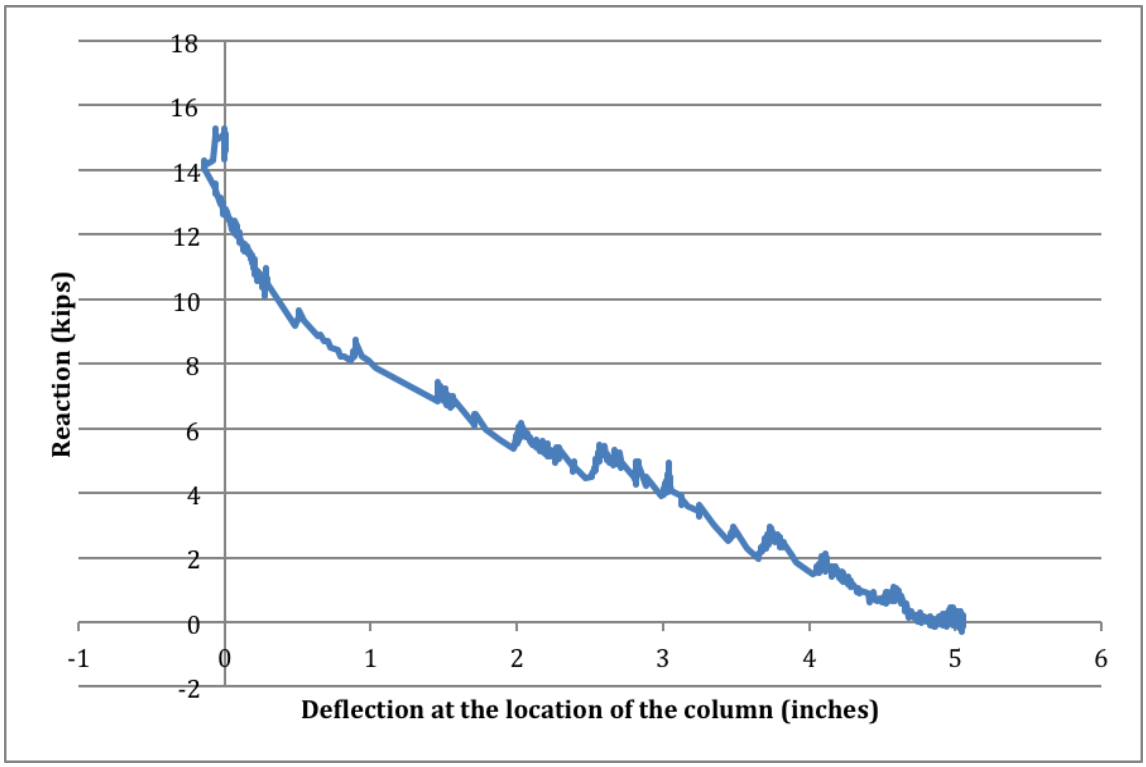


Figure 4-3: Load-Deflection Curve during Static Column Removal

After fully disengaging the actuator, additional load was added to the specimen using the pool-irrigation system described in the previous chapter. Water pumping started at 10:07 am. Similarly to the procedure used to lower the actuator, the research team decided to load the test specimen in increments and allow the slab to stabilize between loading steps. Three minutes after starting this phase of testing, at approximately 10:10 am, the research team heard a loud noise, and the cross bracing seemed to vibrate intensely. The deflection jumped from 5.2 inches to 6.1 inches. As quickly as possible, the team members stopped the water irrigation system. At this time, the west pool contained 15980 gallons of water, and the east contained 15280. After stopping the water pumps, the slab stabilized in its new equilibrium position.

Additional loading started again at 10:16 am and stopped at 10:26 am. The measured deflection was 7.12 inches, and the west and east pool contained 16450 and 15737 gallons of water, respectively. The pumps started again at 10:32 am when the deflection was 7.3 inches. The loading stopped at 10:42 am, and the deflection was 8.25 inches. The west pool contained 16935 gallons of water, and the east pool contained 16290 gallons of water. At 10:52 am, the loading started once again, and the deflection at that time was measured to be 8.65 inches. The loading stopped at 11:02 am, when the deflection was 10.8 inches and the pools contained 17461 and 16700 gallons of water, respectively. The pumps started again at 11:06 am at a deflection of 11.8 inches. At 11:11 am, collapse occurred. At that time, the west poll pool contained 17710 and the east pool contained 16974 gallons of water, resulting in a total load on the slab of approximately 190 psf. Just prior to collapse, the deflection was approximately 13.6 inches. Figure 4-4 shows an overall diagram of the loading sequence versus the vertical displacement at the position of the column. The notation “ON” means that the pumps were active at that point of time, while “OFF” means that they were not pumping water in the pools.

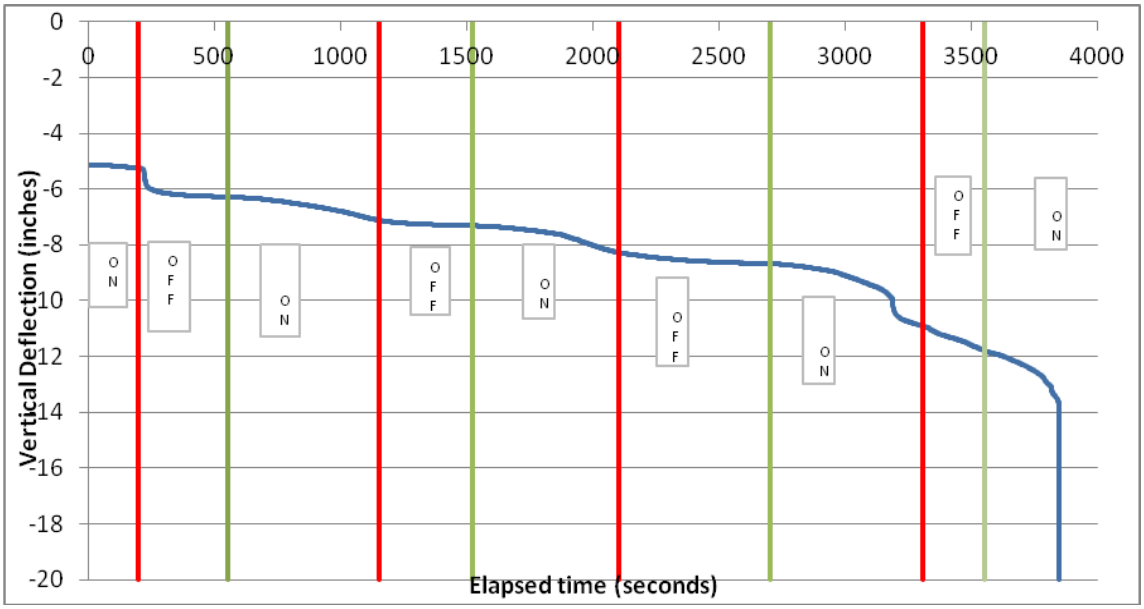


Figure 4-4: Water Loading Stage (Column Deflection versus Time)

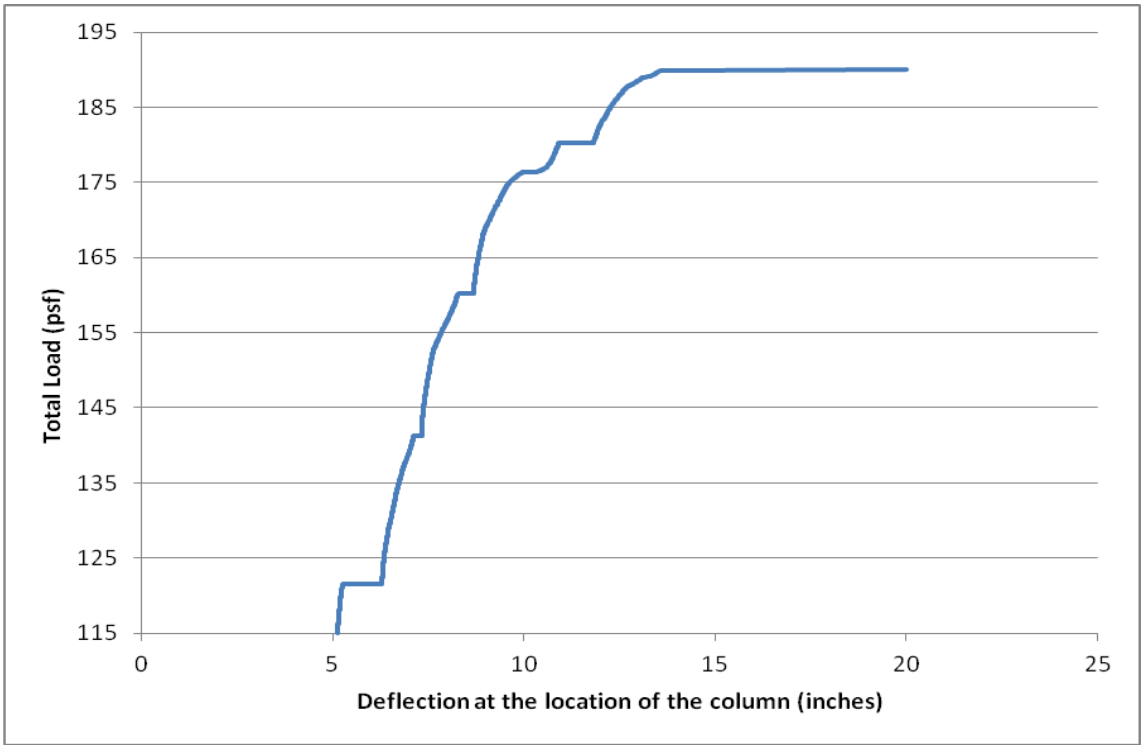


Figure 4-5: Load-Deflection Curve during Water Loading

## 4.2 Experimental Results And Analysis

This section provides a summary of all the data collected during the test. The instrumentation used during the test is described in Chapter 3.

### *4.2.1 Load-Displacement Observations*

In this section, the load-displacement curve for the perimeter column is presented. The column's displacement was measured with four linear potentiometers attached at the base of the column, as mentioned in the previous chapter. The total displacement was calculated by averaging the measurements of the four potentiometers. The superimposed load was calculated by the flow meters on the water pumps, converting the gallons into kips. Although the data show there were small differences in the water volume between the east and west pool, for simplicity it is assumed the load was applied uniformly over the floor system.

Figure 4-3 shows the load-deflection curve during the removal of the perimeter column. The behavior is clearly nonlinear. This can be attributed to possible cracking in the concrete slab or nonlinear response of the steel connections. As mentioned previously, the deflection when the actuator was fully disengaged was 5.03 inches.

Figure 4-5 shows the total load versus deflection curve during the additional loading phase of the test. The horizontal branches on this plot show the regions where the pumps were stopped. Due to the fact that flow meters were used to measure the water supply and that minor leaking occurred compared to a previous test conducted at FSEL where excessive leaking took place (Hull, 2013), the research team believes the additional load measurements are acceptably accurate. In addition, as expected, Figure 4-5 clearly shows the floor system loses stiffness as the load is increased and eventually reaches a horizontal branch where collapse occurs. Specifically, the load-deflection

curve remains fairly linear during the first 40 psf of applied superimposed load. The system starts to soften after 50 psf of superimposed load until it reaches its maximum capacity. Although the peak load and deflection just prior to the onset of collapse are known, the actual failure sequence and response of individual floor system components is not clear. Despite the large amount of data collected and visual observations made during the test, the specific mechanisms controlling the reduction in stiffness and eventual collapse are not precisely known. The test specimen reached its full capacity with no substantial damage or localized failure of any of the monitored components. Taking into account the loud noises that became louder as the load increased, it is speculated that cracking of the concrete slab was the main factor that reduced the test specimen's total stiffness. This hypothesis is further supported by the specimen's deformed shape prior to collapse, where a large deflection occurred at the position of the perimeter column (Figure 4-6). Even though concrete cracking cannot be verified by the pictures or videos of the collapse, it is assumed to have occurred.


Figure 4-6: Deflected Shape when Loud Noise Occurred

From the plot in Figure 4-5, it can be estimated that the deflection due to the additional loading was 162% of the initial deflection corresponding to when the actuator was removed. Figure 4-7 shows the deflection of the column versus the superimposed load during the final phase of the additional loading. Figure 4-8 shows the same deflection as a function of time. This final phase lasted approximately 5 minutes, and the specimen deflected an additional 1.8 inches.

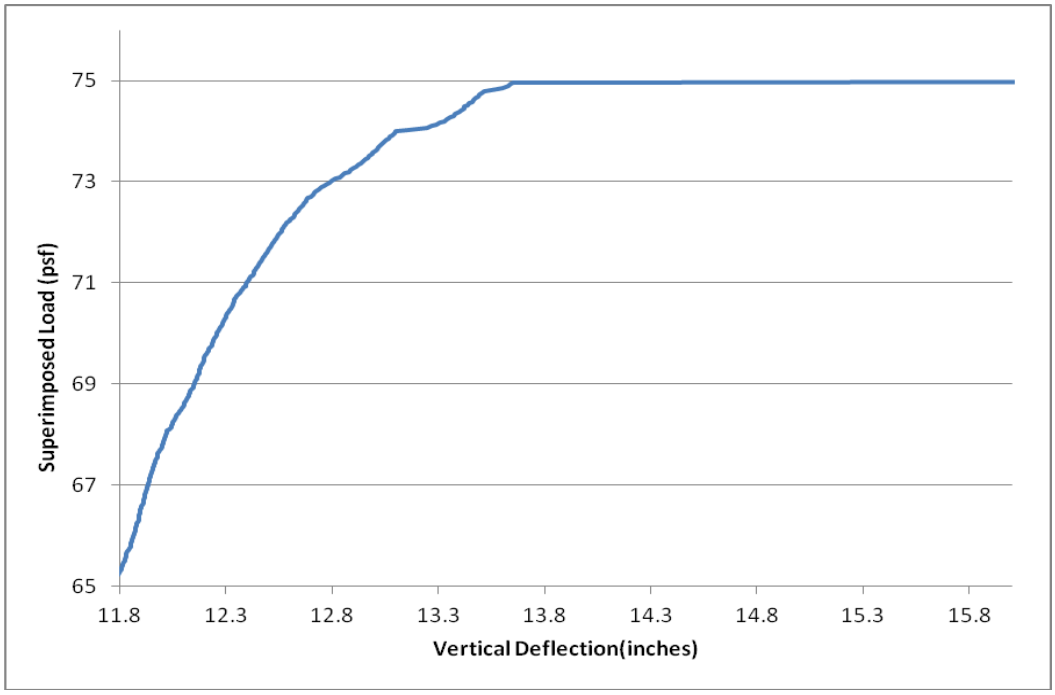


Figure 4-7: Superimposed Load-Deflection Curve before Collapse

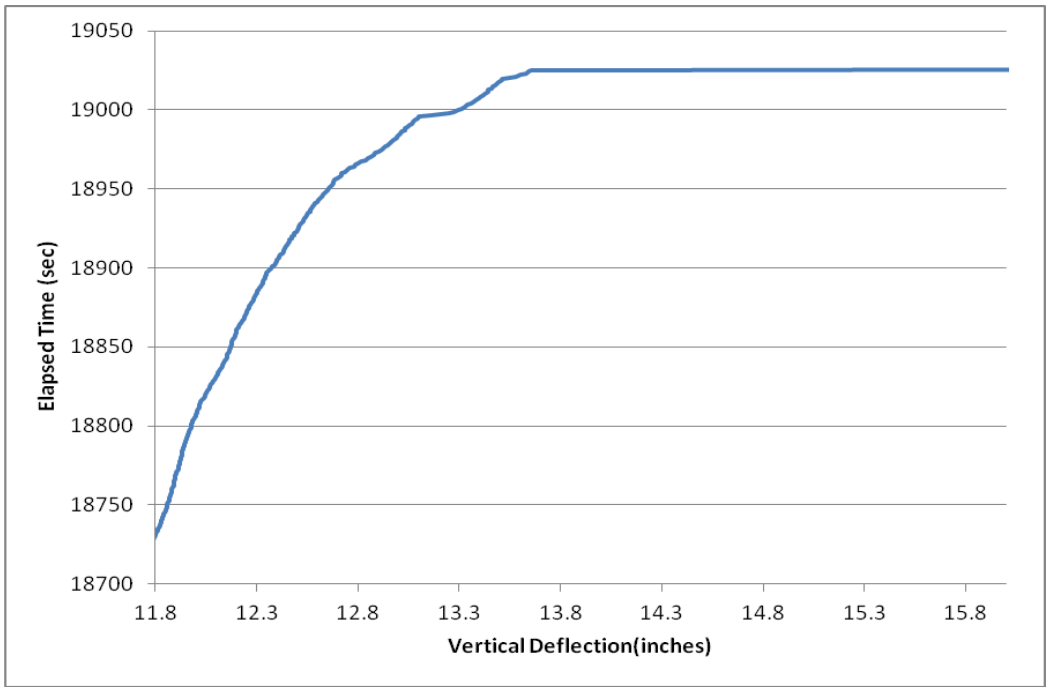


Figure 4-8: Time-Deflection Curve before Collapse

### *4.2.2 Strain Profile In Girder*

To understand the behavior of the main girder during the test, the strain gage measurements at the midspan of the girder are presented and discussed here. The detailed layout of the strain gages on the girder was presented in the previous chapter. As mentioned, the girder was instrumented with eight strain gages in total: two on each flange, two near the top of the web, and two near the bottom of the web. To simplify and average the results, these 8 measurements were normalized to four strain locations over the depth of the cross section. This was done simply by averaging the measurements on either side of the section. As can be seen in Figure 3-22 of the previous chapter, the pairs of strain gages that were averaged together were 1 with 2, 3 with 4, 5 with 6, and 7 with 8. Positive strains correspond to tension.

All strain gages were placed on the girder during the construction of the specimen and before concrete was cast. Although the gages were zeroed at the beginning of the test, it should be noted that they do not measure the absolute values of strain. Rather, they measure a change in strain from the zero position and are used to assess behavior during loading. Figure 4-9 shows the measured strains in the girder during the column removal phase. As can be seen, the maximum strain is approximately $1.7 \times 10^{-4}$. Assuming a Young's modulus of 29,000 ksi, this strain corresponds to a stress of 4.93 ksi, which is well within the elastic range of behavior. The plot also shows the entire section sees negative strains everywhere and the strains get bigger as the load is increased. It also shows the strains become larger moving from the top flange to the bottom flange. These results indicate that during the removal of the perimeter column, the girder did not behave as a catenary member. Instead, it behaved as a flexural member in which the strains varied through the depth of the section. Because these strain values correspond to the change in deformation from the start of the test (i.e., the

pre-existing strains prior to the column unloading phase are not included in the readings) and because these strains correspond to a single section at the midspan, the exact deflected shape along the length of the member and the neutral axis position are not known precisely. Nonetheless, given the negative strain values and variation in strain through the depth of the cross-section, it can be concluded that the beam did not demonstrate catenary response during the column unloading phase. This can be further explained by the fact that the intermediate floor beams might have added some level of support to the main girder at the midspan and therefore the latter behaved more like a cantilever rather than a catenary.

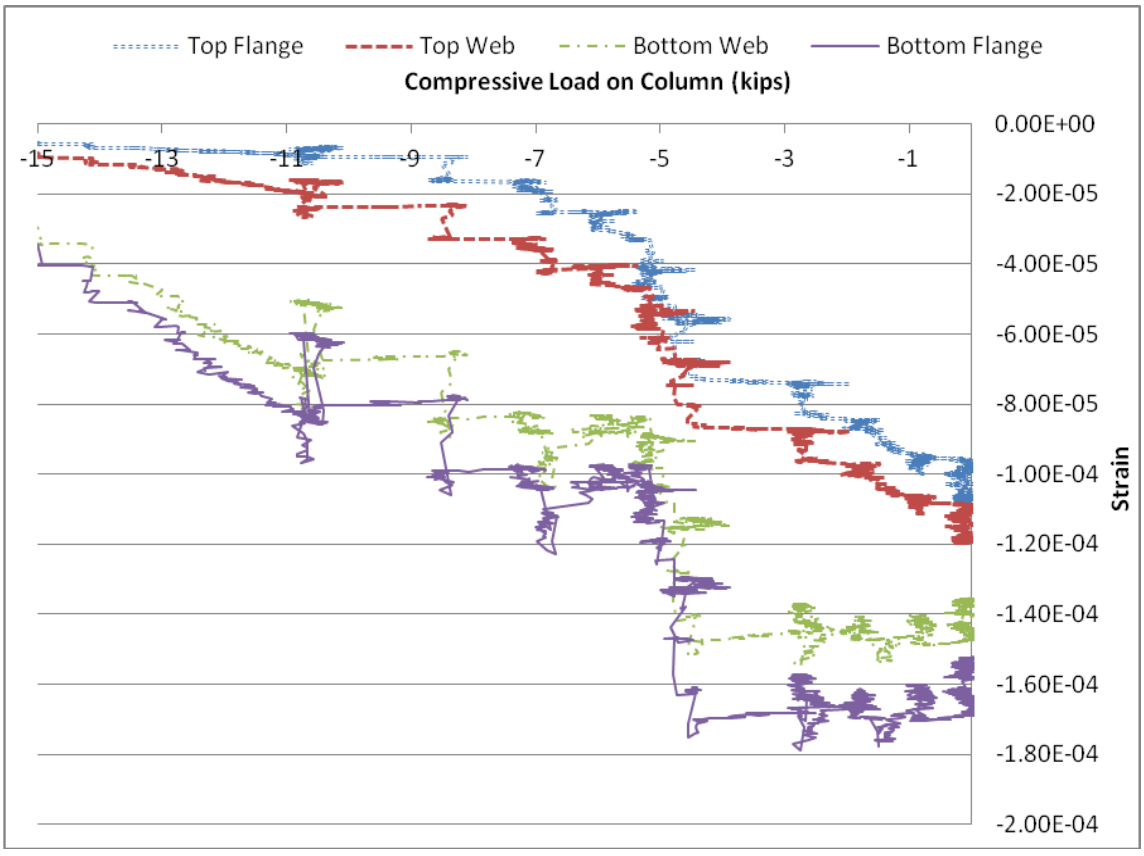


Figure 4-9: Strain in Girder during Column removal

Figure 4-10 shows the measured strains in the girder during the additional loading phase. The plot suggests that the neutral axis moves from the concrete slab to the section's web. The fact that the bottom flange and lower portion of the web are in tension and that the top flange and upper portion of the web are in compression indicates the member is now in positive bending, in contrast with the actuator removal phase. It can also be seen that as the ultimate load is approached, the curves tend to drop to zero, meaning the specimen has started failing and is experiencing rigid body motion rather than developing additional deformation.

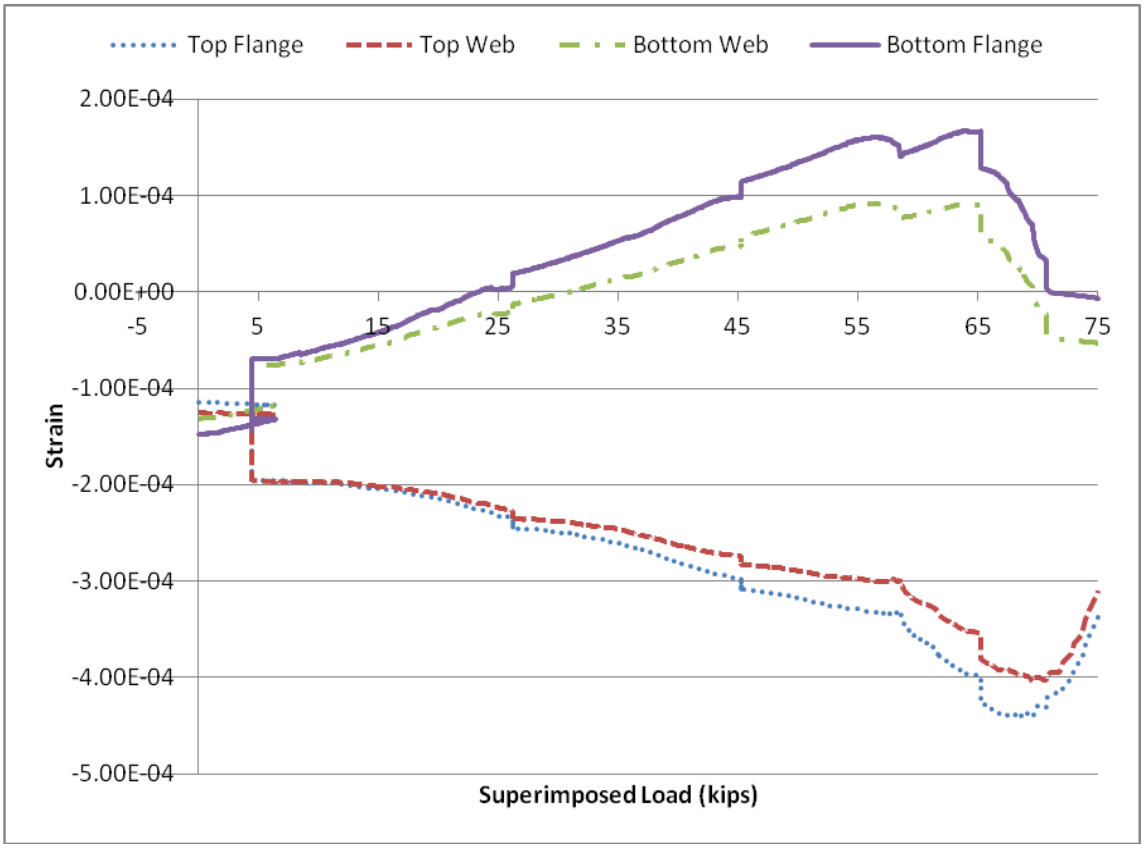


Figure 4-10: Strain in Girder under Superimposed Load

Based on the strain values measured during both the actuator removal phase and the superimposed loading phase, it is estimated that the girder remained in the elastic range and did not reach its yield capacity. Nonetheless, as mentioned earlier, the above mentioned values of strain are not the absolute values; therefore, this conclusion should be treated with caution.

Figure 4-11 depicts the calculated curvature in the girder during the water loading phase. The curvature is defined as $(\varepsilon_b-\varepsilon_t)/h$, where $\varepsilon_b$ is the strain at the bottom fiber of the beam, $\varepsilon_t$ is the strain at the top fiber of the beam, and $h$ is the depth of the beam. As expected, the girder experiences positive curvature.

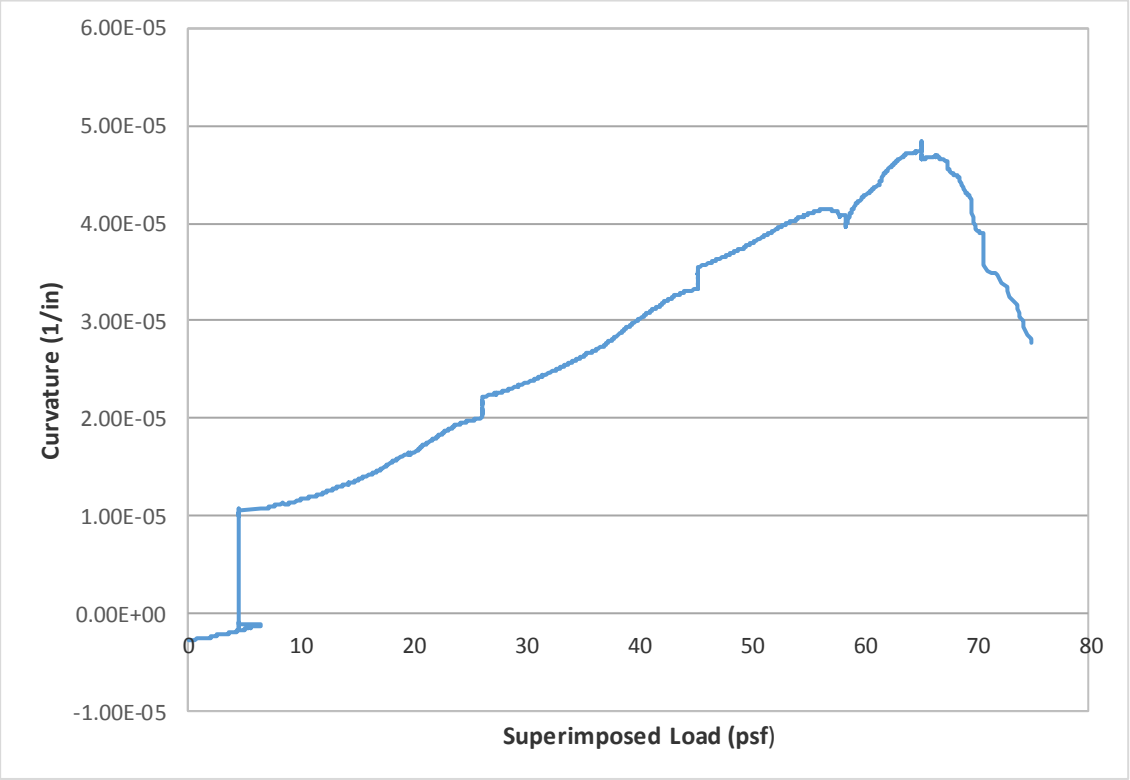


Figure 4-11: Curvature in Girder under Superimposed Load at Midspan

### *4.2.3 Beam And Girder Rotations at Perimeter Column*

The linear potentiometers described in the previous chapter were used to measure the rotation of the main girder and secondary beams at the connection with the perimeter column. To calculate this rotation, the difference between the top and bottom displacement vales was determined, and this value was then divided by the distance between the top and bottom potentiometer. Regarding the beam rotations, the values of the west and east beam were averaged into one value. The chord rotation was also calculated by dividing the total vertical deflection at the position of the perimeter column with the span length of 15 feet. These calculations are based on the assumption that the rotation is sufficiently small.

Figure 4-12 shows the girder and beam rotations as well as the chord rotation during the removal of the actuator. It can indeed be seen that the rotation is small enough for the trigonometric functions not to be used for the above mentioned calculations. It can also be seen that the rotations remain negative throughout this phase of the test. The negative values are reasonable because, as mentioned previously, the girder behaved more like a cantilever than a catenary during this stage of response. The secondary beams responded similarly in that they behaved more like simply supported elements with a shear support at the connection with the main girder rather than a catenary. At approximately -5 kips, there is a sudden increase in the rotation for both the beams and the girder. This value coincides with the sudden increase of the flexural strain as can be seen in Figure 4-9.

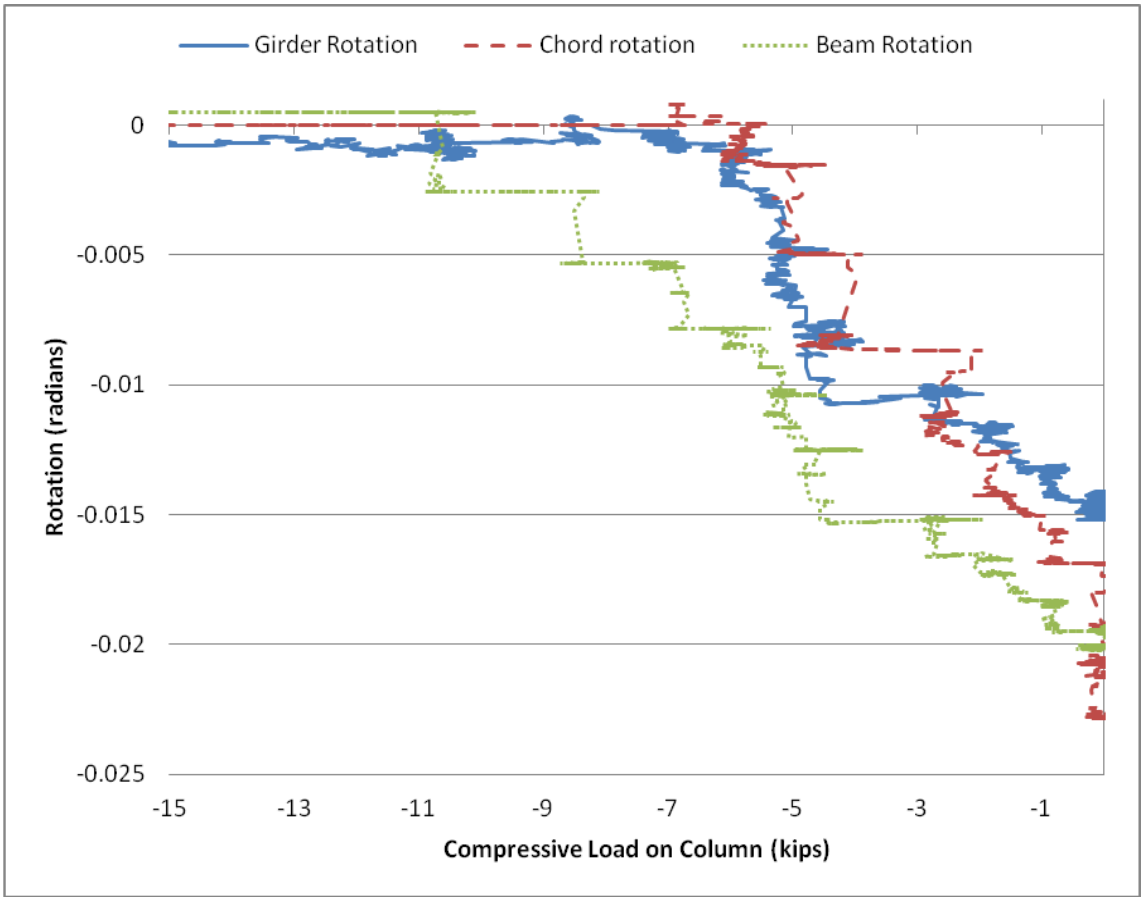


Figure 4-12: Rotation of Beams and Girder during Column Removal

Figure 4-13 shows the change in the girder's and beams' rotation during the water loading stage. The two big spikes in the beam rotation curve are assumed to be "noise" and do not show the actual behavior of the beams. Figure 4-14 shows that both the girder and the beam rotations are smaller than the chord rotation. This result indicates that those elements were potentially behaving as simply supported elements. In addition, the difference between the girder rotation and the chord rotation suggests that the girder was not able to reach a catenary behavior.

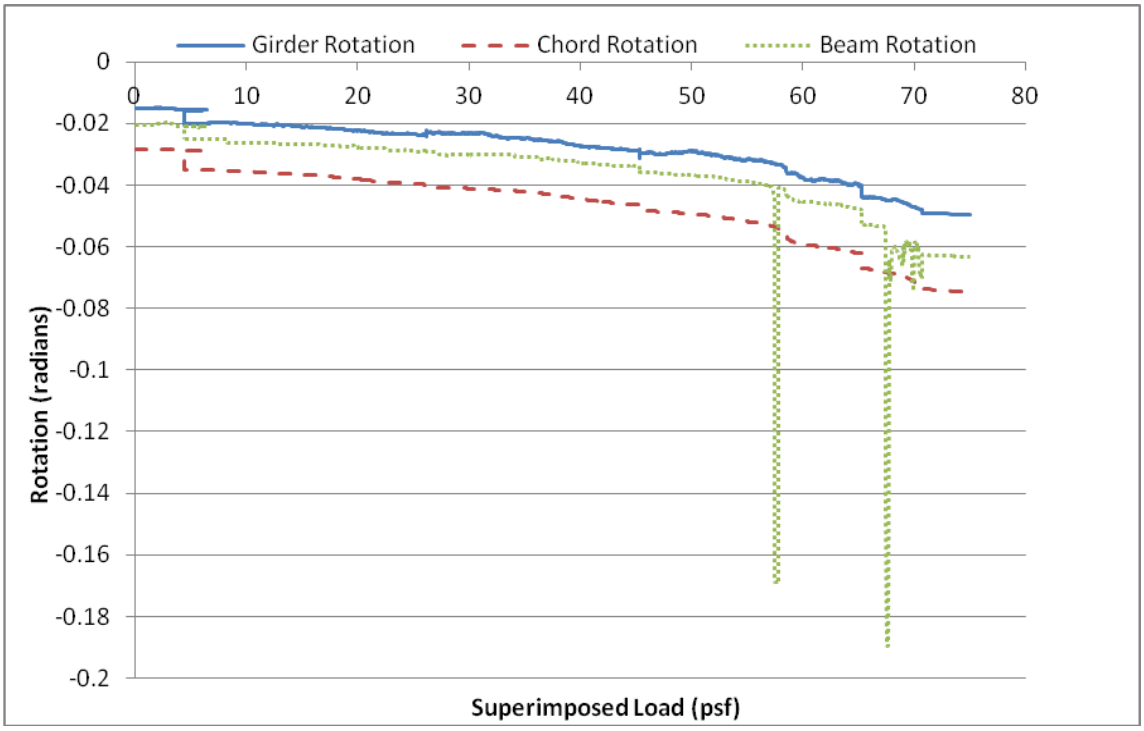


Figure 4-13: Rotation of Beams and Girder under Superimposed Load

### *4.2.4 Restraining Beam Flexure*

The bending moments in the restraining beams were calculated using strain gage data and the formula $M=E\times I\times\varphi$, where $M$ is the bending moment, $E$ is the modulus of elasticity of steel, $I$ is the moment of inertia of the cross-section, and $\varphi$ is the curvature. The exact location of the strain gages was described in Chapter 3, and the procedure for computing curvature from the strain data was described previously in this chapter. To determine the bending response in the vertical direction, the average top and bottom strains were used. To calculate the bending response in the horizontal direction (in the plane of the floor slab), the average strain on the inside and the average strain on the outside were used. Positive moments correspond to tension on the bottom and inside edges of the beams, respectively. In addition, the moment of inertia was calculated by

hand, taking into account the half-inch plates that were welded on the top and bottom of the ring beams.

Figure 4-14 shows the vertical and lateral moments of the west ring beam during the column removal stage. As mentioned in the previous chapter, two points were instrumented on this beam—the south corner and the north corner where the west restraining beam connects with the north restraining beam. As shown in the figure, the lateral moments were much larger than the vertical moments. This suggests that this restraining beam had to resist significant in-plane forces. In addition, the south corner experienced negative lateral moments while the north corner experienced positive lateral moments.

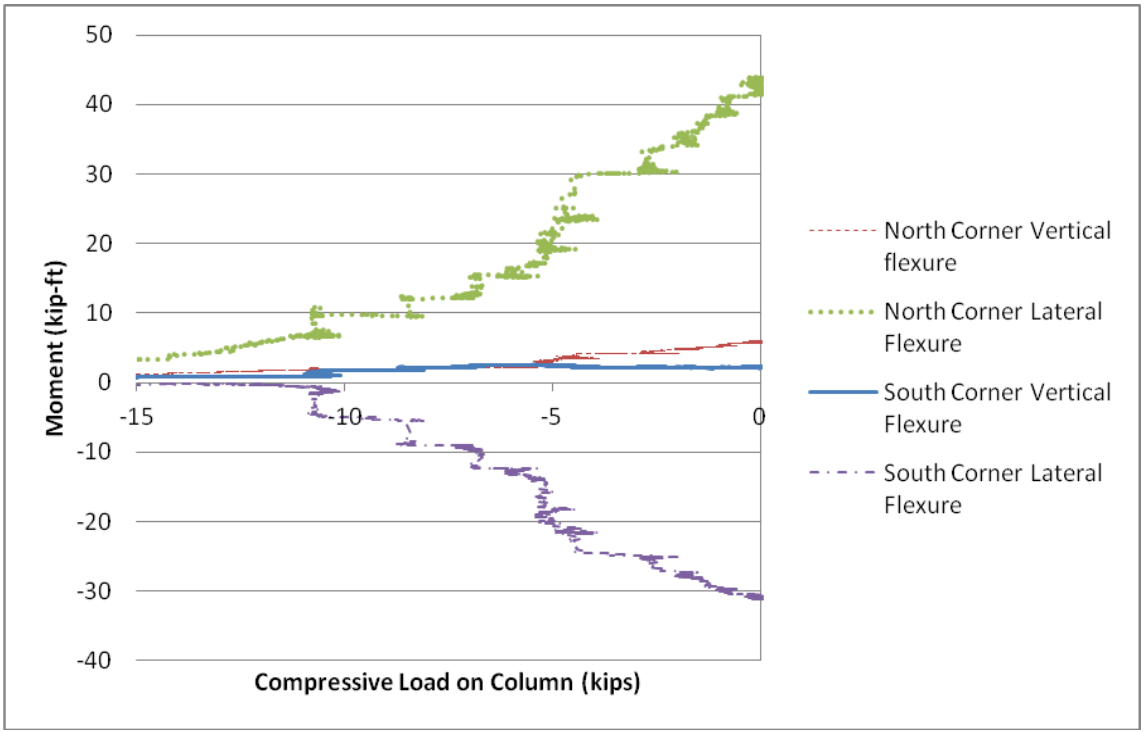


Figure 4-14: Bending Moments in the West Restraining Beam during Column Removal

Figure 4-15 shows the vertical and lateral moments of the east ring beam during the actuator removal phase. The same points as the west ring beam were also instrumented on the east ring beam. As was the case with the west ring beam, the lateral moments were significantly larger than the vertical ones, verifying that the ring beams were primarily loaded in-plane. The south corner experienced negative lateral moments, and the north corner experienced positive lateral moments. Symmetry suggests that the behavior of the west and east restraining beams should have been identical. Although an identical response was not observed, possibly due to the different load in the pools, the two beams have the same trend of moments and values with the same order of magnitude. Both diagrams also show that at a column load of approximately 11 kips, there is a jump in the value of the moments, and the beams start to undergo larger in-plane forces. This possibly suggests that a change in stiffness occurred at this load due to concrete cracking or component failure; however, this hypothesis cannot be confirmed from the test data or from observations and videos of the test.

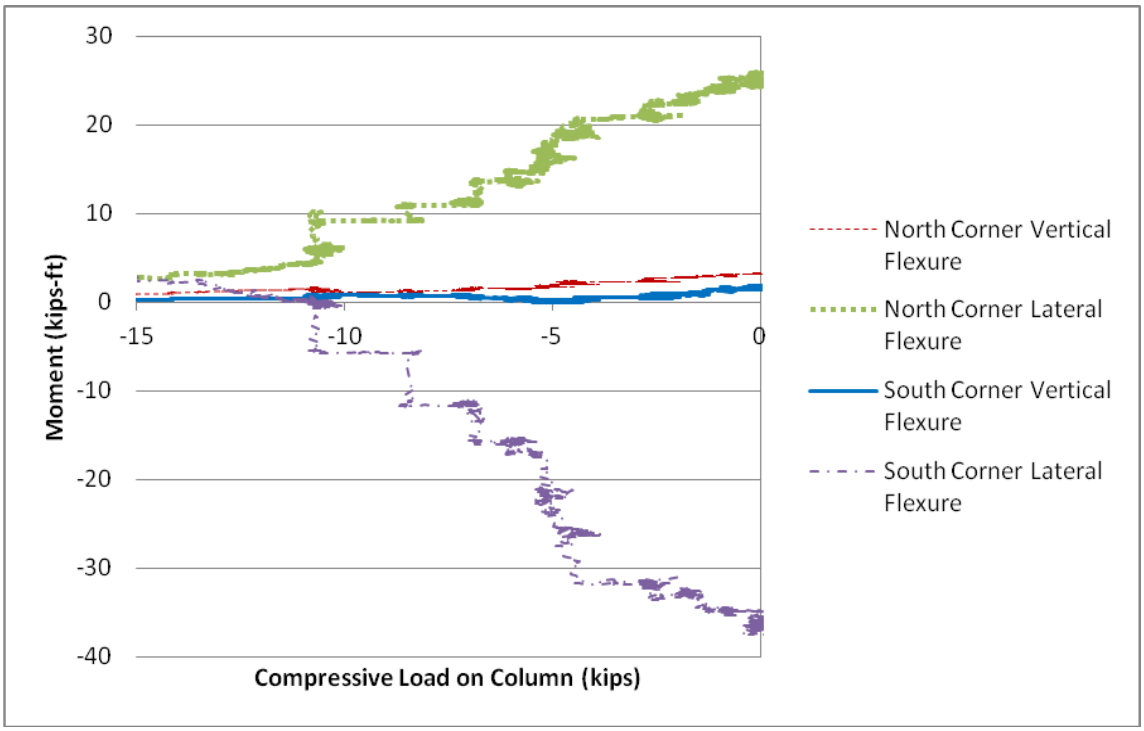


Figure 4-15: Bending Moments in the East Restraining Beam during Column Removal

Figure 4-16 shows the vertical and lateral moments of the north ring beam during the column removal stage. The north beam was instrumented at three points: the west corner (left end), the east corner (right end), and the midpoint. Once again, the lateral demand was much larger than the vertical one. Figure 4-17 also shows the two ends experienced positive lateral bending while the midpoint underwent negative lateral bending. These results agree with those obtained from the west and east ring beams. In addition, good agreement is observed between the behavior of the two ends, though the response is not precisely identical.

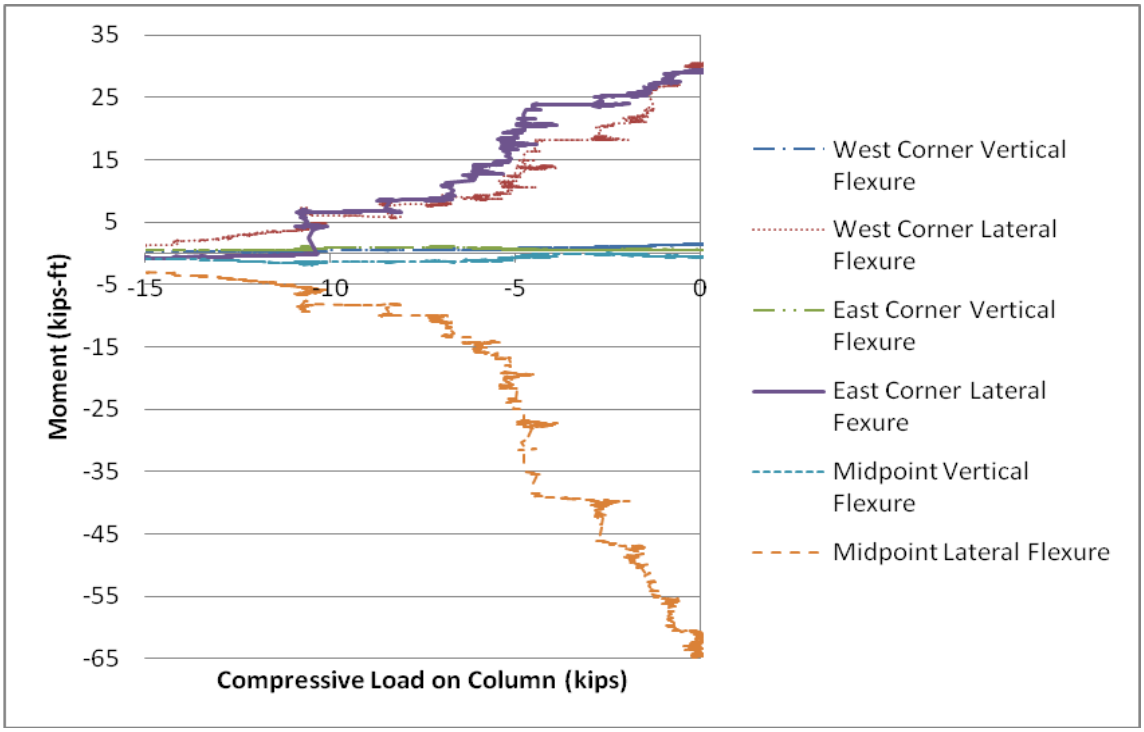


Figure 4-16: Bending Moments in the North Restraining Beam during Column Removal

Figure 4-17 shows the calculated bending moments in the west restraining beam during the superimposed loading until collapse. Figure 4-18 shows the same measurements for the east restraining beam. These figures indicate the moment profile is the same for both beams; however, the west beam experienced significantly larger values of lateral moment at the connection with the north restraining beam compared to the east restraining beam. This result suggests that failure most likely initiated at the west portion of the structure and that the failure was not completely symmetric. Similarly to the column removal stage, the east and west ring beams experienced significant in-plane forces during the superimposed loading as indicated by the large difference between the lateral and vertical bending moments.

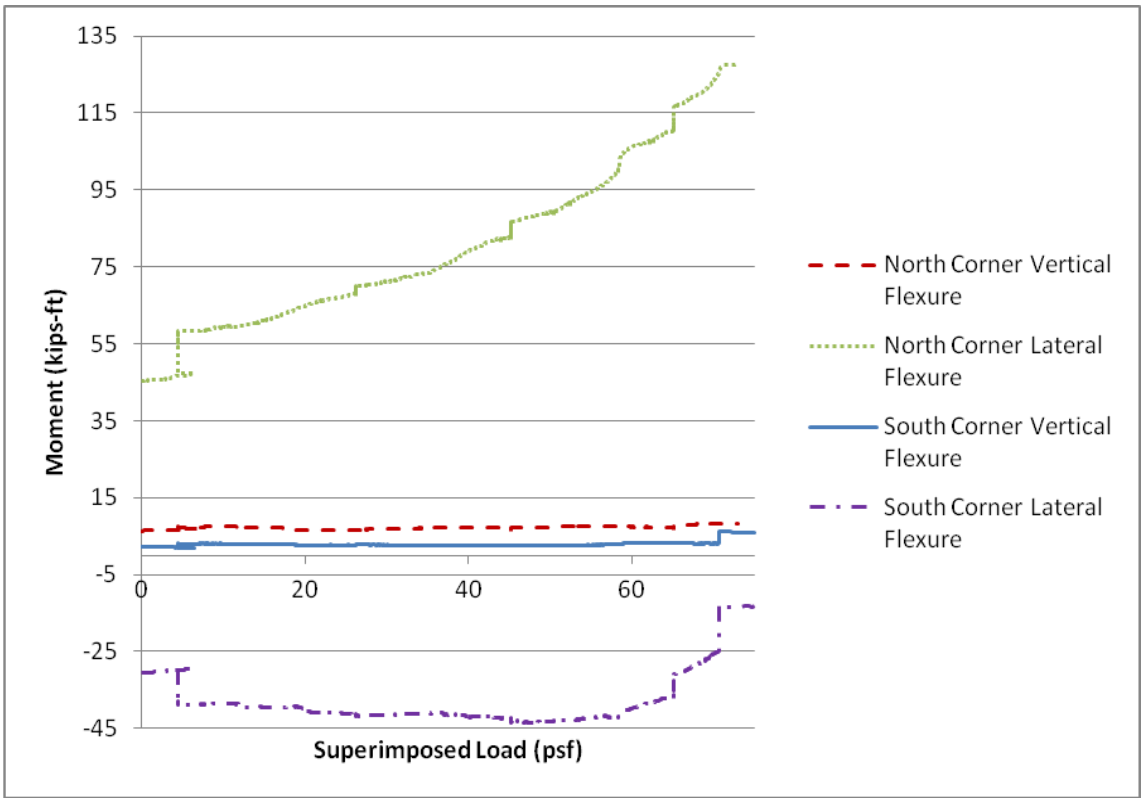


Figure 4-17: Bending Moments in the West Restraining Beam under Sustained Load

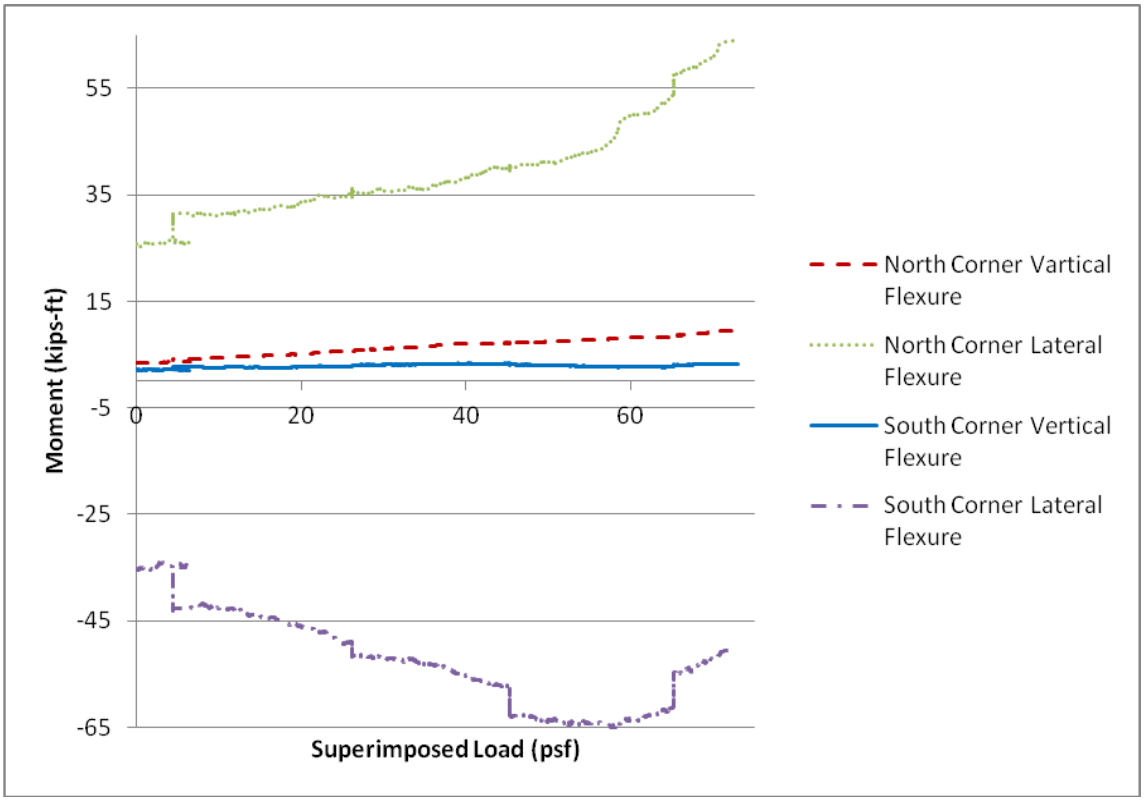


Figure 4-18: Bending Moments in the East Restraining Beam under Sustained Load

Figure 4-19 shows the vertical and lateral bending moments of the north restraining beam during the superimposed loading stage. The graph shows that the west corner moment demand was higher than the east one. This is in agreement with the previous diagrams, suggesting that collapse initiated towards the west side of the structure. Moreover, the large difference between the vertical moment and lateral moment values indicates the development of significant tensile forces along the ribs of the corrugated decking. This possibly suggests that collapse initiated due to failure of the longitudinal seams in the metal decking. It also supports the idea that a significant amount of the specimen's strength comes from the corrugated decking.

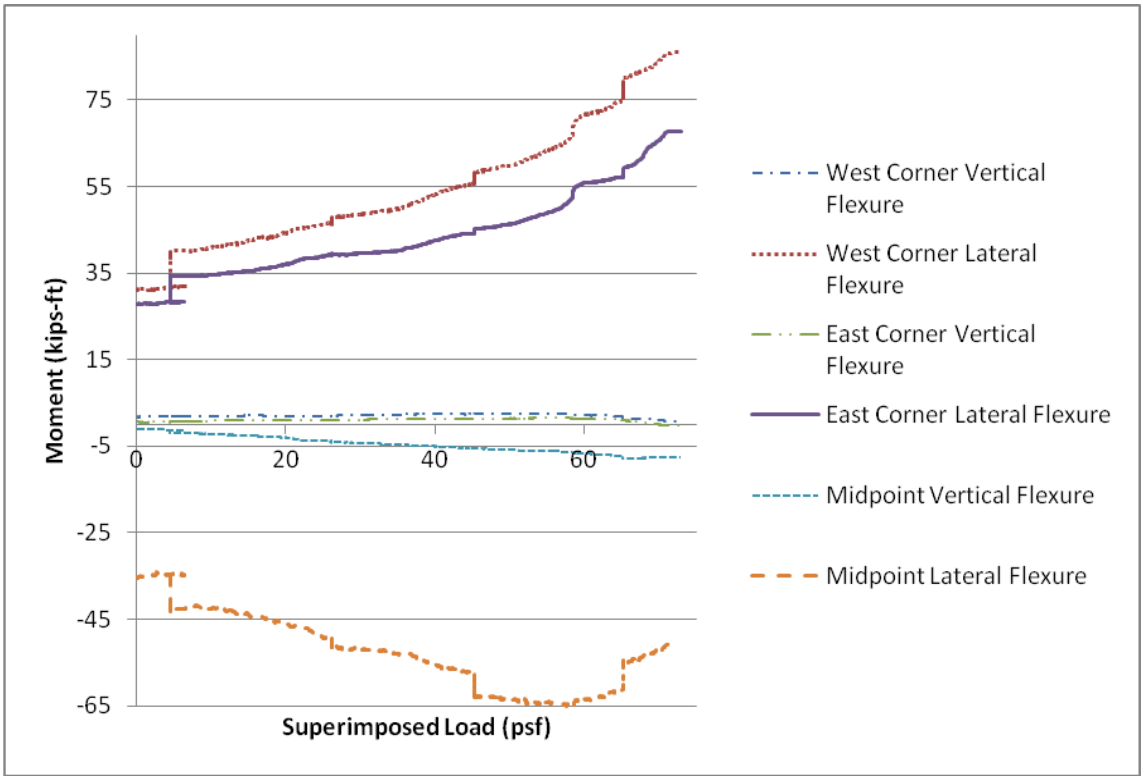


Figure 4-19: Bending Moments in the North Restraining Beam under Sustained Load

### 4.3 Test Specimen After Collapse

Although not clear from the visual observations and measured results, it is speculated that collapse initiated by either the failure of the longitudinal seams in the metal decking or connection failure. In this section, photographs documenting the state of the specimen after collapse are presented.


Figure 4-20: Corrugated Decking and Beams after Collapse

Figure 4-20 shows the secondary beams remained almost undamaged during the collapse, while the floor beams underwent significant damage. It can also be seen that the longitudinal seam of the corrugated decking failed at the position of the side lap, as indicated by the arrow. Because the decking remained attached to the beams, it can be concluded that the shear studs did not tear out at the beams. Figure 4-21 also indicates that the corrugated decking failed at the side lap positions and along its longitudinal

seams. It is unlikely, however, that collapse initiated due to side lap failure. Rather, this was an outcome of the collapse.

Figure 4-21: Corrugated Decking after Collapse

Figures 4-22 through 4-25 depict various connection failures observed after the collapse. However, it is uncertain as to whether these failures were the initiating cause of the collapse or were the result of the floor system failure.


Figure 4-22: Girder-Restraining Beam Connection Failure

Figure 4-23: Perimeter Column-Perimeter Beam Connection Failure

Figure 4-24: Restraining Beam-Floor Beam Connection Failure

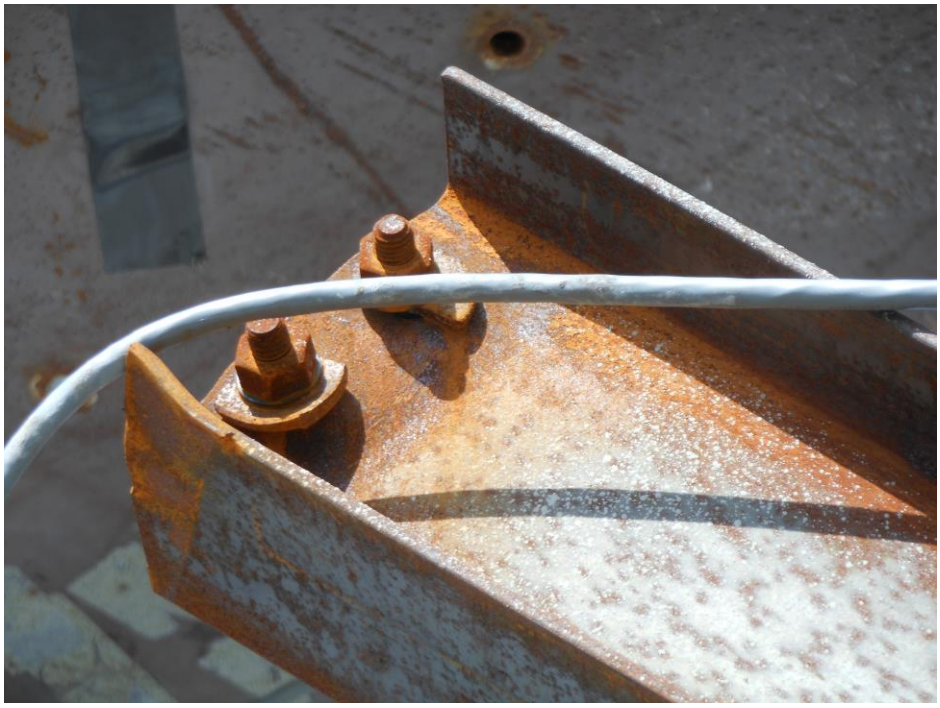

Figure 4-25: Floor Beam Connection Failure

Figures 4-26 and 4-27 indicate the behavior of the shear studs was not the same everywhere. Figure 4-26 shows that the studs did not tear out from the decking, while Figure 4-27 shows that the studs tore out from the decking but remained attached to the steel beam.

Figure 4-26: Shear Studs Remaining Attached on the Corrugated Decking


Figure 4-27: Shear Studs Tearing Out from the Corrugated Decking

In the next chapter, computational work related to modeling the response of a composite floor system is presented. Following that chapter, detailed conclusions and recommendations for future work are provided in Chapter 6.

# CHAPTER 5

## Pull-Out Analysis

As mentioned in previous chapters, many researchers performing high-fidelity progressive collapse analyses use the nonlinear finite element software LS-DYNA. This software is capable of producing accurate models for highly dynamic loadings such as those associated with progressive collapse. One key aspect for properly simulating composite floor systems under progressive collapse is modeling the interaction between the steel beams and the concrete slab through the shear connectors. Although literature exists on the modeling of composite behavior with popular commercial software such as ANSYS and ABAQUS (Chapter 2), no references that study the capability of LS-DYNA to accurately simulate and capture composite behavior have been found. In addition, most research teams that utilize LS-DYNA for progressive collapse analyses use simplified models rather than full three-dimensional models. This approach is used to reduce computational demands, which can be extremely large for nonlinear dynamic analyses. Before analyzing a full-scale model of the test specimen, the research team decided that both three-dimensional and simplified models that focus on composite action should be studied to identify possible deficiencies. The team members decided that the so-called pull-out test is a good measure of composite action because, in most cases, the main mode of failure is the pull-out of the beam and shear connectors from a concrete slab. This particular test was briefly described in Chapter 2 and will be described in more detail later in this chapter.

## 5.1 MATERIAL TESTING

Before starting work on the actual pull-out analyses, material models for different components had to be identified. It was decided that structural steel can be readily modeled as an elastic-perfectly-plastic material based on its well understood response prior to strain hardening. Neglecting strain hardening is a somewhat conservative approach that simplifies the analysis and has been shown to provide acceptable accuracy in problems similar to the one being considered in this study. Unlike steel, concrete materials show pressure dependency and are brittle in tension, requiring a more complicated constitutive model than steel to capture these effects. Therefore, there was a desire to ensure that the concrete material model selected from LS-DYNA's material library was a model that could accurately simulate a normal-weight concrete's behavior. To test this behavior, analyses of three simple tests were conducted: 1.) a concrete cylinder compression test, 2.) a concrete cylinder tension test, and 3.) a modulus of rupture test. Moreover, after reviewing the available literature (LSTC, 2007), it was found that two material models are primarily used for modeling concrete: "072R3-CONCRETE_DAMAGE_REL3" and "159-CSM_CONCRETE". Accordingly, the three above mentioned tests were analyzed with each of the two material models to observe how well they are able to accurately predict response.

### *5.1.1 Concrete Cylinder Compression Test*

A typical 6-inches in diameter by 12-inches tall concrete cylinder was analyzed in direct compression. All the geometry and input was created with LS-PrePost (LSTC, 2007). Initially, a cylinder was created as can be seen in Figure 5-1.

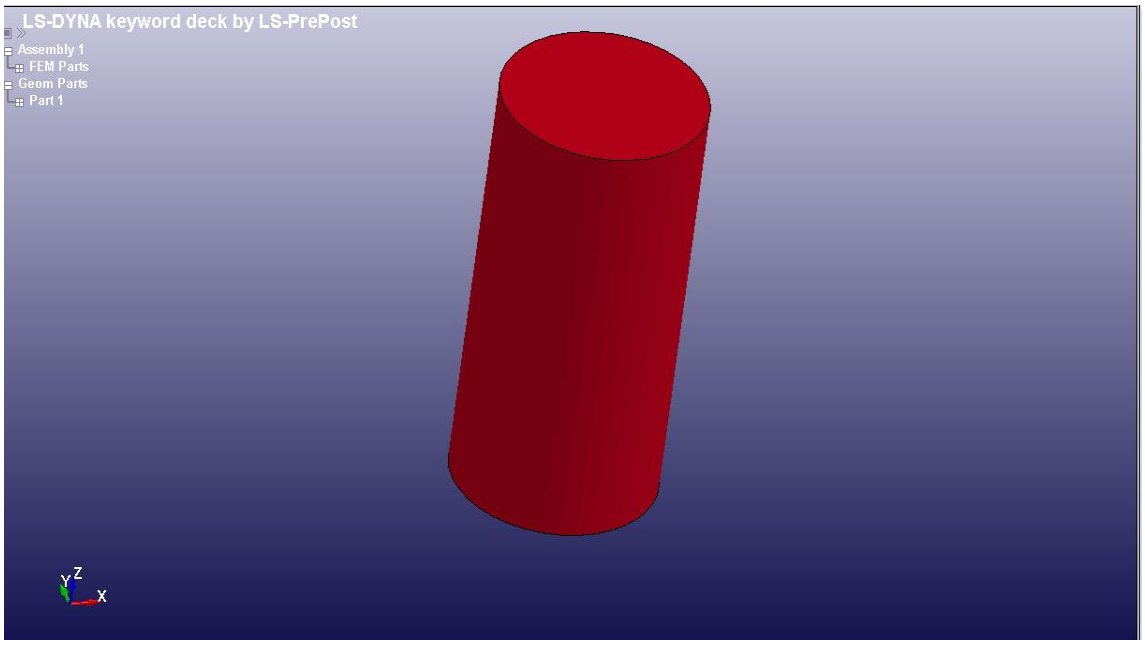


Figure 5-1: Cylinder Created with LS-PrePost

Then, the geometry was discretized with full integration solid elements (Element formulation #3). For comparison purposes, two different meshes were created—one with an average element size of 0.5 inch (dense) and one with an average element size of 1 inch (coarse). The discretized geometry of both the dense and coarse mesh can be seen in Figures 5-2 and 5-3, respectively.

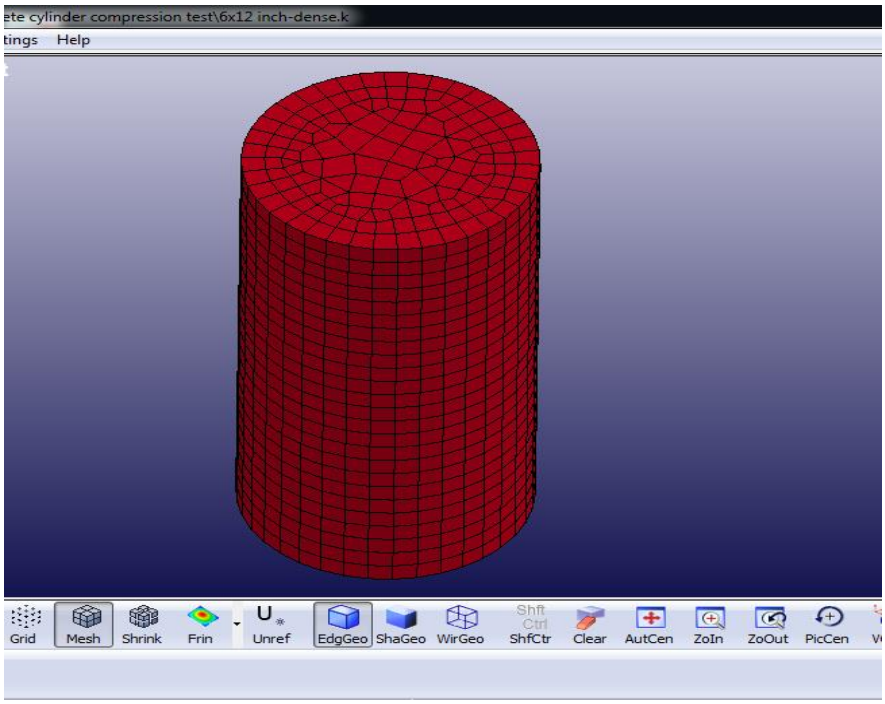


Figure 5-2: Dense Mesh

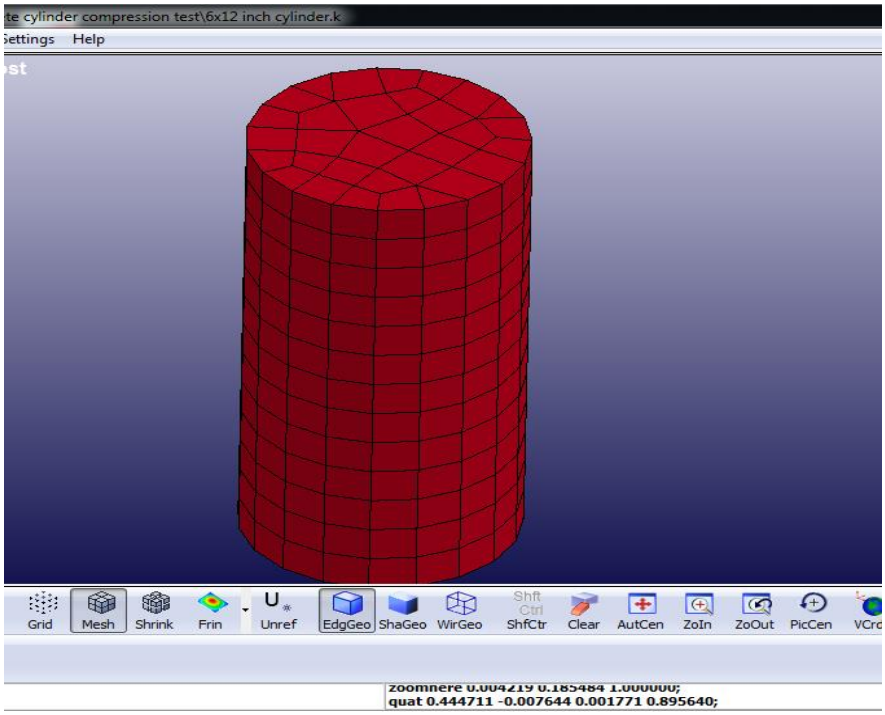


Figure 5-3: Coarse Mesh

The specimen was fixed on the bottom surface in the longitudinal direction. Along the other two axes, only a few nodes were restrained. These boundary conditions allow for lateral deformations associated with Poisson's effects and avoid overly constraining the deformation (Figure 5-4).

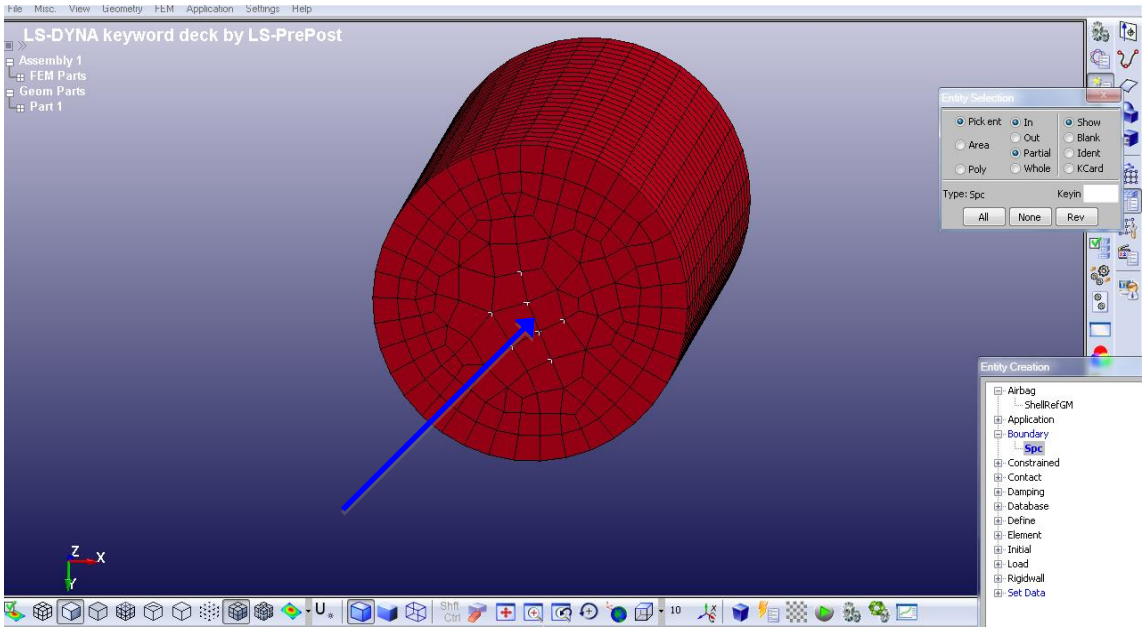


Figure 5-4: Bottom surface nodes restrained along the *x* and *y* axis

The corresponding nodes of the top surface were also restrained along the *x*- and *y*-axis to ensure the specimen will deform along its longitudinal axis and not out of plane.

For the application of the load, a displacement control test was performed. In particular, a displacement value was assigned to all the nodes of the top surface in a direction that caused the cylinder to be in pure compression. An explicit dynamic analysis was performed, and the displacement varied from 0 to 0.1 inch applied over a duration of 1 sec. This loading rate is highly dynamic compared to the pseudo-static

tests routinely done on concrete cylinders and attempted to replicate progressive collapse loading rates.

A typical value of concrete strength equal to 7250 psi (50 MPa) was chosen, and the mass density was specified to be $2.33\times10^{-4}$ lbf-sec$^2$/inch$^4$. The erosion option was enabled so that when a solid element reached its maximum strength, it was automatically deleted from the model. A Poisson's ratio of 0.2 was used.

After solving for the response of the model, the variation in the vertical reaction at the bottom of the concrete cylinder was determined as a function of time. This profile for both the dense and the coarse mesh, and for the two material models, can be seen in Figure 5-5.

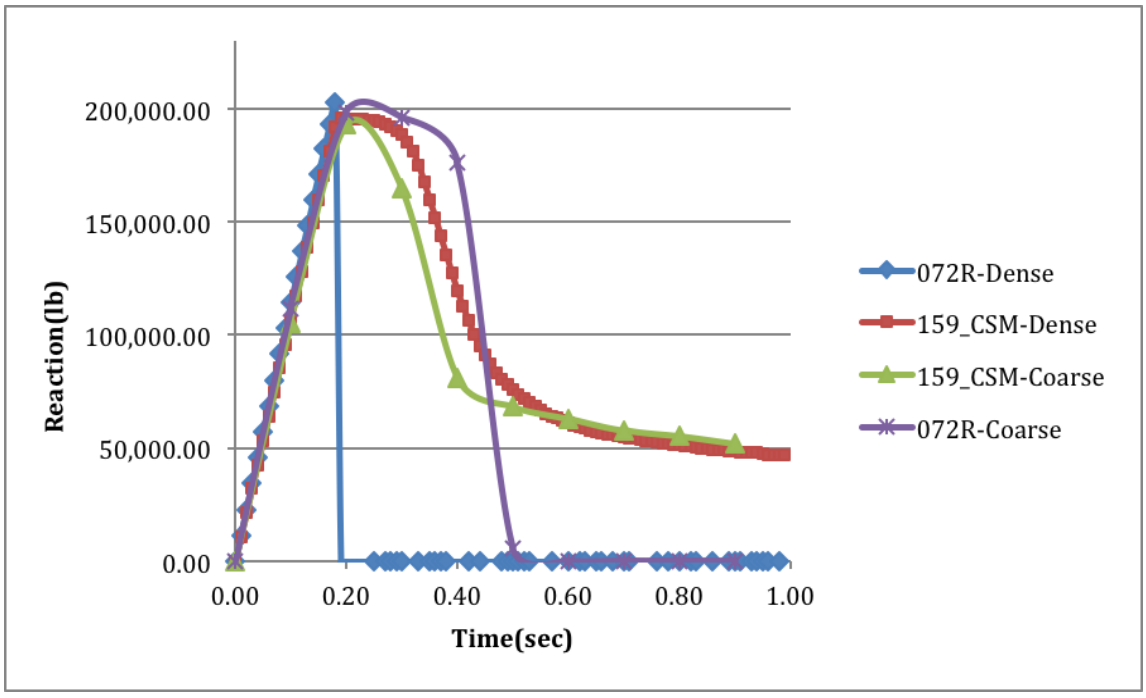


Figure 5-5: Vertical Reaction versus Time for the Compression Test

Based on hand calculations, the total vertical reaction at the base when the concrete reaches failure should be $7250\times\pi\times3^2$=205000 lbs. From the graph, it can be seen that even though an elevated loading rate was used, the strength is consistent with the above mentioned static value, indicating rate of loading effects are not significant. It can also be seen that both material models and mesh densities capture the peak reaction well, but material model 072R is slightly closer to the desired value. However, after the peak reaction is reached, the unloading branch is unrealistically abrupt for the 072R model while it is much smoother for the 159-CSM model. Therefore, it was concluded that the overall response of the 159-CSM material is closest to the desired behavior as far as the concrete in compression is concerned. As for the mesh densities, a small deviation is observed between the dense and coarse mesh for the 159-CSM material. As such, the need to further reduce the element size to improve accuracy was ruled out.

### *5.1.2 Concrete Cylinder Tension Test*

The exact same cylinder with the same properties was used to perform a cylinder tension test. The only difference was that the vertical displacements on the top surface were assigned in the opposite direction to cause the specimen to be in pure tension.

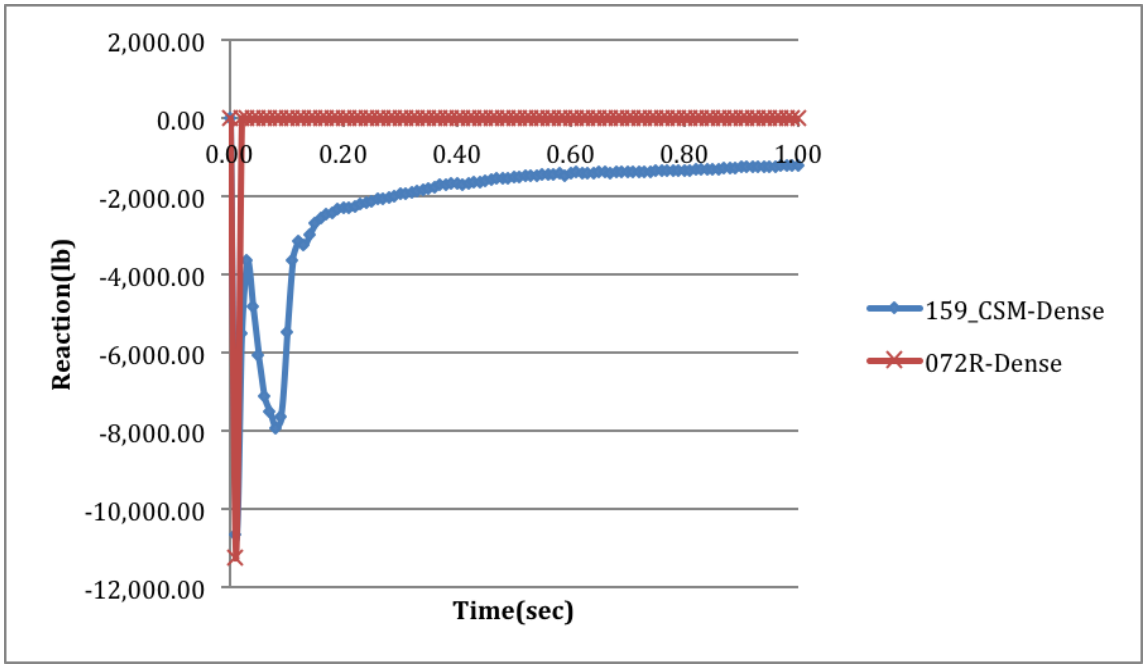


Figure 5-6: Vertical Reaction versus Time for the Tension Test

For simplicity, only the dense mesh configuration was used for the tension test. According to ACI 318-11 (ACI, 2011), the strength of concrete in pure tension is given by the formula $4\times(f'_c)^{0.5}$=340.6 psi, where $f'_c$ is the concrete compressive strength, which is equal to 7250 psi for this case. The peak reaction at the base when the cylinder fails in tension should be $340.6\times\pi\times3^2$=9630 lbs. Based on the plot shown in Figure 5-6, the peak reaction from LS-DYNA is 11000 lbs. This value corresponds to a stress of 390 psi, which is approximately $4.6\times(f'_c)^{0.5}$. Given the brittle nature of concrete and the use of the code-based equation to predict its capacity, the small difference between the computed and predicted strength values is considered to be acceptable. Therefore, it can be concluded that both material models are able to capture the response of the concrete in pure tension. As was the case with the compression test, however, the 072R material model was not able to capture the post-peak behavior accurately and failed abruptly. Conversely, material 159-CSM demonstrated a post-peak jump in the strength. This

aspect of the response was considered unimportant, however, because the strength in tension is not critical to the final response of the pull-out test. Once again, it was concluded that material 159-CSM is more suitable for the purposes of a pull-out analysis.

### *5.1.3 Modulus of Rupture Test*

The modulus of rupture test is another method used to measure concrete strength in tension, and more specifically its flexural strength. The typical test setup for a modulus of rupture test is a simply supported beam with square cross-section. The dimensions of the section are 1/6th the length. The beam is tested under flexure with two point loads applied at $L/3$ from the edges, where $L$ is the length of the beam. The typical setup is shown in Figure 5-7.

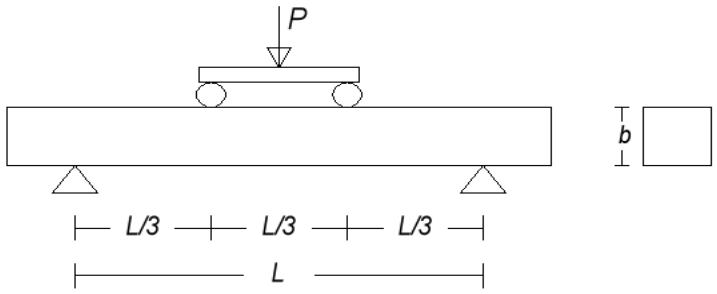


Figure 5-7: Typical Modulus of Rupture Test Setup (ASTM, 1994)

This test setup setup was modeled with LS-PrePost and analyzed with LS-DYNA. Initially, the beam's geometry was created as shown in Figure 5-8. According to the specifications described above, the dimensions of the beam were 6-inches by 6-inches by 36-inches.

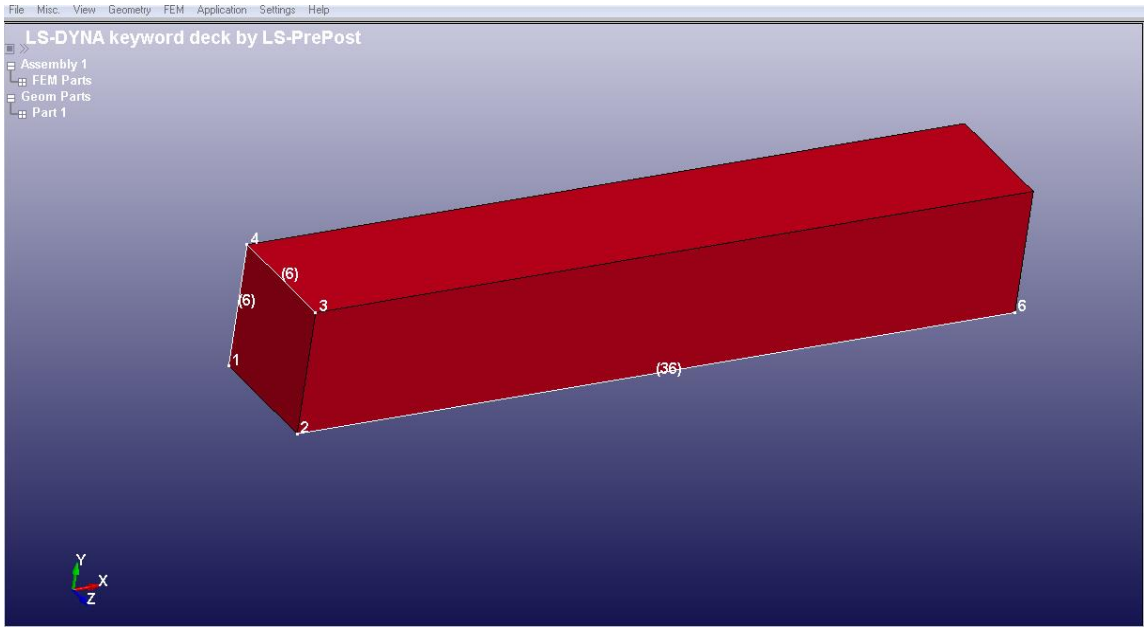


Figure 5-8: Beam Geometry Created with LS-PrePost

The geometry was then discretized with solid elements. For comparison purposes, three different mesh formulations were used: 1.) fully integrated solid elements with an average element size of 0.5 inch (El.formulation 3), 2.) reduced integration solid elements with an average element size of 0.5 inch (El.formulation 1), and 3.) reduced integration solid elements with an average element size of 0.1 inch (El.formulation 1-Dense mesh). Because material 159-CSM behaved better than material 072R in both the direct compression and direct tension analyses, only 159-CSM was used for the modulus of rupture test analyses. Different models would be sought only if the results were unsatisfactory. All specified material properties were the same as for the cylinder compression and tension tests.

As for the boundary conditions, as mentioned above, the beam was simply supported. Therefore, the nodes shown in Figure 5-9 were restrained from moving along

the vertical *z* direction. In addition, one node on each side of these supports was restrained from moving in all directions to ensure that out-of -plane movement would not take place.

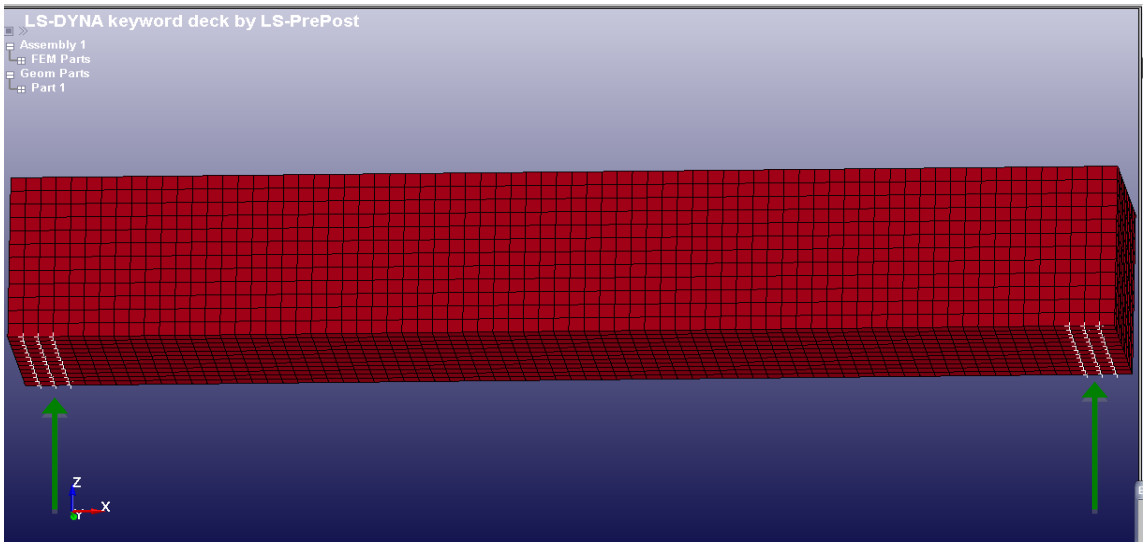


Figure 5-9: Boundary Conditions

The load was applied through a displacement control test. The required nodes around the third-points of the beam were chosen to form a region where prescribed displacements were assigned along the vertical *z*-axis, as shown in Figure 5-10.

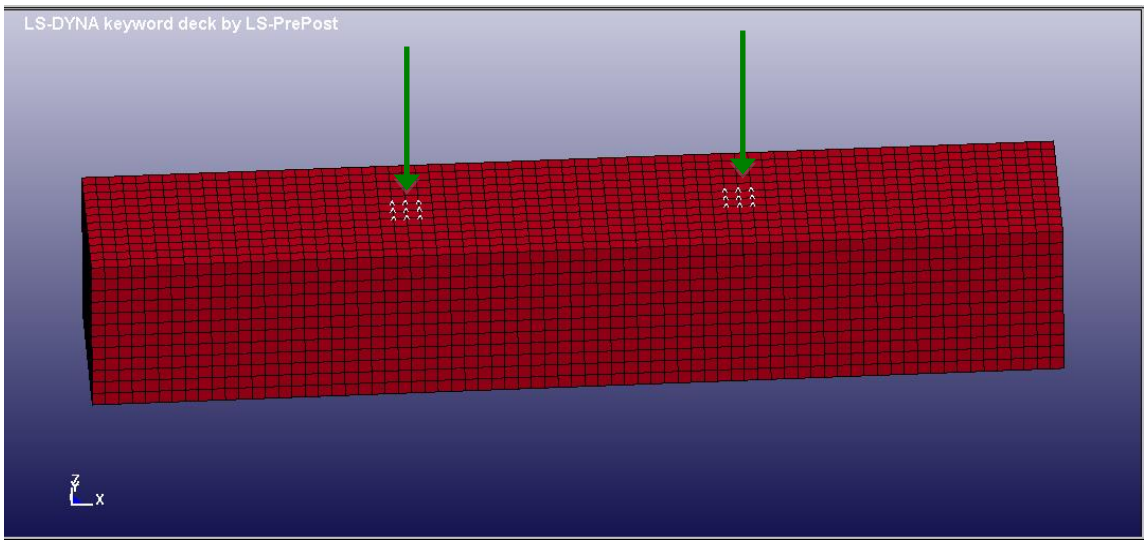


Figure 5-10: Regions of Prescribed Displacements

The value of the assigned displacement varied from 0 to 0.1 inch over a duration of 1 second. An explicit dynamic analysis was performed. Again, this loading rate attempted to accommodate the conditions of a progressive collapse scenario.

After solving for the response of the model, the variation in time of the summation of the vertical reactions was obtained. This profile can be seen in Figure 5-11. Based on ACI 318-11 (ACI, 2011), the theoretical limit for a modulus of rupture test is $7.5\times(f'_c)^{0.5}$=638.6 psi. From the formula $\sigma=M\times y/I$, where $I$ is the beam moment of inertia and $y$ is the distance from the extreme fiber to the neutral axis, the maximum moment $M$ is calculated to be 22,989.6 lbs-in. The relationship between the maximum moment $M$ and the two point loads $P$ is $M=P\times L/3$. Therefore, $P$=1916 lbs, meaning that the total vertical reaction at failure should be $2\times P$=3832 lbs. This limit value can also be seen in Figure 5-11 for comparison with the analysis results. As was the case with the previous test, it can be concluded that rate of loading effects are unimportant.

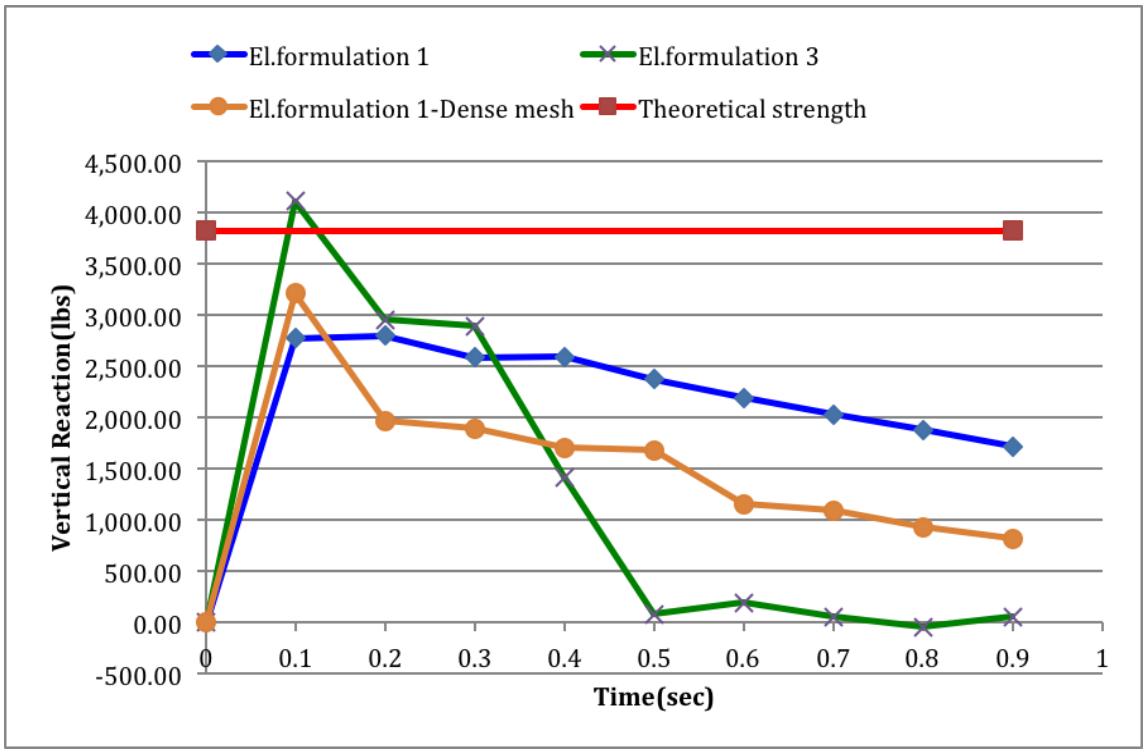


Figure 5-11: Vertical Reaction versus Time for Modulus of Rupture Test

The significant changes in slope observed in the above graph are due to the output points that were specified every 0.1 sec. From the graph, it can be seen that the fully-integrated solid elements give satisfactory results. Accordingly, for the pull-out analyses, material model 159-CSM and fully-integrated solid elements were used.

## 5.2 Pull-Out Analysis

In this section, different simulation techniques for modeling pull-out test are described, validated against experimental data, and compared. Initially, a brief description of the test setup is given and then the models used for analysis are summarized.

### *5.2.1 Test Setup*

A pull-out specimen is usually formed from a short steel beam connected to two small concrete slabs with shear connectors, as shown in Figure 5-12 (Lam, 2005). The slabs rest on the reaction floor, and the load is applied at the upper end of the steel beam. Only one shear stud is connected to each flange. The main parameters of interest are the strength of the shear connector and the slip between the concrete slabs and the beam. This information is used to develop a load-slip curve. The exact dimensions of the specimen adopted for the current thesis are shown in Figure 5-12. The steel beam is a W10×49, and the dimensions of the concrete slab are 619-mm long by 469-mm wide by 150-mm deep. The shank diameter of the shear connector is 19 mm, and the height is 100 mm. The minimum amount of slab reinforcement is used (10 mm bars). This specimen is similar to the standard CP 117 (BSI, 1965) and is the one used in the study by Lam (2005) described in Chapter 2 of the current thesis. The analysis results are validated against that study as will be described subsequently in more detail.

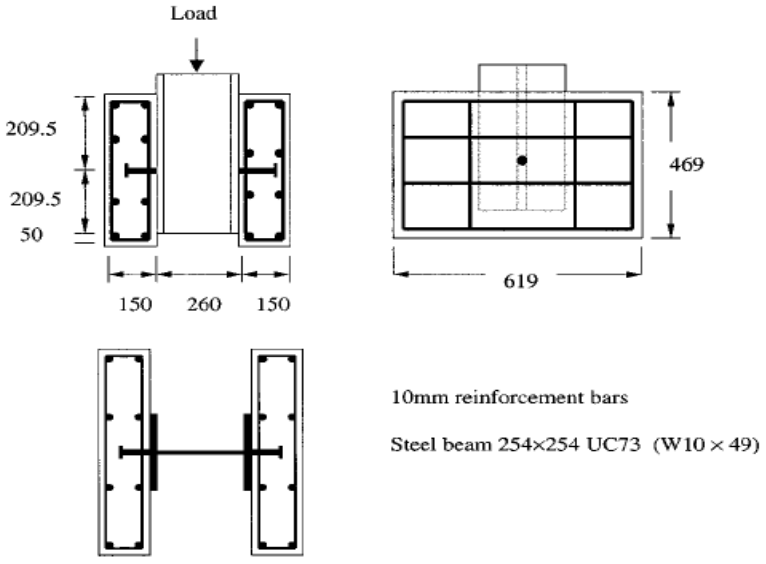


Figure 5-12: Details of Test Specimen (Lam, 2005)

### *5.2.2 Model 1*

The first model created and analyzed was a detailed three-dimensional model of the pull-out specimen, identical to the one analyzed by Lam (2005). The initial geometry was created using Autocad (Kurland, 2004). It was then imported as an IGES file into LS-PrePost. Because the specimen was doubly symmetric, only one-fourth of the model was created and analyzed. Figure 5-13 shows the geometry imported into LS-PrePost. The different colors depict different parts that were combined to form the final model. Figure 5-14 also shows the geometry of the specimen without the slab for clarity purposes regarding the location of the shear stud.

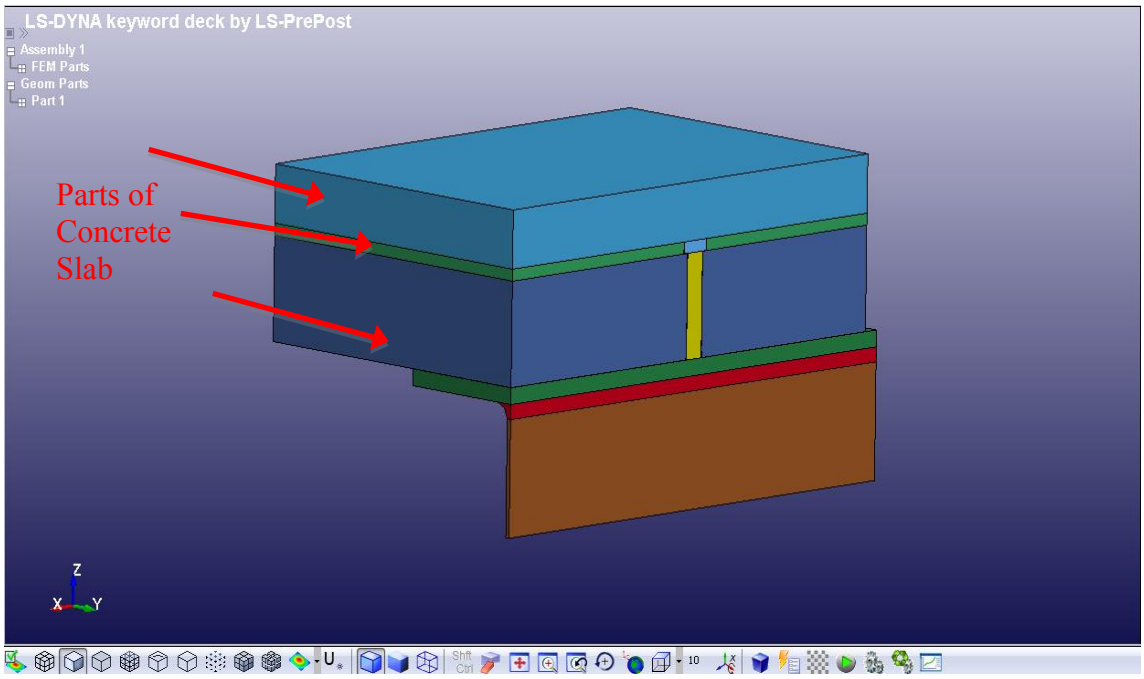


Figure 5-13: Imported Geometry

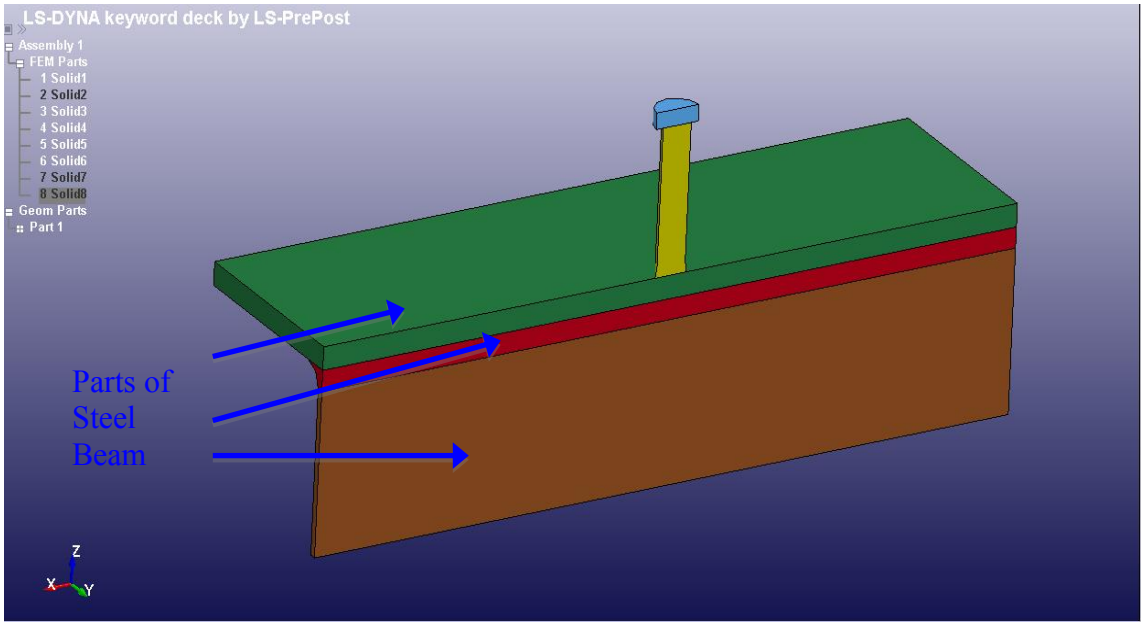


Figure 5-14: Imported Geometry (Slab not shown for clarity)

One of the most challenging issues was modeling the shear stud inside the concrete. To accomplish this task, a hole was created in the concrete slab at the location of the stud so the stud could fit exactly inside the hole. Because of the complicated geometry, it was anticipated that the meshing algorithm would encounter problems. Therefore the geometry was divided into separate parts, as can be seen in Figure 5-13. In particular, the concrete slab was divided into three layers: one layer containing the shank of the stud, one layer containing the head of the stud, and one layer extending from the top of the stud to the top of the concrete slab (red arrows in Figure 5-13). The shear stud was divided similarly—one part that contained the shank and one part that contained the head. The steel beam was also divided into three parts so the meshing procedure could be consistent. One part contained the flange of the beam, one part contained the web, and one part contained the intermediate region between the flange and the web (blue arrows in Figure 5-14).

After the geometry was finalized, the mesh was generated. The automatic solid mesher tool was used, and the average element size was initially chosen to be 5 mm.

After conducting several preliminary analyses and studying the results among models with different element sizes, it was concluded that this particular element size was too small and caused significant delays in the solution time. Therefore, a new average element size that could produce satisfactory results was sought, and the value of 12 mm was eventually chosen. In Figures 5-15 through 5-18, the discretized geometry is shown.

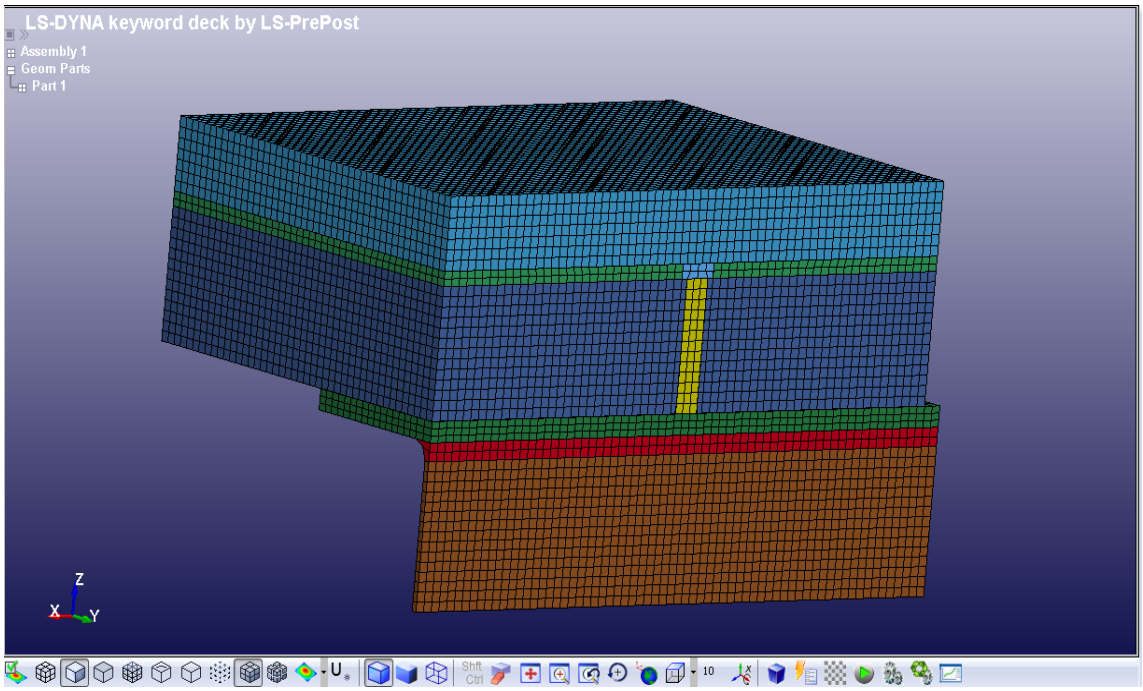


Figure 5-15: Discretized Geometry of the Entire Model

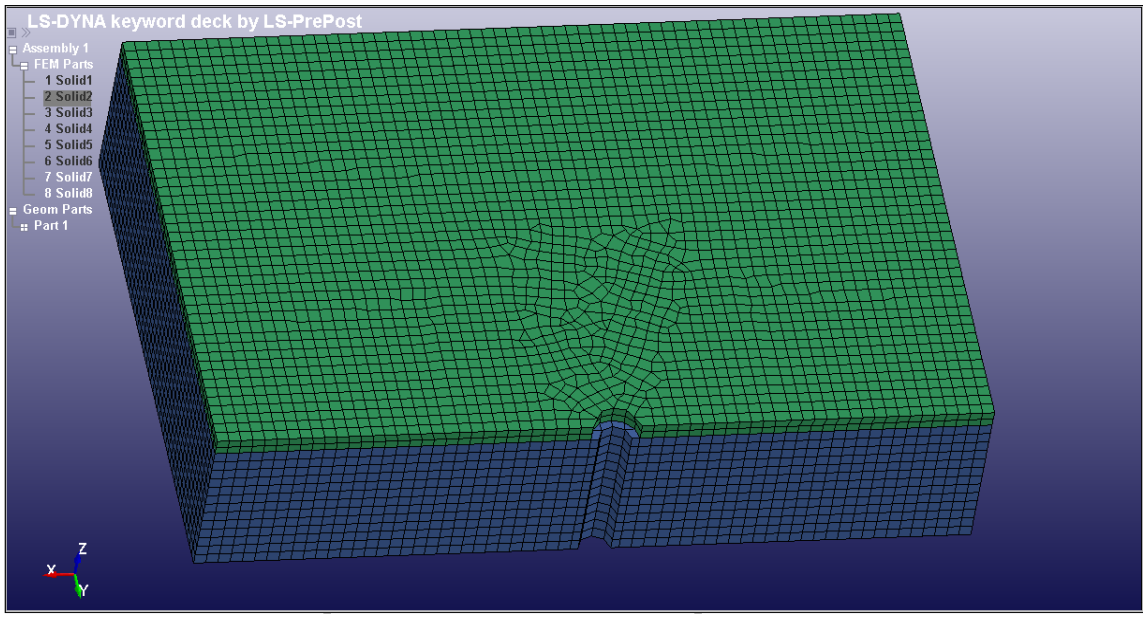


Figure 5-16: Discretized Geometry of the Bottom and Middle Layer of the Concrete Slab

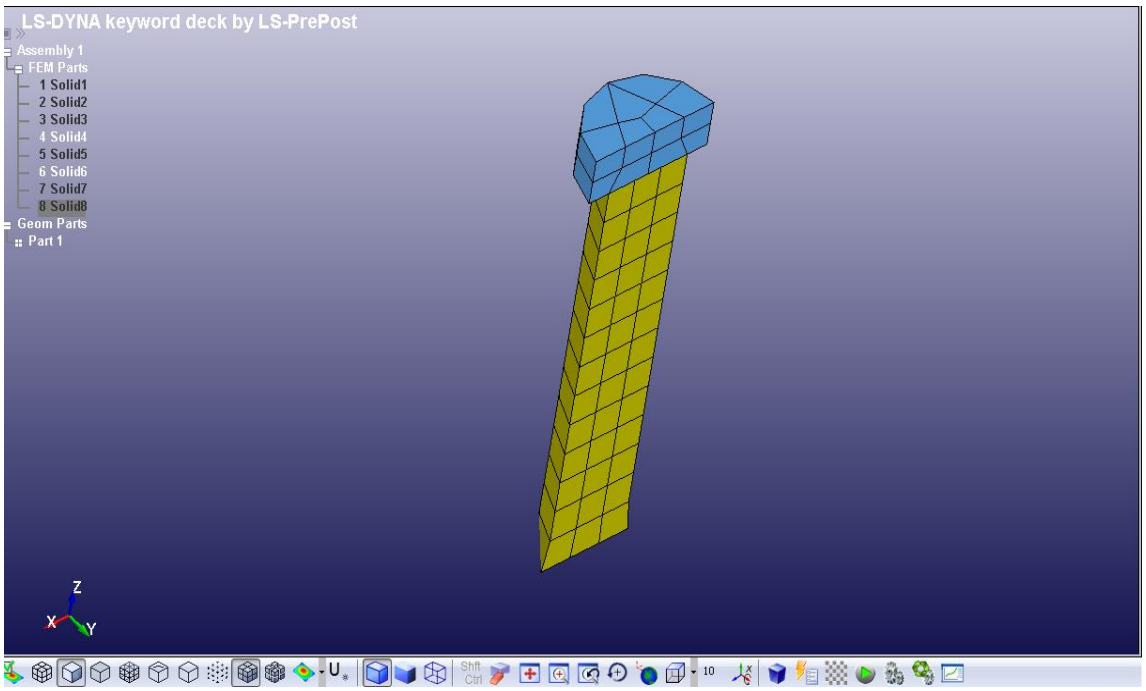


Figure 5-17: Discretized Geometry of the Shear Stud

Another challenging issue was the definition of contact between the parts of the specimen. Specifically, contact was required between the stud and the concrete slab, the stud and the steel beam, as well as the beam and the concrete slab. Because in reality the studs are welded to the beams, a bonded connection between the stud and the beam is an accurate representation of the expected behavior. Therefore, instead of relying on one of the various contact types available in LS-DYNA, the nodes on the bottom surface of the shear stud were merged with the nodes on the top surface of the steel beam. This technique was also used to connect the different layers of the slab to each other, the different layers of the steel beam to each other, as well as the shank of the stud to its head. As for the contact between the slab and the stud and between the slab and the beam, the "Automatic_Single_Surface" contact option was selected. This particular type of contact scans the entire model for parts that are possibly in contact based on a given distance tolerance and adjusts the updated geometry in a way that the nodes of the parts in contact cannot penetrate each other. Although in reality some kind of chemical bond might exist between the concrete and steel parts, this strength is much smaller than that associated with the mechanical interaction of the stud bearing against the concrete. Therefore, it was decided that the above mentioned contact type could accurately capture the composite behavior of interest in this study.

As mentioned in the previous section, the "159-CSM_CONCRETE" material model was used to simulate the concrete behavior. The erosion option was enabled to delete elements that failed. The erosion criterion for this particular concrete model is based on the maximum principal strain. To validate the results against the study of Lam (2005), two different analyses were performed. The first analysis used a concrete compressive strength of 50 MPa, while the second one used a strength of 20 MPa. The steel for the shear stud, steel beam, and reinforcement was modeled as an elastic-

perfectly-plastic material using material model "024-PIECEWISE_LINEAR_PLASTICITY". The properties of those elements were matched to the ones in the study by Lam (2005). Specifically, Young's modulus was 200 GPa, Poisson's ratio was 0.3, the density was $7.8\times10^{-6}$ kg/mm$^3$, and the failure strain was 0.3. The yield stress was defined to be 471 MPa for the shear stud, 275 MPa for the steel beam, and 350 MPa for the reinforcing bars. For the steel reinforcement, four 10-mm diameter bars were used in each direction top and bottom. The bars were modeled as beam elements with the given cross-sectional area and steel properties of the reinforcement. The beam elements were discretized so that the nodes of the bars were merged with the corresponding nodes of the slab. As such, rebar slip was not considered. As far as the element formulation is concerned, fully-integrated, quadratic, 8-node elements with nodal rotations (Element formulation 3) were used for the concrete slab, steel beam, and shear stud, while the "Hughes-Liu with cross section integration" element type was used for all beam elements.

The boundary conditions were chosen to represent the actual behavior as best as possible. The concrete slab was restrained from moving along the *x*-axis (longitudinally) at one end, as indicated by the red arrow in Figure 5-18. The blue arrow shows the location and the direction of the applied load. With this approach, the bearing of the concrete slab against the test floor during the application of the load was simulated.

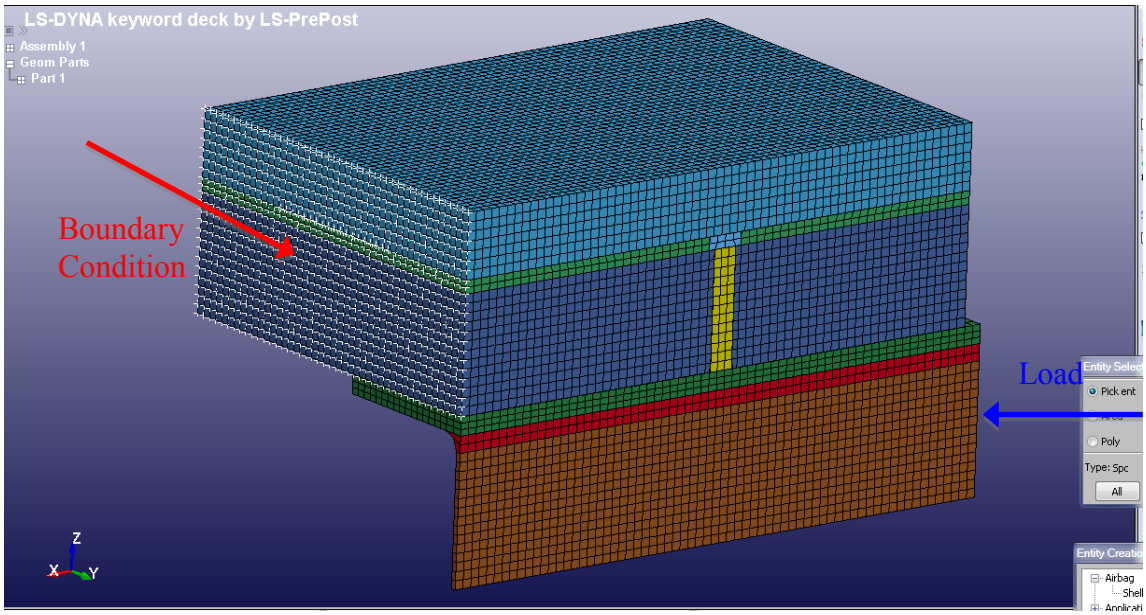


Figure 5-18: Boundary Conditions at the End of the Concrete Slab

The steel beam was also restrained from moving out of plane as can be seen in Figure 5-19. This boundary condition was implemented to account for symmetry. Thus, the surface of the specimen indicated by the red arrows was restrained from moving along the *y*-axis, while the bottom surface of the steel beam (blue arrow) was restrained from moving along the *z*-axis (vertically).

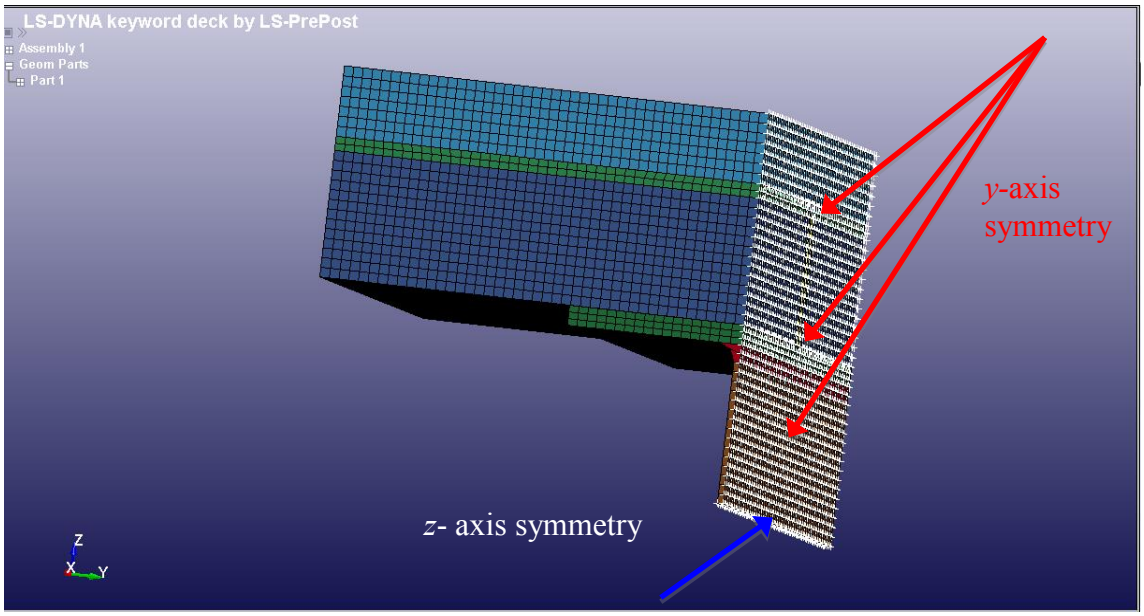


Figure 5-19: Boundary Conditions for Symmetry

The analyses were conducted as a displacement-control test. Prescribed displacements were assigned to the nodes of the steel beam on the side opposite of where the slab was restrained as shown in Figure 5-20. The prescribed displacement varied from 0 to 10 mm over a duration of 1 sec.

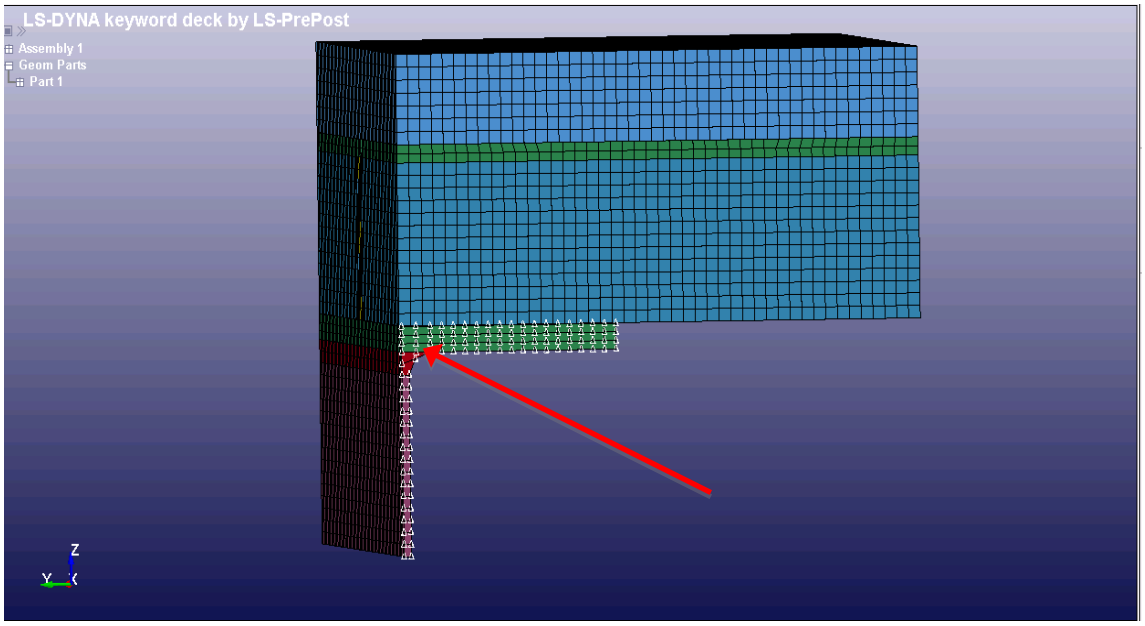


Figure 5-20: Application of Prescribed Displacement

The explicit dynamic solver was used to compute the response, and the load-slip curve was determined based on the output of the model. The final values were multiplied by four because only one-fourth of the specimen was analyzed. Figure 5-21 shows the above mentioned curve for the two different concrete compressive strengths considered along with the results from Lam's 2005 study. Figures 5-22 and 5-23 show the failure modes of the two different analyses. In the first one (50 MPa), stud yielding is the mode of failure, while minor damage appears in the concrete with few slab elements eroding (Figure 5-22). The total shear stud resistance is 135/2 = 67.5 kN (because there are two shear studs in the pull-out test), which coincides with the theoretical shear capacity of a steel element based on the formula $0.58 \times F_u \times$Area. The sudden drop of the corresponding curve in Figure 5-21 occurs due to the failing of the stud at that point of the analysis, which occurs due to excessive deformation of the stud. It is therefore concluded that the assumption of the elastic-perfectly-plastic material, though simple,

can simulate the expected behavior with great accuracy. In the second analysis (20 MPa), concrete crushing is the governing mode of failure, as can be seen in Figure 5-23.

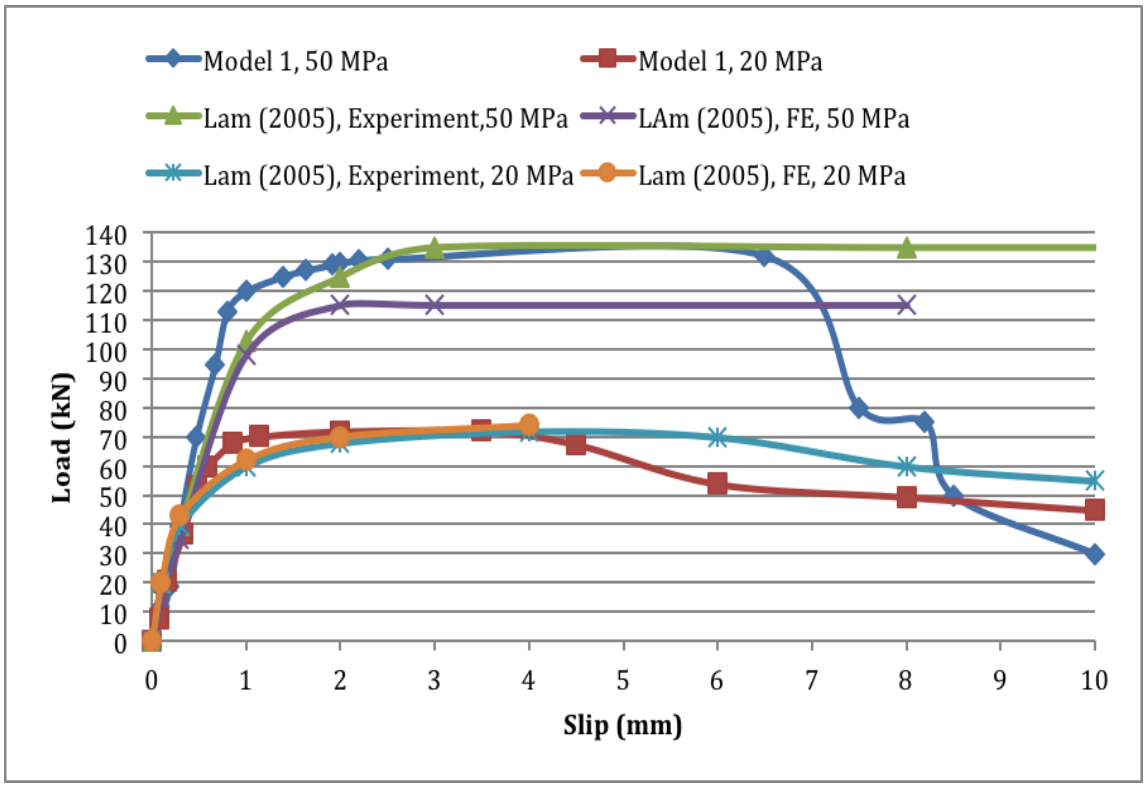


Figure 5-21: Load-Slip Curve for Model 1

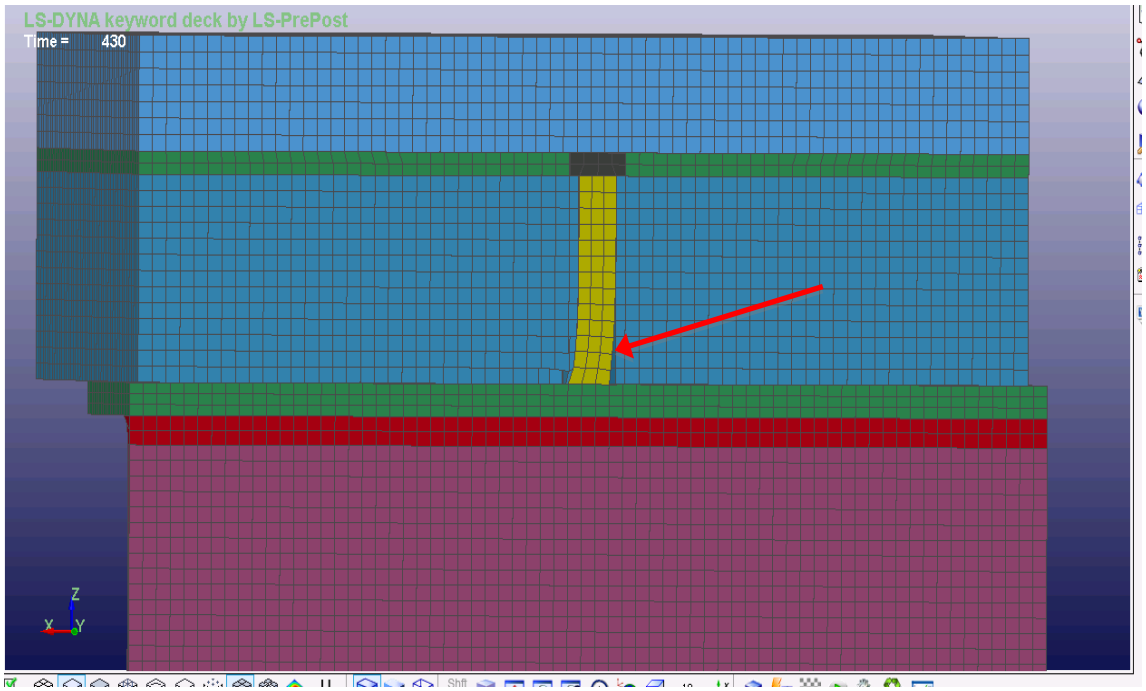


Figure 5-22: Yielding of Shear Stud (50 MPa)

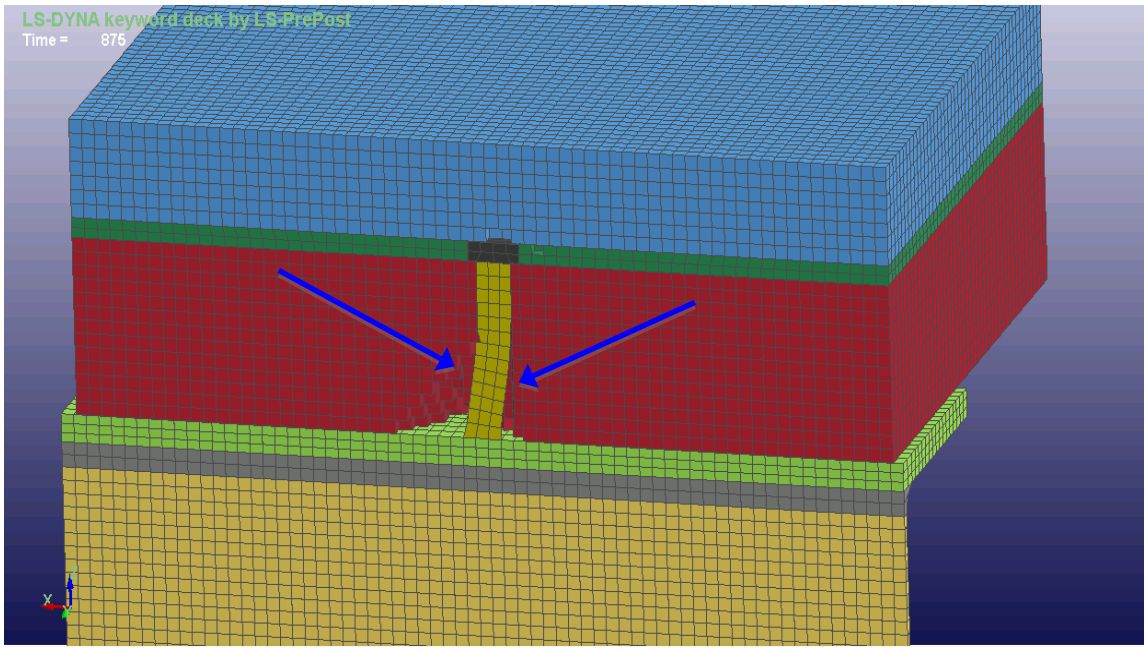


Figure 5-23: Crushing of Concrete (20 MPa)

From the comparison of the two studies, it can be seen clearly that LS-DYNA can accurately capture the composite interaction between the concrete slab and the steel beam. One of the major issues identified during the analyses is the difficulty of the contact algorithm to correctly identify the initial penetrations taking place in the model. Therefore, attention should be paid to the specified tolerance of the initial penetrations input parameter, or a small gap should be placed between the parts of the initial geometry to help the solver avoid tracking penetrations that do not exist.

Despite the fact that the analyses provided good results and proved that LS-DYNA is a powerful tool for simulating composite action, the analysis time was considered to be excessively large for capturing such a detailed aspect of response in simulating progressive collapse of composite floor systems. The fact that such a model is studied to be used as part of a complete progressive collapse analysis makes the use of less complicated models imperative. In the next sections, simpler pull-out models are presented, and their accuracy and efficiency are investigated relative to the results shown in this section. A sample input file for Model 1 is presented in Appendix B.

### *5.2.3 Model 2*

Aside from the manner in which the shear studs were modeled, Model 2 was identical to the first one. Instead of using a three-dimensional shear stud discretized with solid elements, a beam element was utilized to simulate the stud. The "Hughes-Liu with cross section integration" element type was used for the beam elements, and the material properties were the exact same as the first model. The beam was selected to have an outer diameter of 19 mm and a height of 100 mm. For modeling convenience using beam elements, only vertical symmetry was considered. Therefore, half of the full pull-out specimen was analyzed. As far as contact is concerned, the beam element shared a

node with the top of the steel beam to simulate the connection between the beam and the stud. The "Automatic_Single_Surface" contact type was used to define the interaction between the beam and the slab, while the "Automatic_Beams_To_Surface" contact option was utilized for contact between the beam element and the slab. To increase the accuracy of the solution, the shear stud was discretized into 20 beam elements along its height. All the other parameters and solving options were the same as in Model 1. In Figure 5-24, the model with the beam elements is shown. The load-slip curves for both the 50 MPa and 20 MPa concrete are shown in Figure 5-25.

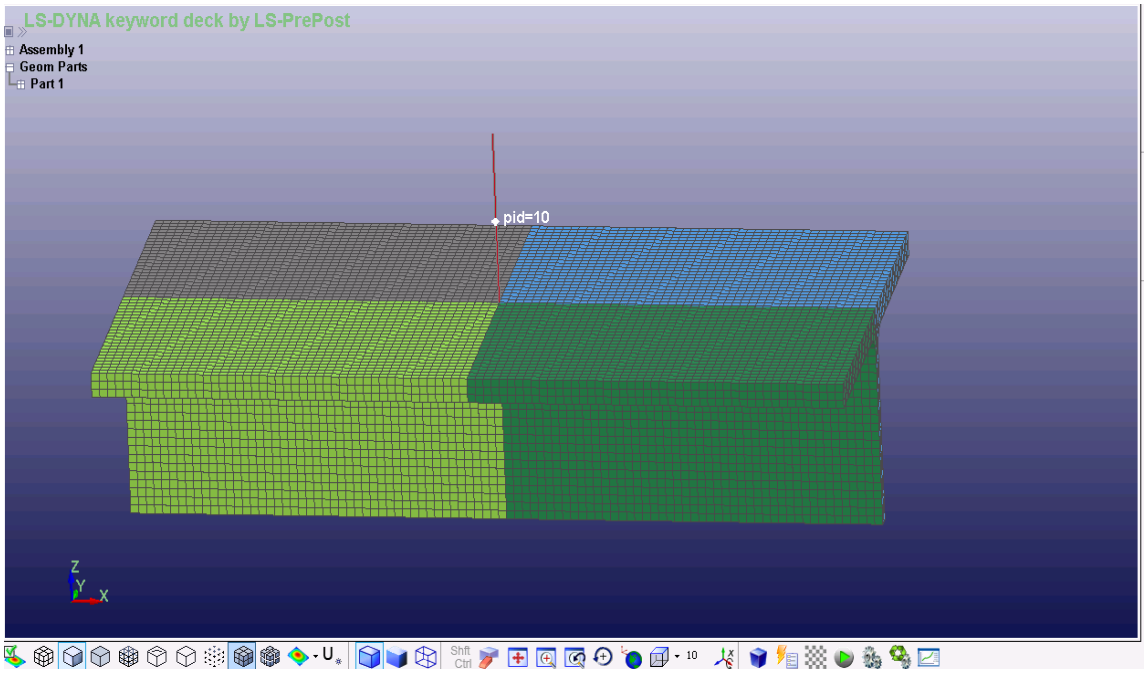


Figure 5-24: Discretized Geometry (Slab not Shown for Clarity)

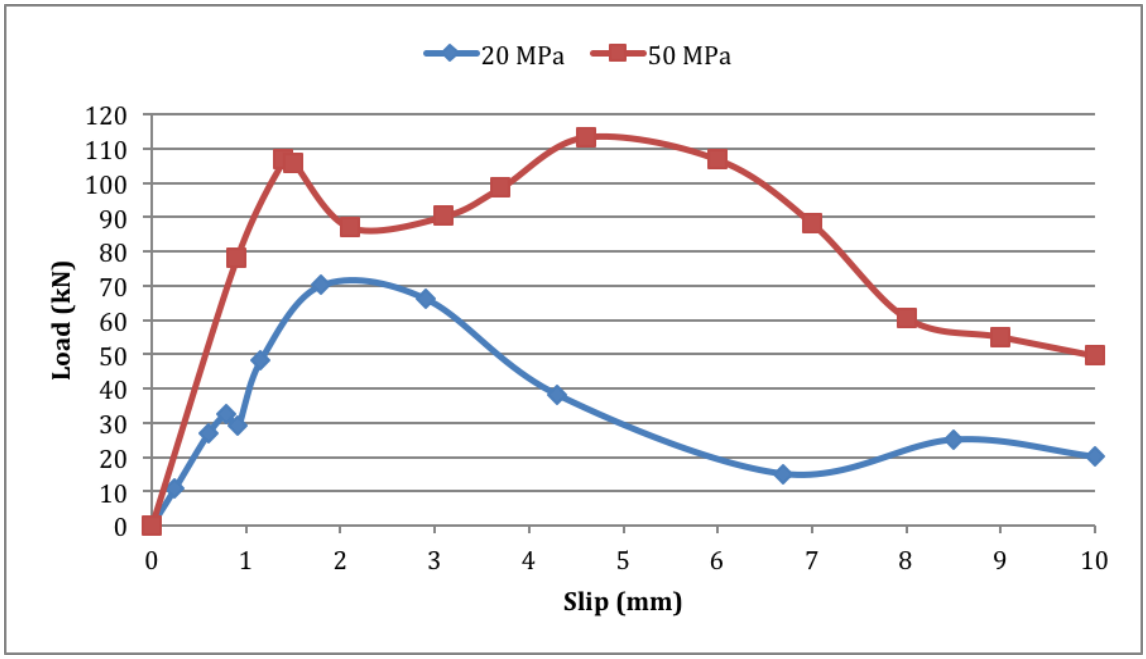


Figure 5-25: Load-Slip Curve for Model 2

The results from this model are similar to those computed using Model 1, though there are some notable differences. A detailed discussion of all analysis models is included in the next section. Importantly, it took approximately half as long to analyze Model 2 as it did Model 1 even though Model 2 used approximately twice as many elements as Model 1 (one-half symmetry versus one-fourth symmetry).

### *5.2.4 Model 3*

The third model was nearly identical to the second one. The primary difference was that a hole was not created in the middle of the concrete slab for the shear stud to be placed in it. To define the interaction between the shear stud and the slab, the stud was discretized into 20 beam elements, and the nodes of the beams were merged with the corresponding nodes of the slab (solid elements). As mentioned before, this technique was used to connect the reinforcing bars with the concrete slab in all three models

presented thus far. All the other parameters and solving options were the same as in Model 2. In Figure 5-26, a comparison between the geometry of Model 2 and Model 3 is presented. Although Model 2 is more realistic, the hole is difficult and time consuming to create and causes difficulties and delays in the meshing procedure. In Figure 5-27 the load-slip curve for Model 3 is provided.

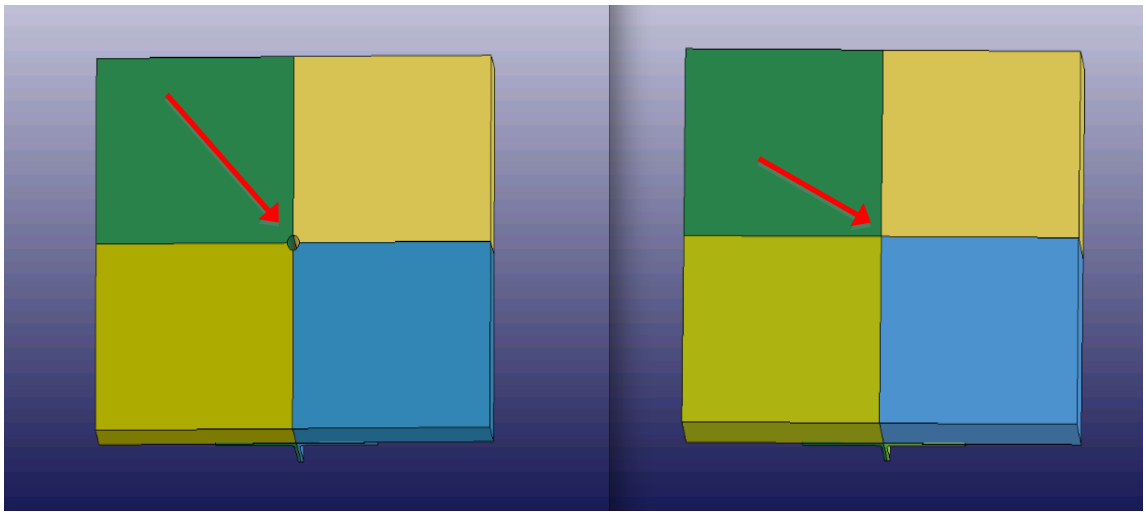

Figure 5-26: Comparison between Model 2 and Model 3

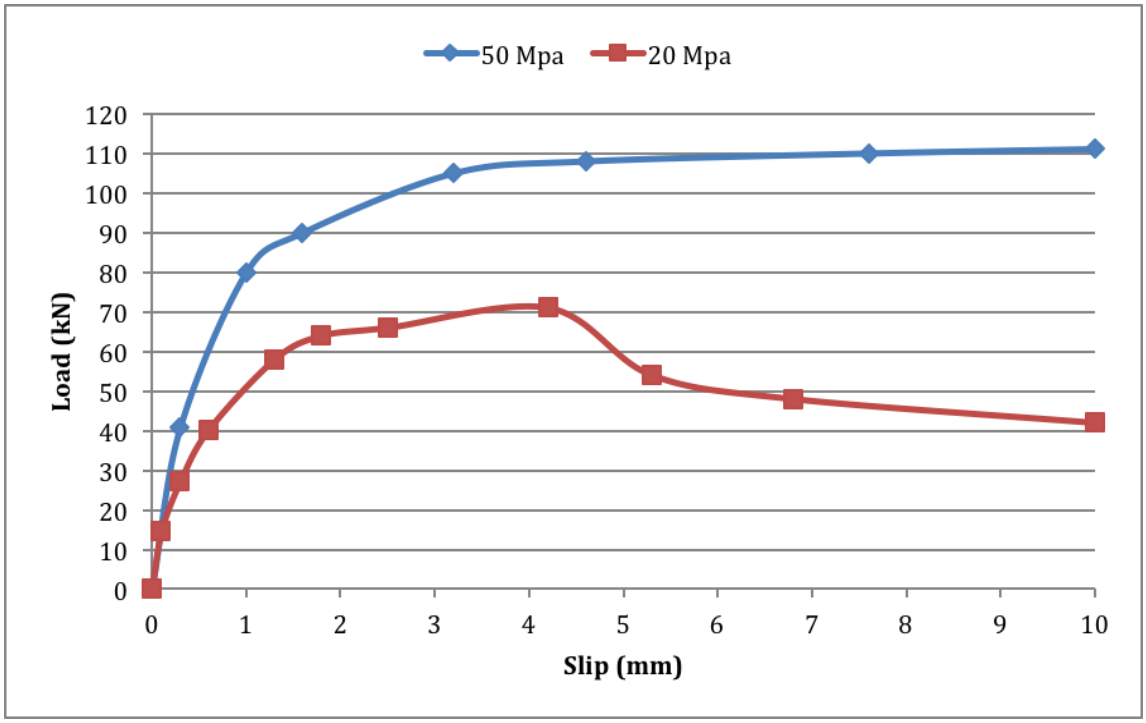


Figure 5-27: Load-Slip Curve for Model 3

The analysis time of this model was approximately 40% the analysis time of the first model.

### *5.2.5 Model 4*

A further reduction of the modeling effort and the computational demand was attempted with the use of Model 4. This model consisted of a steel beam discretized with solid elements, as was the case in all previous models; however, the concrete slab was modeled using shell elements (Belytschko-Tsay), as can be seen in Figure 5-28. The connection between the slab and the beam was modeled using a constraint (SpWeld). This particular constraint consists of a beam element that demonstrates rigid-plastic behavior. The failure stress was defined to be 67.5 kN, which is the theoretical shear strength of a single shear stud. In addition, the elastic-perfectly-plastic material model

"124-PLASTICITY_COMPRESSION_TENSION" was used for the concrete slab because material 159-CSM used in the previous models cannot be used for shell elements. Unlike material model 024, the 124 model allows different behavior in tension and compression, which makes it potentially well suited for modeling concrete. The remaining design and solving parameters were the same as the previous models. After failure of the constraint, the model was expected to demonstrate no further resistance because the shear stud and concrete were modeled separately. As such, once the constraint fails, no composite action can take place.

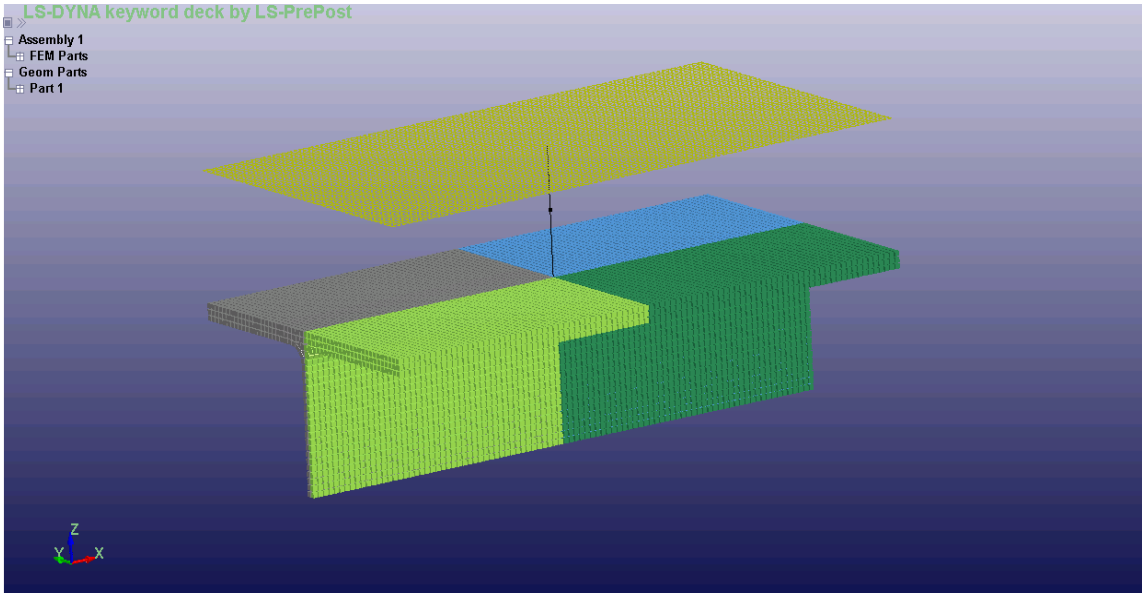


Figure 5-28: Geometry Configuration of Model 4

Although this model appears to offer a simplified approach to representing pull-out test specimens, reasonable results were not obtained. It is speculated that the use of the elastic-perfectly-plastic material model for concrete led to this result. It is likely that the pressure-dependent nature of reinforced concrete cannot be accurately simulated by simply defining the compressive and tensile strength for the concrete material properties.

It is also possible that the use of shell elements for the concrete slab, rather than solids, has oversimplified the problem. Numerous attempts to address these issues were unsuccessful in producing accurate results.

### *5.2.6 Model 5*

The fifth and last model studied attempted to address some of the deficiencies observed with Model 4. The only difference between the two models is that instead of a rigid link, a nonlinear 6 DOF spring was used to connect the beam with the slab. The spring specified from the LS-DYNA library uses material model "119-GENERAL_NONLINEAR_6DOF_DISCRETE_BEAM" along with element formulation 6 "Discrete beam/cable" for the beam section. For this element, the response corresponding to the 6 DOFs at each end is defined by the analyst, and the desired behavior can be readily captured (Figure 5-29). The fact that the response is defined by the user, however, makes this simulation technique unsuitable for pull-out analyses where the response is initially unknown. Instead, this model should be used together with the previous models or with actual pull-out tests. Nonetheless, in the event of a full-scale progressive collapse analysis of a composite building, where hundreds of shear studs might be used, this modeling approach can be employed to significantly reduce computational demands. Prior to using such a model, however, the composite behavior (pull-out response) must be known either using test data or detailed models such as that described for Model 1. Figure 5-30 shows the response of the specimen exactly matches the specified response defined by the analyst. The analysis time for this particular model was about 15% the analysis time for Model 1. Because the entire behavior is governed by the spring, the other parts of the test specimen can be simulated with less detail, depending on the specific problem being solved. For instance, the steel beam can be

modeled with shell elements instead of solid elements to further reduce the computational demand and the analysis time.

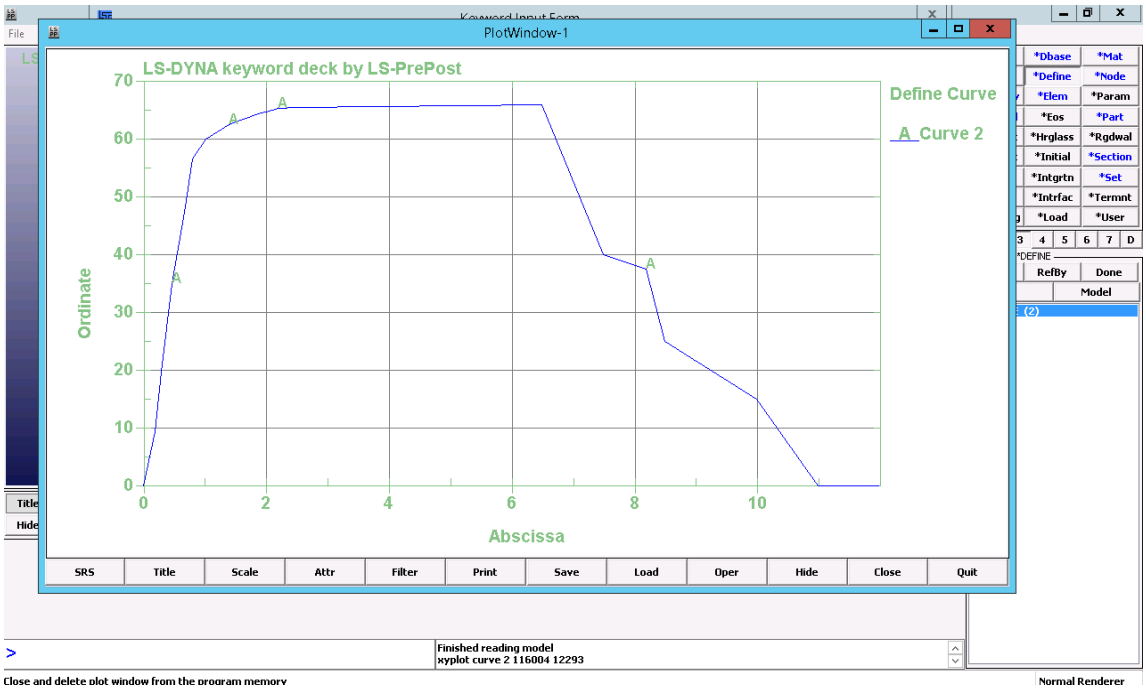


Figure 5-29: User-Defined Response of the Nonlinear Spring (Force versus Displacement)

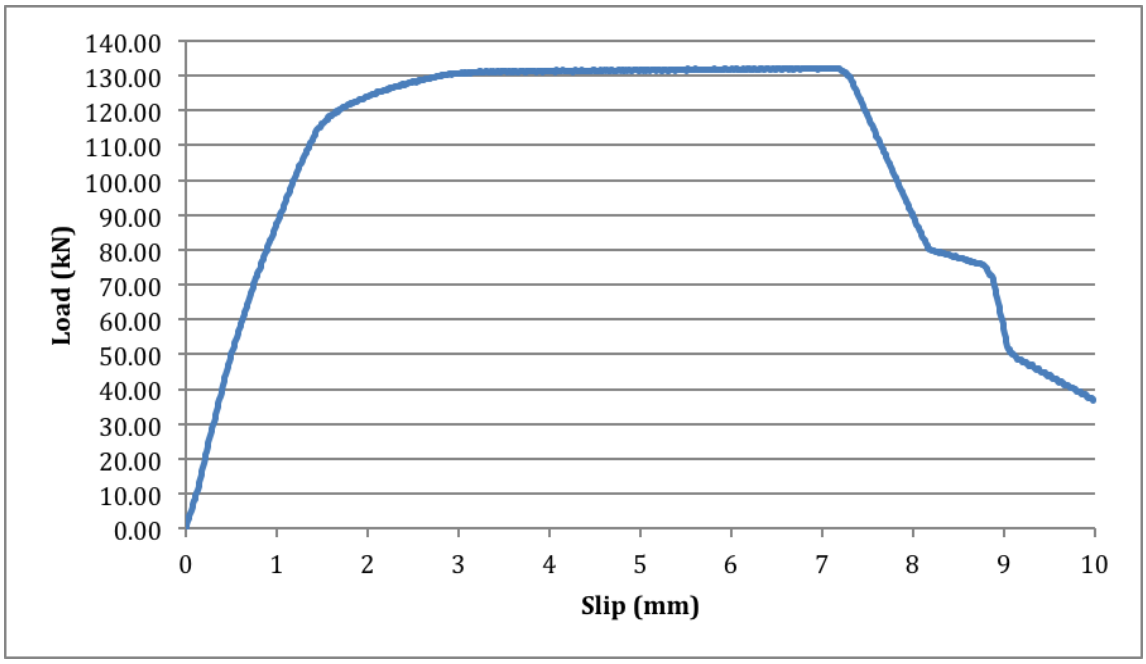


Figure 5-30: Load-Slip Curve for Model 5 (50 MPa Concrete)

### *5.2.7 Comparison*

Figure 5-31 provides a comparison of the first three models for 50 MPa concrete. The fourth and fifth model are not included because Model 4 did not produce useful results and Model 5 is effective only when prior results are known. In Figure 5-32, the same comparison for the 20 MPa concrete case is presented.

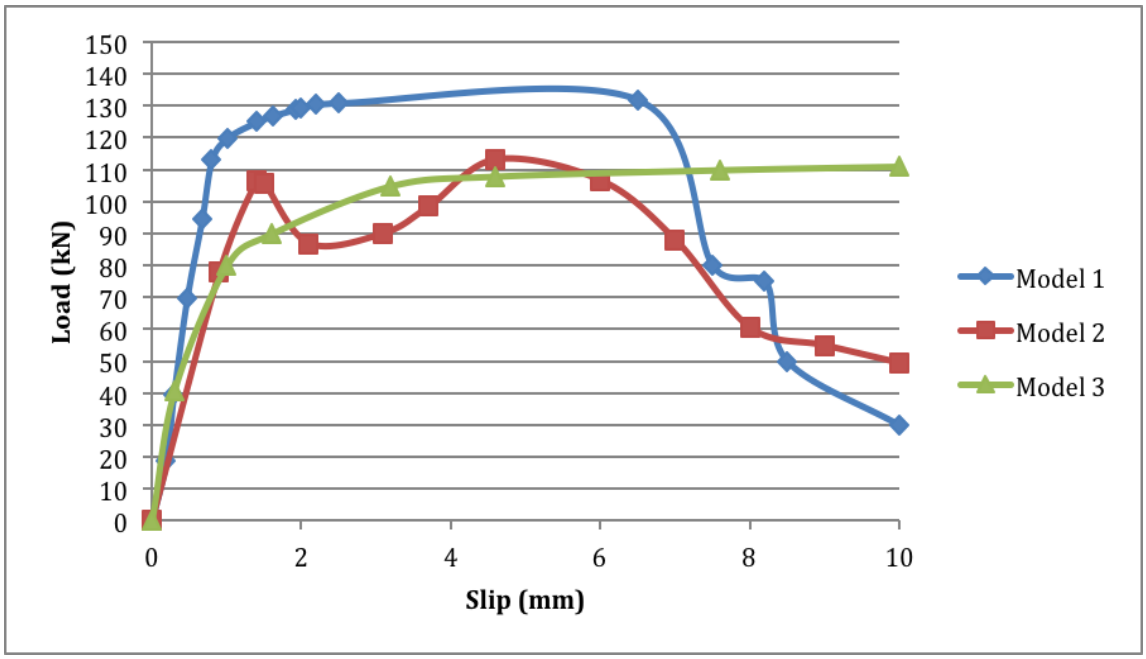


Figure 5-31: Comparison between the Computational Models (50 MPa Concrete)

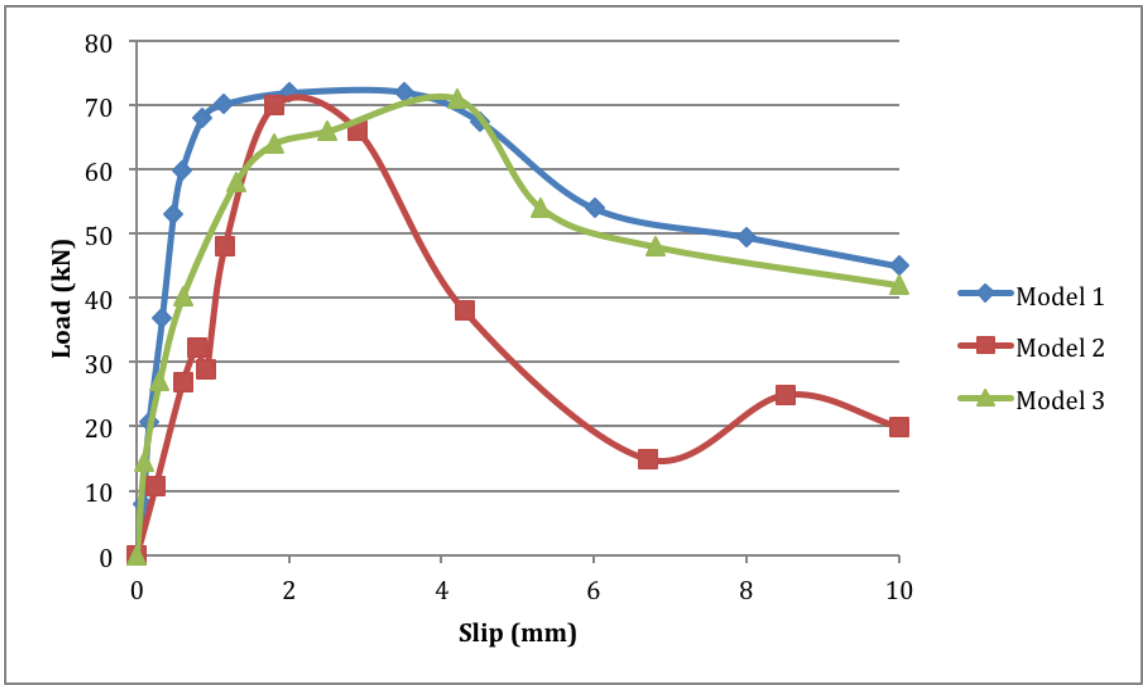


Figure 5-32: Comparison between the Computational Models (20 MPa Concrete)

The above charts show that both Models 2 and 3 can capture the ultimate resistance for the 20 MPa concrete case. For the 50 MPa case, these models appear to underestimate the stud resistance by approximately 20%. For both cases, Model 3 does a good job capturing the initial stiffness, while Model 2 underestimates the initial stiffness relative to the full model (Model 1). Model 3 appears to have a smoother response and tends to match the actual behavior for the 20 MPa case. For the 50 MPa case, Model 3 is unable to capture the fracturing of the shear stud as can be seen in Figure 5-31 where the corresponding curve continues to provide resistance when the other two models have started failing. This can be possibly attributed to the presence of concrete in very close proximity around the shear stud (no hole exists in Model 3), which allows the yielding of the stud but provides increased strength after yielding. For both concrete cases, Model 2 demonstrates instabilities in the behavior; especially for the 20 MPa case, it seems to soften and fail much earlier than the other two models. This can possibly be due to the use of the Beam-To-Surface contact, which might have generated the abrupt jumps that can be seen in the curve.

In general, both models have provided sufficient accuracy and can be used to simulate composite action. However, as mentioned before, when the response of a pull-out specimen can be determined from either detailed finite element software or experimental tests, the use of nonlinear springs to simulate the shear connector is superior both in terms of accuracy and computational demand. Nonetheless, it is unclear how the spring model behaves for different failure modes. Although the pull-out test is a good measurement of the composite behavior of steel-composite floor systems, the response of the above mentioned models should be investigated for other modes of failure as well.

This chapter summarized the computational work conducted within the present thesis to simulate composite action in steel-concrete floor systems. This work is part of a broader computational effort for simulating progressive collapse of typical floor systems in steel-framed buildings. The next chapter provides a brief summary, conclusions, and recommendations for future research based on the work carried out for this thesis.

# CHAPTER 6

# Summary, Conclusions, and Recommendations

## 6.1 Summary and Conclusions

This section summarizes the most significant results from the testing of a 2-bay by 1-bay steel gravity frame with composite floor system under a perimeter column loss scenario. The deflection of the composite floor system at the position of the perimeter column when the actuator was fully disengaged was 5.05 inches. At that point in time, the distributed load on the slab was approximately 115 psf, and the line load on the edge of the specimen was 320 plf. This load is equal to the UFC-specified (DoD, 2009) progressive collapse design load.

The maximum deflection of the specimen just before collapse was 13.6 inches under an approximate load of 190 psf. Based on this result, the DIF of 1.33 specified by the governing UFC (Chapter 3) appears to be a rather conservative value. The additional deflection was 162% of the initial deflection that occurred when the actuator was completely disengaged. Even with the perimeter column missing, the test specimen was also able to resist the ultimate gravity load of $1.2DL + 1.6LL = 180$ psf, which is the governing load case for gravity loads acting statically on the slab.

As for the main girder, assuming the curvature was initially positive when actuator removal was initiated, the flexural stress decreased, and the girder experienced negative flexure during the column removal stage. During the water loading phase, the girder underwent positive bending.

The strains measured in the restraining beams indicate the specimen experienced significant in-plane forces. The magnitude of these forces, however, is dependent on the lateral stiffness provided to the specimen. As such, the ring beam is unable to represent

the demand on neighboring bays of an actual structure for a wide range of scenarios. Nonetheless, the ring beam does provide a consistent means of providing in-plane restraint that is representative of certain idealized conditions found in actual buildings. Because of the repeatability of this setup, it is well suited for laboratory testing.

In general, it was observed that steel gravity frames with composite floor systems have significant reserve capacity. The specimen was able to resist both the dynamic progressive collapse design load and the ultimate gravity load after the perimeter column loss.

As for the computational work described in this thesis, it was concluded that LS-DYNA is a powerful tool for simulating progressive collapse of detailed composite floor system models. The excessive demand in computational resources required for three-dimensional, full-scale models, however, makes the use of simpler models necessary, with the use of nonlinear springs to connect the concrete slabs with the steel beams to be the most accurate, straightforward, fastest and least computationally demanding solution.

## 6.2 RECOMMENDATIONS

Based on the data collected and observations made during the test, the collapse of the specimen was most likely initiated by either failure of the corrugated decking longitudinal seams or by failure of the girder-restraining beam connection. It is therefore suggested that further research with different connection configurations be conducted to determine the contribution of the connections to the capacity of composite floor systems. Furthermore, research to investigate the role of the seams in the corrugated decking on the overall structural behavior should be conducted. It should be mentioned that most

researchers that have included the corrugated decking in their computational analyses have assumed continuous steel decking. Therefore, it would be helpful to actually model the longitudinal seams and the side lap details.

As for the pull-out tests, a model that includes the corrugated decking would provide some insight on the behavior of composite floor systems with steel decking. It is the author's opinion, however, that taking into account this parameter will only change the magnitude of the measured quantities and not the relative behavior between the different simulation techniques. In addition, finite element models that investigate failure modes other than the pull-out mode will shed light on the composite behavior of steel-concrete composite floor systems and will simplify even more the simulation of full-scale finite element models of composite structures under progressive collapse scenarios.

## 6.3 FUTURE WORK

This thesis is part of a broader research project studying progressive collapse resistance of steel gravity frames with composite floor systems. All experimental testing has been completed. Computational work to predict the response of composite floor systems with a missing column is currently ongoing. After these computational models have been validated against the experimental test results, guidance will be provided for developing finite element models that are capable of representing the different failure modes observed during the test program. With such information, engineers can improve their predictions of progressive collapse of typical steel-framed structures and assess the need for enhanced design details for improving performance under a variety of column-removal scenarios.

# APPENDIX A

## Calculation of the Dynamic Impact Factor

The DIF was determined based on the equation within Table 3-5 of paragraph 3-2.15.5 of the governing UFC (DoD, 2009) manual:

$$1.08 + 0.76/(\theta_{pra}/\theta_y + 0.83) \quad (1)$$

where $\theta_{pra}$ is the plastic rotation angle and $\theta_y$ is the yield rotation. Based on ASCE 41-06 (ASCE, 2006), three different states were considered: Immediate Occupancy, Life Safety, and Collapse Prevention. From Table 5-6 of ASCE 41-06 and for the case of "Shear Connection with Slab", $\theta_{pra}$ is given by the following formulas:

- Immediate Occupancy: $0.014 - 0.00010 \times d_{bg} = 0.0136$
- Life Safety: $0.1125 - 0.0027 \times d_{bg} = 0.1017$
- Collapse Prevention: $0.15 - 0.0036 \times d_{bg} = 0.1356$

where $d_{bg}$ is the depth of the connection, which is equal to 4 inches.

Based on equation 5-1 of ASCE 41-06, $\theta_y$ is given by the formula: $\theta_y = Z \times F_{ye} \times l_b / (6EI_b)$, where $Z$ is the plastic section modulus, $F_{ye}$ is the expected yield strength of the material, $E$ is the modulus of elasticity, $l_b$ is the length of the beam, and $I_b$ is the moment of inertia of the beam. For the properties of the W6×9 beam (worst case), for the length of 179.5 inches, and for an assumed estimated yield strength of 50 ksi, $\theta_y = 0.01959$.

From equation (1) and for the three different states:

- Immediate Occupancy: DIF = 1.58

- Life Safety: DIF = 1.21
- Collapse Prevention: DIF = 1.18

The final DIF was taken as the average of the three above cases, equal to 1.33.

# APPENDIX B

## Sample LS-DYNA Input File

Date: 01/28/2014 Time: 13:37:21

```
 _____________________________________________

|                                             |
| Livermore  Software  Technology  Corporation  |
|                                             |
| 7374 Las Positas Road                       |
| Livermore, CA 94551                         |
| Tel: (925) 449-2500  Fax: (925) 449-2507    |
| www.lstc.com                                |
|_____________________________________________|
|                                             |
| LS-DYNA, A Program for Nonlinear Dynamic    |
| Analysis of Structures in Three Dimensions  |
| Version : smp s R7.0.0  Date: 01/10/2013    |
| Revision: 79055         Time: 16:39:15      |
|                                             |
| Features enabled in this version:           |
|  Shared Memory Parallel                     |
|  Interactive Graphics                       |
|  ANSYS Database format                      |
|  NSYS License (ANSYS145)                    |
```

|  |

| Licensed to: University of Texas at Austin Ferg|

The native file format  : 32-bit small endian

Memory size from command line:  150000000

**********

Solid1

part  id .....  1

section  id .....  1

material id .....  2

section  title .....

material title .....

Steel beam

material type .....  24

equation-of-state type .....  0

hourglass type ..... 4

bulk viscosity type ..... 1

density ..... = 7.80000E-06

hourglass coefficient ..... = 1.00000E-01

quadratic bulk viscosity ..... = 1.50000E+00

linear bulk viscosity ..... = 6.00000E-02

element type ..... = 0

eq.0: 4, 6, 8, 10-node solid element or SPH element

eq.1: 2-node beam or truss or 2D shell element

eq.2: 3, 4-node membrane/shell or 2D continuum element

eq.3: 8-node thick shell element

flag for bulk viscosity in shells. = 0

flag for rbdout/matsum output ... = 0

eq.0: rbdout and matsum

eq.1: rbdout only

eq.2: matsum only

eq.3: no output

static coefficient of friction ... = 0.00000E+00

kinetic coefficient of friction... = 0.00000E+00

exponential decay coefficient .... = 0.00000E+00

viscous friction coefficient ..... = 0.00000E+00

optional contact thickness ..... = 0.00000E+00

optional thickness scale factor... = 0.00000E+00

local penalty scale factor..... = 0.00000E+00

flag for adaptive remeshing ..... = 0

eq.0: inactive

eq.1: h-adaptive only

eq.2: r-adaptive only

rayleigh damping coefficient..... = 0.00000E+00

e ..... = 2.00000E+02

strainrate parameter, c ..... = 0.00000E+00

strainrate parameter, p ..... = 0.00000E+00

formulation for rate effects ..... = 0.00000E+00

eq.-1.0: deviatoric strain rate

eq. 0.0: default

eq. 1.0: viscoplastic strain rate

vnu ..... = 3.00000E-01

yield ..... = 2.75000E-01

curve # for stress vs. strain .... = 0

e (harden) ..... = 0.00000E+00

plastic strain at failure, fs .... = 3.00000E-01

gt.0: active

eq.0: inactive

lt.0: user subroutine supplied for

failure and failure strain

is set to |fs|

strain ..... = 0.00E+00 0.00E+00 0.00E+00 0.00E+00

0.00E+00 0.00E+00 0.00E+00 0.00E+00

stress ..... = 0.00E+00  0.00E+00  0.00E+00  0.00E+00

0.00E+00  0.00E+00  0.00E+00  0.00E+00

curve # for strainrate effects ... = 0

time step size for element deletion= 0.00000E+00

stochastic flag..... = 0.00000E+00

eq.0.0: standard model

eq.1.0: stochastic model

solid  formulation ..... = 3

**********

Solid2

part id ..... 2

section id ..... 1

material id ..... 3

section title .....

material title .....

Concrete

material type ..... 159

equation-of-state type ..... 0

hourglass type ..... 4

bulk viscosity type ..... 1

density ..... = 2.50000E-06

hourglass coefficient ..... = 1.00000E-01

quadratic bulk viscosity ..... = 1.50000E+00

linear bulk viscosity ..... = 6.00000E-02

element type ..... = 0

eq.0: 4, 6, 8, 10-node solid element or SPH element

eq.1: 2-node beam or truss or 2D shell element

eq.2: 3, 4-node membrane/shell or 2D continuum element

eq.3: 8-node thick shell element

flag for bulk viscosity in shells. = 0

flag for rbdout/matsum output ... = 0

eq.0: rbdout and matsum

eq.1: rbdout only

eq.2: matsum only

eq.3: no output

static coefficient of friction ... = 0.00000E+00

kinetic coefficient of friction... = 0.00000E+00

exponential decay coefficient .... = 0.00000E+00

viscous friction coefficient ..... = 0.00000E+00

optional contact thickness ..... = 0.00000E+00

optional thickness scale factor... = 0.00000E+00

local penalty scale factor..... = 0.00000E+00

flag for adaptive remeshing ..... = 0

eq.0: inactive

eq.1: h-adaptive only

eq.2: r-adaptive only

rayleigh damping coefficient..... = 0.00000E+00

Control Parameters:

Nplot Plotting Option.....= 1.0000E+00

Incre Strain increment for subincrementation.= 2.0272E-05

Irate Rate Effects Option.....= 0.0000E+00

eq. 0: Rate effects off (default)

eq. 1: Rate effects on

Erode Erosion.....= 1.0000E+00

lt. 1: Erosion off

gt. 1: Erosion on

Erode elements when the maximum principal

strain exceeds value minus one

Recover Recover modulus in compression.....= 0.0000E+00

Iretract Cap retraction option.....= 0.0000E+00

eq. 0: Cap does not retract (default)

eq. 1: Cap retracts

Predam Initial damage in concrete.....= 0.0000E+00

Stiffness:

Shear Shear Modulus.....= 1.3590E+01

Bulk Bulk Modulus.....= 1.4880E+01

TXC Surface:

alpha TXC surface constant term.....= 1.6020E-02

theta TXC surface linear term.....= 3.6480E-01

lambda TXC surface nonlinear term.....= 1.0510E-02

beta TXC surface exponent.....= 1.9290E+01

TOR Surface Scaling Factors:

alpha TOR surface constant term.....= 7.4730E-01

theta TOR surface linear term.....= 4.7500E-01

lambda TOR surface nonlinear term.....= 1.7000E-01

beta TOR surface exponent.....= 4.3140E+01

TXE Surface Scaling Factors:

alpha TXE surface constant term.....= 6.6000E-01

theta TXE surface linear term.....= 5.7040E-01

lambda TXE surface nonlinear term.....= 1.6000E-01

beta TXE surface exponent.....= 4.3140E+01

Shear Surface Hardening Parameters:

NH Hardening initiation.....= 1.0000E+00

CH Hardening rate.....= 0.0000E+00

Cap and Cap Hardening Parameters:

R Cap surface aspect ratio..... .= 5.0000E+00

Xo Cap pressure axis intercept .....= 1.0310E-01

W Hardening law maximum compaction.....= 5.0000E-02

D1 Hardening law linear exponent.....= 2.5000E-01

D2 Hardening law nonlinear exponent.....= 3.4920E-01

Damage Parameters:

B Compressive softening parameter.....= 1.0000E+02

Gfc Compressive fracture energy.....= 9.7850E-03

D Tensile/shear softening parameter.....= 1.0000E-01

Gft Tensile fracture energy.....= 9.7850E-05

Gfs Shear fracture energy.....= 9.7850E-05

pwrc  Compressive damage transition power.....=  5.0000E+00

pwrt  Tensile damage transition power.....=  1.0000E+00

pmod  Moderate pressure fit adjustment.....=  0.0000E+00

Rate Effects Parameters:

flpar1  Compressive fluidity parameter.....=  1.0160E-03

power1  Compressive power.....=  7.8000E-01

flpar1  Tensile fluidity parameter.....=  3.1250E-03

power2  Tensile power.....=  4.8000E-01

overc  Compressive overstress limit.....=  3.4550E-02

overt  Tensile overstress limit.....=  3.4550E-02

sratio  Ratio of shear to tensile parameter.....=  1.0000E+00

repow  Power applied to fracture energies.....=  1.0000E+00

Miscellaeous Output Parameters:

si1  Pressure apex of shear surface.....= -9.3859E-03

hkmin  Minimum cap location .....=  1.0000E-06

hk0  Initial cap location .....=  2.0641E-02

hkcr  Critical cap location .....=  1.0000E+20

solid  formulation ..... =  3

**********

Solid3

part  id .....  3

section  id .....  1

material id .....  2

section  title .....

material title .....

Steel beam

material type .....  24

equation-of-state type .....  0

hourglass type .....  4

bulk viscosity type .....  1

density ..... = 7.80000E-06

hourglass coefficient ..... = 1.00000E-01

quadratic bulk viscosity ..... = 1.50000E+00

linear bulk viscosity ..... = 6.00000E-02

element type ..... =  0

flag for bulk viscosity in shells. =  0

flag for rbdout/matsum  output ... =  0

eq.0: rbdout and matsum

eq.1: rbdout only

eq.2: matsum only

eq.3: no output

static coefficient of friction ... = 0.00000E+00

kinetic coefficient of friction... = 0.00000E+00

exponential decay coefficient .... = 0.00000E+00

viscous friction coefficient ..... = 0.00000E+00

optional contact thickness ..... = 0.00000E+00

optional thickness scale factor... = 0.00000E+00

local penalty scale factor..... = 0.00000E+00

flag for adaptive remeshing ..... = 0

eq.0: inactive

eq.1: h-adaptive only

eq.2: r-adaptive only

rayleigh damping coefficient..... = 0.00000E+00

e ..... = 2.00000E+02

strainrate parameter, c ..... = 0.00000E+00

strainrate parameter, p ..... = 0.00000E+00

formulation for rate effects ..... = 0.00000E+00

eq.-1.0: deviatoric strain rate

eq. 0.0: default

eq. 1.0: viscoplastic strain rate

vnu ..... = 3.00000E-01

yield ..... = 2.75000E-01

curve # for stress vs. strain .... = 0

e (harden) ..... = 0.00000E+00

plastic strain at failure, fs .... = 3.00000E-01

gt.0: active

eq.0: inactive

lt.0: user subroutine supplied for

failure and failure strain

is set to |fs|

strain ..... = 0.00E+00  0.00E+00  0.00E+00  0.00E+00

0.00E+00  0.00E+00  0.00E+00  0.00E+00

stress ..... = 0.00E+00  0.00E+00  0.00E+00  0.00E+00

0.00E+00  0.00E+00  0.00E+00  0.00E+00

curve # for strainrate effects ... = 0

time step size for element deletion= 0.00000E+00

stochastic flag..... = 0.00000E+00

eq.0.0: standard model

eq.1.0: stochastic model

solid formulation ..... = 3

**********

Solid4

part id ..... 4

section id ..... 1

material id ..... 1

section title .....

material title .....

Shear Stud

material type ..... 24

equation-of-state type ..... 0

hourglass type ..... 4

bulk viscosity type ..... 1

density ..... = 7.80000E-06

hourglass coefficient ..... = 1.00000E-01

quadratic bulk viscosity ..... = 1.50000E+00

linear bulk viscosity ..... = 6.00000E-02

element type ..... = 0

flag for bulk viscosity in shells. = 0

flag for rbdout/matsum output ... = 0

eq.0: rbdout and matsum

eq.1: rbdout only

eq.2: matsum only

eq.3: no output

static coefficient of friction ... = 0.00000E+00

kinetic coefficient of friction... = 0.00000E+00

exponential decay coefficient .... = 0.00000E+00

viscous friction coefficient ..... = 0.00000E+00

optional contact thickness ..... = 0.00000E+00

optional thickness scale factor... = 0.00000E+00

local penalty scale factor..... = 0.00000E+00

flag for adaptive remeshing ..... = 0

eq.0: inactive

eq.1: h-adaptive only

eq.2: r-adaptive only

rayleigh damping coefficient..... = 0.00000E+00

e ..... = 2.00000E+02

strainrate parameter, c ..... = 0.00000E+00

strainrate parameter, p ..... = 0.00000E+00

formulation for rate effects ..... = 0.00000E+00

eq.-1.0: deviatoric strain rate

eq. 0.0: default

eq. 1.0: viscoplastic strain rate

vnu ..... = 3.00000E-01

yield ..... = 4.71000E-01

curve # for stress vs. strain .... = 0

e (harden) ..... = 0.00000E+00

plastic strain at failure, fs .... = 3.00000E-01

gt.0: active

eq.0: inactive

lt.0: user subroutine supplied for

failure and failure strain

is set to |fs|

strain ..... = 0.00E+00 0.00E+00 0.00E+00 0.00E+00

0.00E+00 0.00E+00 0.00E+00 0.00E+00

stress ..... = 0.00E+00 0.00E+00 0.00E+00 0.00E+00

0.00E+00 0.00E+00 0.00E+00 0.00E+00

curve # for strainrate effects ... = 0

time step size for element deletion= 0.00000E+00

stochastic flag..... = 0.00000E+00

eq.0.0: standard model

eq.1.0: stochastic model

solid formulation ..... = 3

corotational local coord. ..... = 0

eq. 0: not requested

eq. 1: requested

**********

Solid5

part id ..... 5

section id ..... 1

material id ..... 2

section title .....

material title .....

Steel beam

material type ..... 24

equation-of-state type ..... 0

hourglass type ..... 4

bulk viscosity type ..... 1

density ..... = 7.80000E-06

hourglass coefficient ..... = 1.00000E-01

quadratic bulk viscosity ..... = 1.50000E+00

linear bulk viscosity ..... = 6.00000E-02

element type ..... = 0

flag for bulk viscosity in shells. = 0

flag for rbdout/matsum output ... = 0

eq.0: rbdout and matsum

eq.1: rbdout only

eq.2: matsum only

eq.3: no output

static coefficient of friction ... = 0.00000E+00

kinetic coefficient of friction... = 0.00000E+00

exponential decay coefficient .... = 0.00000E+00

viscous friction coefficient ..... = 0.00000E+00

optional contact thickness ..... = 0.00000E+00

optional thickness scale factor... = 0.00000E+00

local penalty scale factor..... = 0.00000E+00

flag for adaptive remeshing ..... = 0

eq.0: inactive

eq.1: h-adaptive only

eq.2: r-adaptive only

rayleigh damping coefficient..... = 0.00000E+00

e ..... = 2.00000E+02

strainrate parameter, c ..... = 0.00000E+00

strainrate parameter, p ..... = 0.00000E+00

formulation for rate effects ..... = 0.00000E+00

eq.-1.0: deviatoric strain rate

eq. 0.0: default

eq. 1.0: viscoplastic strain rate

vnu ..... = 3.00000E-01

yield ..... = 2.75000E-01

curve # for stress vs. strain .... = 0

e (harden) ..... = 0.00000E+00

plastic strain at failure, fs .... = 3.00000E-01

gt.0: active

eq.0: inactive

lt.0: user subroutine supplied for

failure and failure strain

is set to |fs|

strain ..... = 0.00E+00 0.00E+00 0.00E+00 0.00E+00

0.00E+00 0.00E+00 0.00E+00 0.00E+00

stress ..... = 0.00E+00 0.00E+00 0.00E+00 0.00E+00

0.00E+00 0.00E+00 0.00E+00 0.00E+00

curve # for strainrate effects ... = 0

time step size for element deletion= 0.00000E+00

stochastic flag..... = 0.00000E+00

eq.0.0: standard model

eq.1.0: stochastic model

solid formulation ..... = 3

**********

Solid6

part id ..... 6

section id ..... 1

material id ..... 1

section title .....

material title .....

Shear Stud

material type ..... 24

equation-of-state type ..... 0

hourglass type ..... 4

bulk viscosity type ..... 1

density ..... = 7.80000E-06

hourglass coefficient ..... = 1.00000E-01

quadratic bulk viscosity ..... = 1.50000E+00

linear bulk viscosity ..... = 6.00000E-02

element type ..... = 0

eq.0: 4, 6, 8, 10-node solid element or SPH element

eq.1: 2-node beam or truss or 2D shell element

eq.2: 3, 4-node membrane/shell or 2D continuum element

eq.3: 8-node thick shell element

flag for bulk viscosity in shells. = 0

flag for rbdout/matsum output ... = 0

eq.0: rbdout and matsum

eq.1: rbdout only

eq.2: matsum only

eq.3: no output

static coefficient of friction ... = 0.00000E+00

kinetic coefficient of friction... = 0.00000E+00

exponential decay coefficient .... = 0.00000E+00

viscous friction coefficient ..... = 0.00000E+00

optional contact thickness ..... = 0.00000E+00

optional thickness scale factor... = 0.00000E+00

local penalty scale factor..... = 0.00000E+00

flag for adaptive remeshing ..... = 0

eq.0: inactive

eq.1: h-adaptive only

eq.2: r-adaptive only

rayleigh damping coefficient..... = 0.00000E+00

e ..... = 2.00000E+02

strainrate parameter, c ..... = 0.00000E+00

strainrate parameter, p ..... = 0.00000E+00

formulation for rate effects ..... = 0.00000E+00

eq.-1.0: deviatoric strain rate

eq. 0.0: default

eq. 1.0: viscoplastic strain rate

vnu ..... = 3.00000E-01

yield ..... = 4.71000E-01

curve # for stress vs. strain .... = 0

e (harden) ..... = 0.00000E+00

plastic strain at failure, fs .... = 3.00000E-01

gt.0: active

eq.0: inactive

lt.0: user subroutine supplied for

failure and failure strain

is set to |fs|

strain ..... = 0.00E+00 0.00E+00 0.00E+00 0.00E+00

0.00E+00 0.00E+00 0.00E+00 0.00E+00

stress ..... = 0.00E+00 0.00E+00 0.00E+00 0.00E+00

0.00E+00 0.00E+00 0.00E+00 0.00E+00

curve # for strainrate effects ... = 0

time step size for element deletion= 0.00000E+00

stochastic flag..... = 0.00000E+00

eq.0.0: standard model

eq.1.0: stochastic model

solid formulation ..... = 3

eq.-2: 8 point integration-3dof/node

for poor aspect ratio elements

**********

Solid7

part id ..... 7

section id ..... 1

material id ..... 3

section title .....

material title .....

Concrete

material type ..... 159

equation-of-state type ..... 0

hourglass type ..... 4

bulk viscosity type ..... 1

density ..... = 2.50000E-06

hourglass coefficient ..... = 1.00000E-01

quadratic bulk viscosity ..... = 1.50000E+00

linear bulk viscosity ..... = 6.00000E-02

element type ..... = 0

flag for bulk viscosity in shells. = 0

flag for rbdout/matsum output ... = 0

eq.0: rbdout and matsum

eq.1: rbdout only

eq.2: matsum only

eq.3: no output

static coefficient of friction ... = 0.00000E+00

kinetic coefficient of friction... = 0.00000E+00

exponential decay coefficient .... = 0.00000E+00

viscous friction coefficient ..... = 0.00000E+00

optional contact thickness ..... = 0.00000E+00

optional thickness scale factor... = 0.00000E+00

local penalty scale factor..... = 0.00000E+00

flag for adaptive remeshing ..... = 0

eq.0: inactive

eq.1: h-adaptive only

eq.2: r-adaptive only

rayleigh damping coefficient..... = 0.00000E+00

Control Parameters:

Nplot Plotting Option.....= 1.0000E+00

Incre Strain increment for subincrementation.= 2.0272E-05

Irate Rate Effects Option.....= 0.0000E+00

eq. 0: Rate effects off (default)

eq. 1: Rate effects on

Erode Erosion.....= 1.0000E+00

lt. 1: Erosion off

gt. 1: Erosion on

Erode elements when the maximum principal

strain exceeds value minus one

Recover Recover modulus in compression.....= 0.0000E+00

Iretract Cap retraction option.....= 0.0000E+00

eq. 0: Cap does not retract (default)

eq. 1: Cap retracts

Predam Initial damage in concrete.....= 0.0000E+00

Stiffness:

Shear Shear Modulus.....= 1.3590E+01

Bulk Bulk Modulus.....= 1.4880E+01

TXC Surface:

alpha TXC surface constant term.....= 1.6020E-02

theta TXC surface linear term.....= 3.6480E-01

lambda TXC surface nonlinear term.....= 1.0510E-02

beta TXC surface exponent.....= 1.9290E+01

TOR Surface Scaling Factors:

alpha TOR surface constant term.....= 7.4730E-01

theta TOR surface linear term.....= 4.7500E-01

lambda TOR surface nonlinear term.....= 1.7000E-01

beta TOR surface exponent.....= 4.3140E+01

TXE Surface Scaling Factors:

alpha TXE surface constant term.....= 6.6000E-01

theta TXE surface linear term.....= 5.7040E-01

lambda TXE surface nonlinear term.....= 1.6000E-01

beta TXE surface exponent.....= 4.3140E+01

Shear Surface Hardening Parameters:

NH Hardening initiation.....= 1.0000E+00

CH Hardening rate.....= 0.0000E+00

Cap and Cap Hardening Parameters:

R Cap surface aspect ratio..... .= 5.0000E+00

Xo Cap pressure axis intercept .....= 1.0310E-01

W Hardening law maximum compaction.....= 5.0000E-02

D1 Hardening law linear exponent.....= 2.5000E-01

D2 Hardening law nonlinear exponent.....= 3.4920E-01

Damage Parameters:

B Compressive softening parameter.....= 1.0000E+02

Gfc Compressive fracture energy.....= 9.7850E-03

D Tensile/shear softening parameter.....= 1.0000E-01

Gft Tensile fracture energy.....= 9.7850E-05

Gfs Shear fracture energy.....= 9.7850E-05

pwrc Compressive damage transition power.....= 5.0000E+00

pwrt Tensile damage transition power.....= 1.0000E+00

pmod Moderate pressure fit adjustment.....= 0.0000E+00

Rate Effects Parameters:

flpar1 Compressive fluidity parameter.....= 1.0160E-03

power1 Compressive power.....= 7.8000E-01

flpar1 Tensile fluidity parameter.....= 3.1250E-03

power2 Tensile power.....= 4.8000E-01

overc Compressive overstress limit.....= 3.4550E-02

overt Tensile overstress limit.....= 3.4550E-02

sratio Ratio of shear to tensile parameter.....= 1.0000E+00

repow Power applied to fracture energies.....= 1.0000E+00

Miscellaeous Output Parameters:

si1 Pressure apex of shear surface.....= -9.3859E-03

hkmin Minimum cap location .....= 1.0000E-06

hk0 Initial cap location .....= 2.0641E-02

hkcr Critical cap location .....= 1.0000E+20

solid formulation ..... = 3

**********

Solid8

part id ..... 8

section id ..... 1

material id ..... 3

section title .....

material title .....

Concrete

material type ..... 159

equation-of-state type ..... 0

hourglass type ..... 4

bulk viscosity type ..... 1

density ..... = 2.50000E-06

hourglass coefficient ..... = 1.00000E-01

quadratic bulk viscosity ..... = 1.50000E+00

linear bulk viscosity ..... = 6.00000E-02

element type ..... = 0

eq.0: 4, 6, 8, 10-node solid element or SPH element

eq.1: 2-node beam or truss or 2D shell element

eq.2: 3, 4-node membrane/shell or 2D continuum element

eq.3: 8-node thick shell element

flag for bulk viscosity in shells. = 0

flag for rbdout/matsum output ... = 0

static coefficient of friction ... = 0.00000E+00

kinetic coefficient of friction... = 0.00000E+00

exponential decay coefficient .... = 0.00000E+00

viscous friction coefficient ..... = 0.00000E+00

optional contact thickness ..... = 0.00000E+00

optional thickness scale factor... = 0.00000E+00

local penalty scale factor..... = 0.00000E+00

flag for adaptive remeshing ..... = 0

eq.0: inactive

eq.1: h-adaptive only

eq.2: r-adaptive only

rayleigh damping coefficient..... = 0.00000E+00

Control Parameters:

Nplot Plotting Option.....= 1.0000E+00

Incre Strain increment for subincrementation.= 2.0272E-05

Irate Rate Effects Option.....= 0.0000E+00

eq. 0: Rate effects off (default)

eq. 1: Rate effects on

Erode Erosion.....= 1.0000E+00

lt. 1: Erosion off

gt. 1: Erosion on

Erode elements when the maximum principal

strain exceeds value minus one

Recover Recover modulus in compression.....= 0.0000E+00

Iretract Cap retraction option.....= 0.0000E+00

eq. 0: Cap does not retract (default)

eq. 1: Cap retracts

Predam Initial damage in concrete.....= 0.0000E+00

Stiffness:

Shear Shear Modulus.....= 1.3590E+01

Bulk Bulk Modulus.....= 1.4880E+01

TXC Surface:

alpha TXC surface constant term.....= 1.6020E-02

theta TXC surface linear term.....= 3.6480E-01

lambda TXC surface nonlinear term.....= 1.0510E-02

beta TXC surface exponent.....= 1.9290E+01

TOR Surface Scaling Factors:

alpha TOR surface constant term.....= 7.4730E-01

theta TOR surface linear term.....= 4.7500E-01

lambda TOR surface nonlinear term.....= 1.7000E-01

beta TOR surface exponent.....= 4.3140E+01

TXE Surface Scaling Factors:

alpha TXE surface constant term.....= 6.6000E-01

theta TXE surface linear term.....= 5.7040E-01

lambda TXE surface nonlinear term.....= 1.6000E-01

beta TXE surface exponent.....= 4.3140E+01

Shear Surface Hardening Parameters:

NH Hardening initiation.....= 1.0000E+00

CH Hardening rate.....= 0.0000E+00

Cap and Cap Hardening Parameters:

R Cap surface aspect ratio..... .= 5.0000E+00

Xo Cap pressure axis intercept .....= 1.0310E-01

W Hardening law maximum compaction.....= 5.0000E-02

D1 Hardening law linear exponent.....= 2.5000E-01

D2 Hardening law nonlinear exponent.....= 3.4920E-01

Damage Parameters:

B Compressive softening parameter.....= 1.0000E+02

Gfc Compressive fracture energy.....= 9.7850E-03

D Tensile/shear softening parameter.....= 1.0000E-01

Gft Tensile fracture energy.....= 9.7850E-05

Gfs Shear fracture energy.....= 9.7850E-05

pwrc Compressive damage transition power.....= 5.0000E+00

pwrt Tensile damage transition power.....= 1.0000E+00

pmod Moderate pressure fit adjustment.....= 0.0000E+00

Rate Effects Parameters:

flpar1 Compressive fluidity parameter.....= 1.0160E-03

power1 Compressive power.....= 7.8000E-01

flpar1 Tensile fluidity parameter.....= 3.1250E-03

power2 Tensile power.....= 4.8000E-01

overc Compressive overstress limit.....= 3.4550E-02

overt Tensile overstress limit.....= 3.4550E-02

sratio Ratio of shear to tensile parameter.....= 1.0000E+00

repow Power applied to fracture energies.....= 1.0000E+00

Miscellaeous Output Parameters:

si1 Pressure apex of shear surface.....= -9.3859E-03

hkmin Minimum cap location .....= 1.0000E-06

hk0 Initial cap location .....= 2.0641E-02

hkcr Critical cap location .....= 1.0000E+20

solid formulation ..... = 3

**********

Beam10

part id ..... 10

section id ..... 2

material id ..... 1

section title .....

material title .....

Shear Stud

material type ..... 24

equation-of-state type ..... 0

hourglass type ..... 4

bulk viscosity type ..... 1

density ..... = 7.80000E-06

hourglass coefficient ..... = 1.00000E-01

quadratic bulk viscosity ..... = 1.50000E+00

linear bulk viscosity ..... = 6.00000E-02

element type ..... = 1

flag for bulk viscosity in shells. = 0

flag for rbdout/matsum output ... = 0

static coefficient of friction ... = 0.00000E+00

kinetic coefficient of friction... = 0.00000E+00

exponential decay coefficient .... = 0.00000E+00

viscous friction coefficient ..... = 0.00000E+00

optional contact thickness ..... = 0.00000E+00

optional thickness scale factor... = 0.00000E+00

local penalty scale factor..... = 0.00000E+00

flag for adaptive remeshing ..... = 0

rayleigh damping coefficient..... = 0.00000E+00

e ..... = 2.00000E+02

strainrate parameter, c ..... = 0.00000E+00

strainrate parameter, p ..... = 0.00000E+00

formulation for rate effects ..... = 0.00000E+00

eq.-1.0: deviatoric strain rate

eq. 0.0: default

eq. 1.0: viscoplastic strain rate

vnu ..... = 3.00000E-01

yield ..... = 4.71000E-01

curve # for stress vs. strain .... = 0

e (harden) ..... = 0.00000E+00

plastic strain at failure, fs .... = 3.00000E-01

gt.0: active

eq.0: inactive

lt.0: user subroutine supplied for

failure and failure strain

is set to |fs|

strain ..... = 0.00E+00  0.00E+00  0.00E+00  0.00E+00

0.00E+00  0.00E+00  0.00E+00  0.00E+00

stress ..... = 0.00E+00  0.00E+00  0.00E+00  0.00E+00

0.00E+00  0.00E+00  0.00E+00  0.00E+00

curve # for strainrate effects ... =  0

time step size for element deletion= 0.00000E+00

stochastic flag..... = 0.00000E+00

eq.0.0: standard model

eq.1.0: stochastic model

shear area factor ..... = 1.00000E+00

cross-section integration rule ... = 20.

eq.1.0:1 x 1 gauss (truss-spring)

eq.2.0:2 x 2 gauss (4 point circle)

eq.3.0:3 x 3 gauss (9 point circle)

eq.4.0:3 x 3 lobatto (9 point circle)

eq.5.0:4 x 4 gauss (16 point circle)

cross section type ..... = 1.00000E+00

eq.0.0: rectangular

eq.1.0: (tubular)

eq.2.0: arbitrary

triad location (type 6 beam) ..... = 0.00000E+00

eq.-3.: node 1 cid local axis tracts nodes

eq.-2.: node 1 local axis between nodes 1 & 2

eq.-1.: node 1

eq. 0.: midpoint

eq.+1.: node 2

eq.+2.: node 2 local axis between nodes 1 & 2

eq.+3.: node 2 cid local axis tracts nodes

nonstructural mass per unit length = 0.00000E+00

beam formulation ..... = 1

eq. 1: hughes-liu

y-fiber lengths node 1 .. = 1.90000E+01

(outer diameter) node 2 .. = 1.90000E+01

z-fiber lengths node 1 .. = 0.00000E+00

(inner diameter) node 2 .. = 0.00000E+00

y-ref. surface or sarea: node 1 .. = 0.00000E+00

eq. 1.0:top node 2 .. = 0.00000E+00

eq. 0.0:middle

eq.-1.0:bottom

z-ref. surface: node 1 .. = 0.00000E+00

eq. 1.0:top node 2 .. = 0.00000E+00

eq. 0.0:middle

eq.-1.0:bottom

c o n t a c t i n t e r f a c e s

**********

Contact Interface 1

contact type..... 13

contact interface ID ..... 1

contact order within input deck ..... 1

no. of slave segments..... 0

no. of master segments..... 0

static coefficient of friction ..... 0.40000E+00

kinetic coefficient of friction..... 0.30000E+00

exponential decay coefficient ..... 0.00000E+00

viscous friction coefficient ..... 0.00000E+00

optional load curve for tension in type 9 ... 0

optional load curve for interference-in DR .. 0

optional load curve for interference-in run . 0

small penetration in contact search ..... 0

include slave side in printed interface file 0

include master side in printed interface file 0

scale factor on default slave stiffness ..... 0.10000E+01

scale factor on default master stiffness .... 0.10000E+01

percent of critical viscous damping ..... 0.00000E+00

optional slave side thickness ..... 0.00000E+00

eq.0.0:default set actual thickness

optional master side thickness ..... 0.00000E+00

eq.0.0:default set actual thickness

scale factor on slave thickness ..... 0.10000E+01

eq.0.0:default set to 1.0

scale factor on master thickness (def.=1.0).. 0.10000E+01

eq.0.0:default set to 1.0

birth time ..... 0.00000E+00

lt.0.0:active during dynamic relaxation

and contact is always active after

dynamic relaxation is completed.

death time ..... 0.10000E+21

lt.0.0:birth time and contact are

inactive during dynamic relaxation

eq.0.0:default set to 1.0e+20

penetration treatment for auto contact ..... 1

eq.0:move penetrating nodes

eq.1:do not move penetrating nodes

constraint formulation ..... 0

scale factor for soft constraint ..... 0.10000E+00

load curve ID for airbag thickness vs. time . 0

segment extension for contact in type 26 .... 0.10250E+01

special type 13 tolerance ..... 0.20000E+01

searching depth, sd ..... 2

normal vector ID to contact surface ..... 0

normal vector ID segment angle for inclusion. 0.00000E+00

bucket sorting interval n ..... 100

contact interval force update if applicable.. 1

Contact segment search option..... 0

max penetration distance for old type 3, 5 & 10

contacts or segment thickness multiplied by

PENMAX defines max penetration distance for

contact types a 3, a 5, a10, and 13..... 0.00000E+00

thickness offsets for contact #s 3, 5, & 10 . 2

thickness considered in type 3 contact ..... 0

opening/closing flag (implicit only) ..... 0

shooting node logic ..... 0

optional thickness for solid elements ..... 0.00000E+00

optional stiffness for solid elements ..... 0.00000E+00

feature angle tolerance for smooth contact... 0.00000E+00

optional coordinate ID for RCFORC output..... 0

nonlinear scale factor for contact forces.... 0.00000E+00

displacement for nonlinear scaling ..... 0.00000E+00

incremental calculation flag for tied contact 0

penalty fallback for constrained tied contact 0

number of materials in automatic contact.....

flag for eliminating faces on symmetry planes 0

flag for considering erosion in contact ..... 0

consideration of adjacent solids..... 0

solids not included in material subset

coulomb friction scale factor.(default=1).... 0.10000E+01

viscous friction scale factor.(default=1).... 0.10000E+01

normal stress (force) at failure..... 0.00000E+00

shear stress (force) at failure..... 0.00000E+00

exponent for normal force/option (default=2). 0.20000E+01

exponent for shear force (default=2)..... 0.20000E+01

range of coordinates for contact treatment

X-minimum..... -0.10000E+17

X-maximum..... 0.10000E+17

Y-minimum..... -0.10000E+17

Y-maximum..... 0.10000E+17

Z-minimum..... -0.10000E+17

Z-maximum..... 0.10000E+17

list of materials being considered:

all materials are treated in automatic contact

automatic contact initialization slave surface:

no. of slave segments..... 19713

no. of slave nodes..... 1943

**********

Contact summary

| Order # | Contact ID | Type | Title |
|---|---|---|---|
| 1 | 1 | 13 | |

**********

# REFERENCES


Alashker, Y.; El-Tawil, S.; Sadek, F. (2010). "Progressive collapse resistance of steel-concrete composite floors." J. Struct. Eng., 136, 1187-1196.

American Concrete Institute, (1971). *Building Code requirements for Reinforced Concrete (ACI 318-71)*, ACI Committee 318, Detroit, MI.

American Concrete Institute, (2002). *Building Code requirements for Structural Concrete (ACI 318-02),* ACI Committee 318, Farmington Hills, MI.

American Concrete Institute, (2011). *Building Code Requirements for Structural Concrete and Commentary (ACI 318-11),* ACI Committee 318, Farmington Hills, MI.

ASCE. (2006). ASCE 41-06, *Seismic Rehabilitation of Existing Buildings,* American Society of Civil Engineers, Reston, VA.

American Society for Testing and Materials (ASTM), (1994). *Standard Test Method for Flexural Strength of Concrete (using Simple Beam with Third Point Loading).* Concrete and Concrete Aggregates, 4, 04.02, ASTM Standard C 78-94.

Astaneh-Asl, A., Tan, S. (2003). *Cable Based Retrofit of Steel Building Floors to Prevent Progressive Collapse.* Final Report. Dep. Of Civil and Env. Eng., Univ. of California, Berkeley.

Bao, Y., Lew, H.S., and Kunnath, S.K. (2007). "Modeling of Reinforced Concrete Assemblies under Column-Removal Scenario." J. Struct. Eng., 2014.140.

Bazant, Z., Verdure, M. (2007). "Mechanics of Progressive Collapse: Learning from World Trade Center and Building Demolitions." J. Eng. Mech., 133 (3), 308-319.

Biggs, J.M. (1964). *Introduction to Structural Dynamics,* McGraw-Hill Book Company, New York.

British Standards Institution (BSI), (1965). "Composite construction in structural steel and concrete: Simply supported beams in building." CP 117 Part 5, London.

Centre for the Protection of Natural Infrastructure, (2011). *Review of International Research on Structural Robustness and Disproportionate Collapse,* London, UK.

Corley, G. (2004). "Lessons Learned on Improving Resistance of Buildings to Terrorist Attacks." J. Struct. Eng., 18, 68-78.

Corely, G. (2008). "Learning from disaster to prevent progressive collapse." Proceedings of ICE, 161, 41-48.

Department of Defense, (2005). Unified Facilities Criteria (UFC) 4-023-03, *Design of Buildings to Resist Progressive Collapse,* Washington, D.C.

Department of Defense, (2009). Unified Facilities Criteria (UFC) 4-023-03, *Design of Buildings to Resist Progressive Collapse,* Washington, D.C.

Elingwood, B., Marjanishvili, S., Mlakar, P. Sasani, M. Williamson, E. (2009). "Disproportionate Collapse Research Needs." Structures Congress 2009, 1896-1907.

Federal Emergency Management Agency, (1996). "The Oklahoma City Bombing: Improving building performance through multi-hazard mitigation." Building Performance Assessment Team, Rep. 277, Washington, D.C.

Federal Emergency Management Agency, (2002). "World Trade Center Building Performance Study." Building Performance Assessment Team, Rep. 403, Washington, D.C.

Federal Emergency Management Agency, (2005). "Blast-resistance Benefits of Seismic Design." Building Performance Assessment Team, Rep. 449A, Washington D.C.

Feld, J., and Carper, K. (1997). *Construction Failure.* Wiley, New York.

Foley, C.M, Martin, K., Schneeman, C. (2007). *Robustness in Structural Steel Framing Systems.* Final Report. Dep. Of Civil and Env. Eng., Marquette University.

Fuller, R. (1975). "Industrialized concrete concstruction for HUD." Industrialization in concrete building construction, American Concrete Institute, Detroit, MI.

Gannon, J., Patel, V., Waggoner, M., Williamson, E. (2009). "Discussion of Examples Using the Revised DoD Progressive Collapse Design Requirements." Structures Congress 2009, 1739-1748.

Griffiths, H., Pugsley, A.G., and Saunders, O. (1968). "Report of the inquiry into the collapse of flats at Ronan Point, Canning Town." Her Majesty's Stationery Office, London.

Hull, L. (2013). *Experimental Testing of a Steel Gravity Frame with a Composite Floor under Interior Column Loss.* M.S. Thesis, Department of Civil, Architectural and Environmental Engineering, The University of Texas at Austin.

Kim, H.S., Kim, J., An, D.W. (2008). "Development of integrated system for progressive collapse analysis of building structures considering dynamic effects." Advances in Engineering Software, 40 (2009), 1-8.

Kurland, K.S. (2004). Autocad 2004 2D Training Manual, Autodesk, Inc.

Lam, D., El-Lobody, E. (2005). "Behavior of Headed Stud Shear Connectors in Composite Beam." J. Struct. Eng., 131 (1), 96-107.

Levy, M., and Salvadori, M. (1992). *Why Buildings Fall Down*, Norton, New York.

Li, H., El-Tawil, S. (2001). "Three-Dimensional Effect in Progressive Collapse Modeling." Structures Congress 2011, 2829-2839.

Livermore Software Technology Corporation, (2001). *LS-DYNA User's Manual Version 960.* Livermore, CA.

Oklahoma City Police Department, (1995). *Alfred P. Murrah Building Bombing After Action Report,* Oklahoma City, OK.

Omika, Y., Fukuzawa, E., Koshika, N., Morikawa, H., and Fukuda, R. (2005). "Structural Responses of World Trade Center under Aircraft Attacks." J. Struct. Eng., 131, 6-15.

Orton, S., Kirby, J. (2012). "Dynamic Response of a RC Frame under Column Removal." J. Perform. Constr. Facili.

Patil, P.S., Shaikh, M.G. (2013). "A Study of Effect of Shear Connector in Composite Beam in Combined Bending and Shear by Ansys." International Journal of Innovative Technology and Exploring Engineering, Volume-3, Issue-3, 67-74.

Pearson, C., Delatte, N. (2003). "Lessons from the Progressive Collapse of the Ronan Point Apartment Tower." Forensic Engineering, 190-200.

Pearson, C., Delatte, N. (2005). "Ronan Point Apartment Tower Collapse and its Effect on Building Codes." J. Perform. Constr. Facili., 19, 172-200.

Portland Cement Association, (2005). *An Engineer's guide to: Concrete Building and Progressive Collapse Resistance.*

Prakash, A., Anandavalli, N., Madheswaran, C.K., Rajasankar, J., Lakshmanan, N. (2011). "Three Dimensional FE Model of Stud Connected Steel-Concrete Composite Girders Subjected to Monotonic Loading." International Journal of Mechanics and Applications, 1 (1), 1-11.

Qian, K., Li, B. (2012). "Experimental and Analytical Assessment on RC Interior Beam-Column Subassemblages for Progressive Collapse." J. Perform. Constr. Facili., 26 (5), 576-589.

Queiroz, F.D., Vellasco, P.C.G.S., Nethercot, D.A. (2006). "Finite element modeling of composite beams with full and partial shear connection." J. Constr. Steel. Research." 63 (2007), 505-521.

Ross, Steven (1984). *Construction Disasters: Design Failures, Causes and Prevention.* Eng. News-Rec., McGraw-Hill, New York.

Sadek, F.; El-Tawil, S.; Lew, H. (2008). "Robustness of composite floor systems with shear connectors: modeling, simulation, and evaluation." J. Struct. Eng., 134 (11), 1717-1725.

Sasani, M., Sagiroglu, S. (2009). "Progressive Collapse Resistance of Hotel San Diego." J. Struct. Eng., 134 (3), 478-488.

Sasani, M., Kazemi, A., Sagiroglu, S., Forest, S. (2011). "Progressive Collapse Resistance of an Actual 11-Story Structure Subjected to Severe Initial Damage." J. Struct. Eng., 137 (9), 893-902.

Scribner , C.F., Culver, C.G., (1998). "Investigation of the collapse of L' Ambiance Plaza." J. Perform. Constr. Facili., 2, 58-79.

Schellhammer, J., Delatte, N.J., and Bosela, P.A. (2013). "Another Look at the Collapse of Skyline Plaza at Bailey's Crossroads, Virginia." J. Perform. Constr. Facili., 27, 354-361.

Shepherd, R., and Frost, J.D. (1995). *Failures in civil engineering, structural, foundation and geoenvironmental case studies,* ASCE, New York.

Slawson, T.R. (1995). *Wall Response to Airblast Loads: The Wall Analysis Code (WAC),* U.S. Army Enginerr Waterways Experiment Station, Vicksburg, MS.

Song, B., Sezen, H. (2009). "Evaluation of an Existing Steel Frame Building against Progressive Collapse." Structures Congress 2009, 1878-1885.

Song, B., Sezen, H., Giriunas, K. (2010). "Experimental and Analytical Assessment on Progressive Collapse Potential of Two Actual Steel Frame Buildings." Structures Congress 2010, 1171-1182.

Song, B., Sezen, H., Giriunas, K. (2012). "Collapse Performance Evaluation of Steel Buildings after Loss of Columns." Structures Congress 2012, 213-224.

Stevens, D., Croweder, B., Sunshine, D., Marchand, K., Smilowitz, R., Williamson, E., and Waggoner, M. (2011). "DoD Research and Criteria for the Design of Buildings to Resist Progressive Collapse." J. Struct. Eng., 137 (9), 870-880.

Szyniszewski, S. (2009). "Dynamic Energy Based Method for Progressive Collapse Analysis." Structures Congress 2009, 1259-1268.

Tan, S., Astaneh-Asl, A. (2003). "Use of Steel Cables to Prevent Progressive Collapse of Existing Buildings." Proceedings of Sixth Conference on Tall Buildings in Seismic Regions, Los Angeles, CA.

US Army Corps of Engineers, (1998). *Fundamentals of Protective Design for Conventional Weapons.* Vicksburg, MS.

US General Services Administration, (2003). *Progressive Collapse Analysis and Design Guidelines for New Federal Office Buildings and Major Modernization Projects,* Washington, D.C.

Vlassis, A.G., Izzuddin, B.A., Elghazouli, A.Y., Nethercot, D.A. (2008). "Progressive collapse of multi-storey building due to failed floor impact." Engineering Structures, 31 (2009), 1522-1534.

Yi, W.I., Kunnath, S.K., Zhang, F.Z., and Xiao, Y. (2011). "Large-Scale Experimental Evaluation of Building System Response to Sudden Column Removal." Structures Congress 2011, 2353-2357.

# VITA

Georgios Moutsanidis was born in Karditsa, Greece on March 24, 1988 to Evangelos Moutsanidis and Maria Karetsou. After graduating from 2nd Unified High School of Karditsa, he attended Aristotle University of Thessaloniki, Greece receiving a Master of Engineering in April, 2012. In August, 2012, he entered the Graduate School at The University of Texas at Austin. While completing his Master's Degree at The University of Texas, he worked as a Teaching Assistant and as a Graduate Research Assistant at the Phil M. Ferguson Structural Engineering Laboratory. He received his Master of Science in Structural Engineering degree in August 2014.

Email address: moutsanidis@utexas.edu

This thesis was typed by the author.